ornl

OAK RIDGE NATIONAL LABORATORY

UNION CARBIDE

NUREG/CR-1305
ORNL/NUREG/TM-380

Heavy-Section Steel Technology Program Quarterly Progress Report for October–December 1979

G. D. Whitman R. H. Bryan

Prepared for the U.S. Nuclear Regulatory Commission
Office of Nuclear Regulatory Research
Under Interagency Agreements DOE 40-551-75 and 40-552-75

OPERATED BY
UNION CARBIDE CORPORATION
FOR THE UNITED STATES
DEPARTMENT OF ENERGY

Printed in the United States of America. Available from
National Technical Information Service
U.S. Department of Commerce
5285 Port Royal Road, Springfield, Virginia 22161

Available from

GPO Sales Program
Division of Technical Information and Document Control
U.S. Nuclear Regulatory Commission
Washington, D.C. 20555

NUREG/CR-1305
ORNL/NUREG/TM-380
Dist. Category RF

Contract No. W-7405-eng-26

Engineering Technology Division

HEAVY-SECTION STEEL TECHNOLOGY PROGRAM QUARTERLY PROGRESS REPORT FOR OCTOBER–DECEMBER 1979

G. D. Whitman R. H. Bryan

Manuscript Completed – April 14, 1980
Date Published – May 1980

Prepared for the
U.S. Nuclear Regulatory Commission
Office of Nuclear Regulatory Research
Under Interagency Agreements DOE 40-551-75 and 40-552-75

NRC FIN No. B0119

Prepared by the
OAK RIDGE NATIONAL LABORATORY
Oak Ridge, Tennessee 37830
operated by
UNION CARBIDE CORPORATION
for the
DEPARTMENT OF ENERGY

CONTENTS

PREFACE

The Heavy-Section Steel Technology (HSST) Program, which is sponsored by the Nuclear Regulatory Commission, is an engineering research activity devoted to extending and developing the technology for assessing the margin of safety against fracture of the thick-walled steel pressure vessels used in light-water-cooled nuclear power reactors. The program is being carried out in close cooperation with the nuclear power industry. This report covers HSST work performed in October through December 1979, except for subcontractor contributions which may cover the three-month period ending in November. The work performed by Oak Ridge National Laboratory (ORNL) and by subcontractors is managed by the Engineering Technology Division. Major tasks at ORNL are carried out by the Engineering Technology Division and the Metals and Ceramics Division. Prior progress reports on this program are ORNL-4176, ORNL-4315, ORNL-4377, ORNL-4463, ORNL-4512, ORNL-4590, ORNL-4653, ORNL-4681, ORNL-4764, ORNL-4816, ORNL-4855, ORNL-4918, ORNL-4971, ORNL/TM-4655 (Vol. II), ORNL/TM-4729 (Vol. II), ORNL/TM-4805 (Vol. II), ORNL/TM-4914 (Vol. II), ORNL/TM-5021 (Vol. II), ORNL/TM-5170, ORNL/NUREG/TM-3, ORNL/NUREG/TM-28, ORNL/NUREG/TM-49, ORNL/NUREG/TM-64, ORNL/NUREG/TM-94, ORNL/NUREG/TM-120, ORNL/NUREG/TM-147, ORNL/NUREG/TM-166, ORNL/NUREG/TM-194, ORNL/NUREG/TM-209, ORNL/NUREG/TM-239, NUREG/CR-0476 (ORNL/NUREG/TM-275), NUREG/CR-0656 (ORNL/NUREG/TM-298), NUREG/CR-0818 (ORNL/NUREG/TM-324), NUREG/CR-0980 (ORNL/NUREG/TM-347), and NUREG/CR-1197 (ORNL/NUREG/TM-370).

SUMMARY*

1. PROGRAM ADMINISTRATION AND PROCUREMENT

The Heavy-Section Steel Technology (HSST) Program is an engineering research activity conducted by the Oak Ridge National Laboratory (ORNL) for the Nuclear Regulatory Commission (NRC) in coordination with other research sponsored by the federal government and private organizations. The program comprises studies relating to all areas of the technology of the materials fabricated into thick-section primary-coolant containment systems of light-water-cooled nuclear power reactors. The principal area of investigation is the behavior and structural integrity of steel pressure vessels containing cracklike flaws. Current work is organized into the following tasks: (1) program administration and procurement, (2) fracture mechanics analyses and investigations, (3) investigations of irradiated materials, (4) thermal shock investigations, and (5) pressure vessel investigations.

The work performed under the existing research and development subcontracts is included in this report.

Fourteen program briefings, reviews, or presentations were made during the quarter.

2. FRACTURE MECHANICS ANALYSES AND INVESTIGATIONS

Creager's elastic equations for stresses near notch tips were used to derive the relation $K_I^2 = E'J$ for a notch with a finite root radius. This result and the path independence of J were then applied to a bielastic specimen to derive the incremental form of Neuber's equation, $K_\sigma K_\varepsilon = K_t^2$, which had been used as the starting point for developing the tangent modulus method of elastic-plastic fracture analysis. In addition, by using Ilyushin's principle of stress and strain scaling for power-law stress-

*Conversions from SI to English units for all SI quantities are listed on a foldout page at the end of this report.

strain curves, the more familiar deformation theory form of Neuber's equation was obtained, thus clarifying the applicability of this often-used equation.

In developing a standard method for crack-arrest toughness testing, results of the Cooperative Test Program are being organized and analyzed. Compliance calibrations established following those tests indicate that small adjustments need to be made in the compliance expressions used for data analysis. Improvements are being made in the technique for initiating cleavage under desired conditions. Tests were made to aid in establishing an appropriate specimen size criterion. The three steels to be used in the series known as the Round-Robin Program have been located.

The NOZ-FLAW computer program developed at Georgia Institute of Technology for nozzle-corner crack analysis is being converted to an IBM version being made operational at ORNL. The automatic mesh generator segment is operational.

A combined pressure-thermal loading stress analysis of a boiling-water reactor feedwater nozzle has been made with ADINA and ADINAT codes to provide input to the BIGIF program, which calculates K_I distributions for nozzle-corner flaws.

The continuing photoelastic studies of crack propagation and arrest are concerned presently with two-dimensional finite-element computations of crack behavior in specimens and vessels, experiments on late-breaking ligaments, investigation of the cleavage-fibrous fracture transition, and study of effects of higher-order terms in photoelastic data reduction. The finite-element code is being modified to accept vessel geometry and loading. Experiments on damping in compact specimens indicate that both crack size and crack depth affect damping.

3. INVESTIGATIONS OF IRRADIATED MATERIALS

The first capsule of fracture mechanics specimens in the fourth irradiation series is being irradiated. A thermal shield was designed and installed to reduce gamma heating of the specimens to a level at which uniformity of temperature could be ensured.

4. THERMAL SHOCK INVESTIGATIONS

Posttest calibration of crack-opening displacement gages used in thermal shock experiment TSE-5 was made, and the value of the maximum crack velocity was revised. An analysis of secondary cracking in TSE-5 shows that the effect of secondary cracking on the primary crack was small.

Calculations were made for evaluating the conditions of the next thermal shock experiment. Variations in material toughness and the severity of the thermal shock were considered. Analyses indicate that test conditions leading to a conclusive warm-prestressing demonstration may be difficult to attain.

5. PRESSURE VESSEL INVESTIGATIONS

Specifications were prepared and bids were invited for (1) repairing intermediate test vessel V-8, (2) developing a low-toughness-weld process, and (3) inserting a low-toughness seam weld in the vessel.

We studied the possibility of testing vessel V-7 in the HSST vessel test facility for observation of acoustic emissions from a flawed vessel under cyclic loads. Pacific Northwest Laboratories proposed to make such observations in their NRC-sponsored program. Most of the objectives could be met in the available facility with cyclic notch pressurization.

HEAVY-SECTION STEEL TECHNOLOGY PROGRAM QUARTERLY PROGRESS REPORT FOR OCTOBER–DECEMBER 1979

G. D. Whitman R. H. Bryan

ABSTRACT

The Heavy-Section Steel Technology Program is an engineering research activity conducted by the Oak Ridge National Laboratory for the Nuclear Regulatory Commission. The program comprises studies related to all areas of the technology of materials fabricated into thick-section primary-coolant containment systems of light-water-cooled nuclear power reactors. The investigation focuses on the behavior and structural integrity of steel pressure vessels containing cracklike flaws. Current work is organized into five tasks: (1) program administration and procurement, (2) fracture mechanics analyses and investigations, (3) investigations of irradiated materials, (4) thermal shock investigations, and (5) pressure vessel investigations.

An elastic-plastic fracture analysis based on power-law strain hardening was developed. Preparations are being made for a round-robin crack-arrest test program. Nozzle-corner cracks under combined pressure and thermal loadings are being analyzed by both finite-element and boundary-integral methods. Photoelastic and theoretical studies of crack propagation and arrest are continuing. Irradiation of fracture specimens in a new series was initiated. Posttest analyses of the last thermal shock experiment and preliminary studies for the next experiment were made. Specifications were developed for preparing a vessel for a low-upper-shelf intermediate vessel test.

---

1. PROGRAM ADMINISTRATION AND PROCUREMENT

G. D. Whitman

The Heavy-Section Steel Technology (HSST) Program, a major safety program sponsored by the Nuclear Regulatory Commission (NRC), is concerned with the structural integrity of the primary systems (particularly the reactor pressure vessels) of light-water-cooled nuclear power reactors. The structural integrity of these vessels is ensured by (1) designing and fabricating them according to the standards set by the code for nuclear pressure vessels, (2) detecting flaws of significant size that occur during fabrication and in service, and (3) developing methods of producing quantitative estimates of conditions under which fracture could

occur. The program is concerned mainly with developing pertinent fracture technology, including knowledge of the material used in these thick-walled vessels, the flaw growth rate, and the combination of flaw size and load that would cause fracture and thus limit the life and/or operating conditions for this type of reactor plant.

The program is coordinated with other government agencies and with the manufacturing and utility sectors of the nuclear power industry in the United States and abroad. The overall objective is quantification of safety assessments for regulatory agencies, professional code-writing bodies, and the nuclear power industry. Several activities are conducted under subcontracts by research facilities in the United States and through informal cooperative efforts on an international basis. Three research and development subcontracts are currently in force. Two subcontracts for which results have been reported herein for several years have terminated: with Westinghouse Electric Corporation on fatigue-crack growth in pressurized-water reactor (PWR) primary-coolant environment and with Hanford Engineering Development Laboratory on testing of irradiated specimens. Work along these lines is being continued under the NRC's contract with the Naval Research Laboratory.

Administratively, the program is organized into five tasks, as reflected in this report: (1) program administration and procurement, (2) fracture mechanics analyses and investigations, (3) investigations of irradiated material, (4) thermal shock investigations, and (5) pressure vessel investigations.

During this quarter, 14 program briefings, reviews, or presentations were made by the HSST staff at technical meetings and at program reviews for the NRC staff or visitors. One technical report was published.[1]

Reference

1. R. H. Bryan et al., *Test of 6-in.-Thick Pressure Vessels. Series 3: Intermediate Test Vessel V-8*, ORNL/NUREG-58 (December 1979).

2. FRACTURE MECHANICS ANALYSES AND INVESTIGATIONS*

2.1 An Application of the J-Integral to the Elastic-Plastic Analysis of Blunting Cracks†

J. G. Merkle

2.1.1 Introduction

The development of linear-elastic fracture mechanics (LEFM) has made it possible to measure fracture toughness and to estimate safety margins against fracture for structures constructed of high-yield-strength, low-toughness materials. However, the majority of structures are designed and built of materials that are selected with the objective of preventing fracture at stresses below the yield stress. Thus, estimating fracture loads and safety margins for most structures, based on actual measured or probable undetected flaw sizes, requires some form of elastic-plastic fracture mechanics.

Several methods of elastic-plastic fracture analysis have been proposed in recent years. The methods potentially easiest to apply to structures are semiempirical methods based on some particular simplified yet still general description of cracked structural behavior. The only theoretically based method of elastic-plastic fracture analysis currently receiving wide attention is the J-integral.[1,2] This method has been used to calculate fracture toughness values for small two-dimensional test specimens but not yet to calculate fracture strengths for large structures containing small three-dimensional flaws. What is currently needed for structural safety assessments is either a workable simplification of the J-integral approach or a better theoretical justification for one of the semiempirical approaches.

---

*Conversions from SI to English units for all SI quantities are listed on a foldout page at the end of this report.

†Symbols used in this section are defined in Sect. 2.1.11.

2.1.2 Theoretical considerations

The J-integral[1,2] is the most widely accepted basis for elastic-plastic fracture analysis because its definition is physically based and mathematically exact; and, by virtue of path independence, its value can be determined analytically or experimentally by several different methods. However, its definition is based on the deformation theory of plasticity, which is known to be physically less accurate than incremental theory.[3] The incremental theory of plasticity is accepted as a more accurate method of elastic-plastic stress analysis because it recognizes that the principal stress ratios at a point can change during loading.[3] Nevertheless, almost all the currently proposed methods for elastic-plastic fracture analysis are based, explicitly or implicitly, on deformation theory, because they calculate the crack-driving force directly as a function of the currently applied load.

Efforts have already been made to evaluate or to justify several of the proposed methods for elastic-plastic fracture analysis. The J-integral is often justified as a fracture criterion because it serves as the loading parameter for the deformation theory stress distribution near the tip of an infinitely sharp crack in a material with a pure power-law stress-strain curve.[4] For this type of stress-strain curve and proportional applied loading only, deformation theory and incremental theory agree exactly, and stress analysis solutions are scalable according to Ilyushin's principle.[5,6] Hutchinson, Goldman, Shih, and Kumar[7,8] have taken advantage of this fact to develop a J-integral estimating procedure based on scaling. However, as stated earlier, deformation theory is known to be of limited accuracy; cracks do not remain infinitely sharp during loading, especially in the elastic-plastic range; and most materials do not deform exactly according to a pure power-law stress-strain curve. Furthermore, the estimating procedure of Shih and Kumar[8] still requires nonlinear numerical analysis and has not yet been extended to three-dimensional problems.

Another approach to the treatment of the elastic-plastic aspects of crack-tip behavior was developed by Neuber[9] in the form of the equation[10]

$$K_\sigma K_\varepsilon = K_t^2 , \qquad (1)$$

where K_σ and K_ε are the ratios of the peak to the nominal stresses and strains, respectively, and K_t is the theoretical elastic stress concentration factor. Neuber's equation [Eq. (1)] is by far the simplest equation available for the elastic-plastic stress analysis of notches. However, its application to cracks is hampered by the need to specify a value of the crack-tip root radius and by the lack of an analytical relationship connecting it to the more widely accepted equations of fracture mechanics.

Neuber's equation was originally developed for deformation theory conditions. However, it has since been applied successfully in an incremental form, for both cyclic fatigue analysis[11,12] and monotonic loading elastic-plastic fracture analysis,[13-16] although without a completely theoretical basis. In the incremental form of Eq. (1), the total stress and strain terms on the left side of the equation are simply replaced by the corresponding increments. The primary potential advantage of Neuber's equation is that the effects of geometry can be determined from a linear-elastic analysis and do not have to be redetermined in the plastic range, thus avoiding the need for a difficult and expensive nonlinear numerical analysis. Neuber concluded that Eq. (1) was independent of the shape of the stress-strain curve. However, noting Neuber's[9] result that the solution for a Mode III–loaded crack also provides a solution for a notch with a finite root radius, Rice[17] pointed out that the elastic–perfectly plastic solution described by McClintock and Irwin[18] agrees with Eq. (1) only for the case of small-scale yielding. Therefore, Eq. (1) apparently cannot be completely general. Nevertheless, if a form of Neuber's equation can be found that is independent of the stress-strain curve, then it may still provide a valid basis for a practical method of elastic-plastic fracture analysis that does not involve unrealistic or unnecessary assumptions about the elastic-plastic behavior of cracked structures. In addition, the principles of the theory of plasticity probably will have to be applied explicitly to clarify further the applicability and limitations of Neuber's equation.

2.1.3 Analytical starting points

Reference 14 shows that an expression for the product of the notch root strain increment multiplied by the square root of the notch root

radius can be derived from Neuber's equation written in incremental form and that the expression contains the factor $\sqrt{E_g/E_n}$, where E_g and E_n are the tangent moduli in the gross section and at the notch root, respectively. This expression was used in refs. 15 and 16 as the basis for accurate posttest calculations for several sets of elastic-plastic fracture specimen test data. Nevertheless, the lack of a completely theoretical basis for the method of analysis remained the basis for uncertainty concerning its applicability and limitations.[19,20] Therefore, efforts were undertaken to improve the analytical basis of the method.

In searching for an improved analytical basis for the incremental form of Neuber's equation, we noted that Hutchinson[21] had obtained a solution for the stresses near the tip of a sharp crack in elastic-linear strain-hardening material and that the result was the classical elastic solution, multiplied by the factor $\sqrt{E_T/E}$, where E_T and E are the crack region and the remote region tangent moduli, respectively. Furthermore, Wang[22] has recently obtained the same result for the case of a bielastic adhesive joint specimen. These results suggested that an analytical basis for the incremental form of Neuber's equation might be obtainable by using a bielastic specimen as an analytical starting point. Such an analytical model is shown in Fig. 2.1, which depicts a blunted crack in an elastic body whose near-tip region has an elastic modulus of E_T and the remainder, an elastic modulus of E. Because of path independence, the value of J should be the same for all contours surrounding the notch tip that begin and end on parallel segments of the notch faces. Thus,

$$J_T = J_\infty \ , \tag{2}$$

where J_T is the value of J computed for a contour lying close to the notch tip entirely within the region of modulus E_T and J_∞ is the value of J computed for a contour located remote from the notch tip entirely within the region of modulus E.

Since the purpose of the analysis to be developed is to examine the basis of Eq. (1), consideration of the existence of a finite notch root radius is necessary to prevent the value of K_t from becoming infinite.

ORNL-DWG 80-4339 ETD

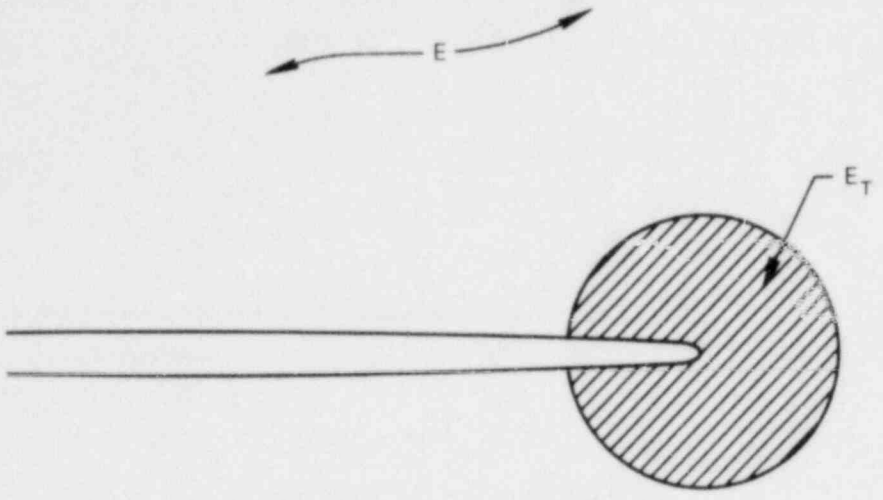

Fig. 2.1. Schematic drawing of a blunted crack in a bielastic specimen with notch-tip region elastic modulus E_T and elastic modulus E elsewhere.

Rice's derivation of the J-integral[1] recognized the possible existence of a finite notch root radius, as demonstrated by the equation

$$J = \int_{\Gamma_t} W \, dy \ , \tag{3}$$

where W is strain energy density, y is distance perpendicular to the notch centerline, and Γ_t is the notch-tip contour. Consequently, the existence of a finite notch root radius should not affect the path independence of J. Furthermore, since J is derived for nonlinear elastic conditions, its path independence should not be affected by a difference in the elastic modulus values between the notch-tip region and other remote regions, as assumed in writing Eq. (2).

To relate J to the notch-tip stress field, a relation between these quantities must be used that is valid for notches having finite root radii as well as for infinitely sharp cracks. The relation

$$J = K_I^2/E' \ , \tag{4}$$

where $E' = E/(1 - \nu^2)$ for plane strain and E for plane stress, was derived by Irwin[23] for sharp cracks. However, implicitly, the same relation was derived by Rice[2] for notches with finite root radii. The latter derivation consisted of developing the equation for J by integrating along a contour surrounding the notch tip having a radius that was large compared with the notch root radius but small compared with other specimen dimensions, so that the only terms entering the expression for J were the singular inverse square root sharp crack terms. In Rice's derivation, the radius of the contour of integration was taken to be effectively infinite; thus, the problem actually analyzed was a semiinfinite notch in an infinite body. Because any terms involving the notch root radius were eliminated at the input stage of Rice's analysis by the choice of an integration path, their null effect was only implicit in the results. However, explicit consideration of the effects of a notch root radius on the relation between J and K_I should be made possible by applying Eq. (3) to Creager's elastic notch-region stress equations.[24,25] For each stress component, Creager's equations consist of the sharp-crack-stress term plus an additional term proportional to the product of K_I and the notch root radius.

For a narrow elliptic or hyperbolic notch, the near-tip region of which is shown in Fig. 2.2, the near-tip normal stresses are given by[24,25]

$$\sigma_x = \frac{K_I}{\sqrt{2\pi r}} \cos\frac{\theta}{2}\left(1 - \sin\frac{\theta}{2}\sin\frac{3\theta}{2}\right) - \frac{K_I}{\sqrt{2\pi r}}\left(\frac{\rho}{2r}\right)\cos\frac{3\theta}{2}, \qquad (5)$$

and

$$\sigma_y = \frac{K_I}{\sqrt{2\pi r}} \cos\frac{\theta}{2}\left(1 + \sin\frac{\theta}{2}\sin\frac{3\theta}{2}\right) + \frac{K_I}{\sqrt{2\pi r}}\left(\frac{\rho}{2r}\right)\cos\frac{3\theta}{2}, \qquad (6)$$

where the coordinate axes x and y are parallel and perpendicular, respectively, to the centerline of the notch. In Eqs. (5) and (6), the origin of the cylindrical coordinates is the focal point of the notch profile, which is located on the x axis at a distance $\rho/2$ behind the notch tip. In addition, the stress-intensity factor K_I has exactly the

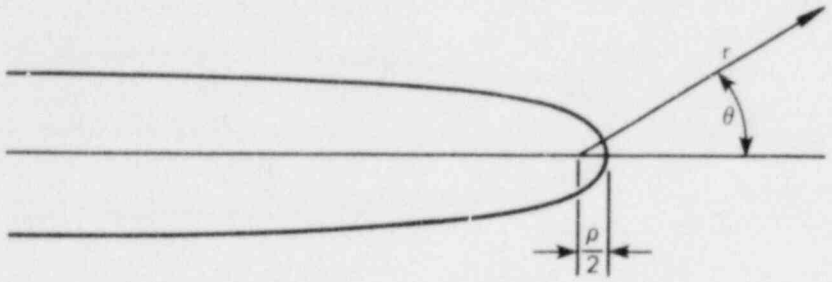

Fig. 2.2. Profile of the near-tip region of a narrow elliptic or hyperbolic notch showing coordinate system used with Creager's elastic stress equations (ref. 24).

same definition in terms of nominal stress and notch depth as it would have for a sharp crack of the same depth.

For either plane stress or plane strain, the only stress that contributes to the strain energy density on a traction-free notch surface is σ_t, the principal stress acting tangential to the notch surface. Mohr's circle can be used to show that, on the notch surface,

$$\sigma_t = \sigma_x + \sigma_y \, . \tag{7}$$

Thus, substituting Eqs. (5) and (6) into Eq. (7) gives

$$\sigma_t = \frac{2K_I}{\sqrt{2\pi r}} \cos\frac{\theta}{2} \, , \tag{8}$$

in which terms proportional to ρ do not appear because of their opposite signs in Eqs. (5) and (6).

2.1.4 Representation of notch geometry

To apply Eq. (3) to determining the relation between J and K_I by integrating along the notch contour, an expression for the notch contour that allows the determination of J by closed-form integration is desirable. Considering a narrow elliptical notch, the tip region of which is

shown in Fig. 2.3, the equation of the notch profile is given by

$$(x^2/a^2) + (y^2/b^2) = 1 \ , \tag{9}$$

and the notch-tip radius of curvature is given by

$$\rho = b^2/a \ . \tag{10}$$

Substituting Eq. (10) into Eq. (9) and rearranging gives

$$x^2 + (a/\rho)y^2 = a^2 \ . \tag{11}$$

From Fig. 2.3,

$$x = a + \left(r \cos \theta - \frac{\rho}{2}\right) , \tag{12}$$

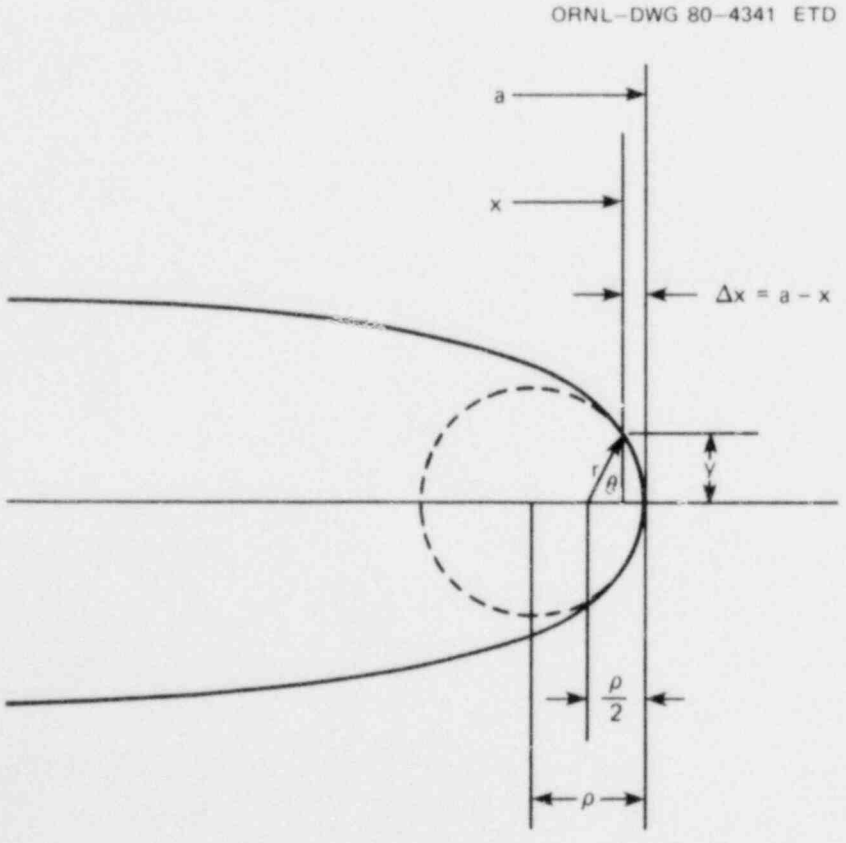

Fig. 2.3. Near-tip region of an elliptical notch showing coordinates and dimensions used in the parabolic approximation of the notch profile.

and

$$y = r \sin \theta \ . \tag{13}$$

Squaring Eq. (12) gives

$$x^2 = a^2 + 2a\left(r \cos \theta - \frac{\rho}{2}\right) + \left(r \cos \theta - \frac{\rho}{2}\right)^2 \ ; \tag{14}$$

for r and ρ both small compared with a,

$$x^2 \sim a^2 + 2a\left(r \cos \theta - \frac{\rho}{2}\right) . \tag{15}$$

Substituting Eq. (15) into Eq. (11) gives

$$2a\left(r \cos \theta - \frac{\rho}{2}\right) + \left(\frac{a}{2}\right)y^2 = 0 \ . \tag{16}$$

From Fig. 2.3,

$$\left(r \cos \theta - \frac{\rho}{2}\right) = -\Delta x \ , \tag{17}$$

so that combining Eqs. (16) and (17) gives

$$y = \sqrt{2\rho\Delta x} \ , \tag{18}$$

which is the equation of a parabola. Equation (18) demonstrates that the effect of Eq. (15) is to represent a narrow ellipse with the parabola having the same end-point radius of curvature.

Substituting Eq. (13) into Eq. (16) and solving the resulting quadratic equation for r gives

$$r = \frac{\rho}{1 + \cos \theta} \ . \tag{19}$$

Equation (19) holds as long as $r \ll a$.

2.1.5 Relation between J and K_I for a blunted notch

The elastic strain energy density on the surface of a blunt notch is given by

$$W = \frac{\sigma_t^2}{2E'} \ . \tag{20}$$

Combining Eqs. (8) and (20) thus gives

$$W = \frac{K_I^2}{E'} \frac{\cos^2 \frac{\theta}{2}}{\pi r} . \tag{21}$$

Substituting Eq. (19) and the identity

$$\cos^2 \frac{\theta}{2} = \frac{1 + \cos \theta}{2} \tag{22}$$

into Eq. (21) thus leads to

$$W = \frac{K_I^2}{E'} \left[\frac{(1 + \cos \theta)^2}{2\pi\rho} \right] . \tag{23}$$

Combining Eqs. (13) and (19) gives

$$y = \frac{\rho \sin \theta}{(1 + \cos \theta)} , \tag{24}$$

so that

$$dy = \frac{\rho \, d\theta}{(1 + \cos \theta)} . \tag{25}$$

Thus, substituting Eqs. (23) and (25) into Eq. (3) gives

$$J = \frac{K_I^2}{E'} \left(\frac{1}{2\pi} \right) \int_{-\pi}^{\pi} (1 + \cos \theta) \, d\theta . \tag{26}$$

By direct integration, Eq. (26) gives

$$J = \frac{K_I^2}{E'} . \tag{27}$$

Thus, the relation between J and K_I is unaffected by the existence of a root radius.

The problem analyzed to derive Eq. (27) is the crack surface counterpart of the problem analyzed by Rice.[2] It uses the near-notch-tip stress equations (as did Rice) and locates the end points of the notch profile

at an effectively infinite distance from the notch tip (as did Rice) to ensure reaching a condition of parallel notch faces at the end points of the integration. The equations used are valid as long as the distance from the notch tip is small compared with the notch depth.

2.1.6 Stress concentration in a bielastic specimen

Returning to the blunted crack in the bielastic specimen shown in Fig. 2.1, applying Eq. (27) to both sides of Eq. (2) gives

$$J = K_T^2/E_T' = K_\infty^2/E' \ , \tag{28}$$

where K_T is the stress-intensity factor of the actual near-tip stress field and K_∞ is the stress-intensity factor calculated on the basis of the remote nominal stress and crack size. The null effect of a small zone of reduced modulus near the notch tip on the value of K_∞ was pointed out by Rice.[2] Since there is no dependence of the near-tip stress variation on the numerical value of the elastic modulus, it follows that each of the actual near-tip stress components is given by

$$\sigma = \frac{K_T}{\sqrt{2\pi r}} f\left(\frac{\rho}{r}, \theta\right) \tag{29}$$

and that the near-tip stress that would exist in a homogeneous elastic specimen are given by

$$\sigma_e = \frac{K_\infty}{\sqrt{2\pi r}} f\left(\frac{\rho}{r}, \theta\right) \ . \tag{30}$$

Rearranging Eq. (28) and assuming no variation in Poisson's ratio within the specimen gives

$$K_T = K_\infty \sqrt{E_T/E} \ , \tag{31}$$

which is identical to the result obtained by Wang[22] for a sharp crack in an elastic adhesive joint specimen. Then, by substituting the expressions

for K_T and K_∞ obtained from Eqs. (29) and (30) into Eq. (31), it follows that

$$\sigma = \sigma_e\sqrt{E_T/E} \ ; \tag{32}$$

that is, the near-tip stresses are the same as the stresses calculated for a homogeneous elastic specimen but then multiplied by the factor $\sqrt{E_T/E}$. This is exactly the same as the result obtained by Hutchinson[21] for a sharp crack in a material described as an elastic-linear strain-hardening material.

2.1.7 Incremental elastic-plastic analysis of notch-tip stresses and strains

Since Eq. (32) is valid for a notch with a finite root radius, it provides a basis for examining the incremental changes in stress and strain at the root of a notch. At the root of a notch,

$$\sigma_e = K_t S \ , \tag{33}$$

where K_t is the theoretical elastic stress concentration factor and S is the nominal stress. Combining Eqs. (32) and (33) gives

$$\sigma = K_t S\sqrt{E_T/E} \ . \tag{34}$$

Equation (34) still applies only for elastic conditions, but it can be used to develop an elastic-plastic analysis if one recognizes that the incremental response of an elastic-plastic body to a load increment is still linear — that is, although the tangent moduli at points throughout a body loaded into the plastic range may change from one load increment to the next, they do not change during a given load increment. Thus, for considering elastic-plastic behavior, Eq. (34) can be differentiated, holding E_T and E constant as the tangent moduli governing the notch tip and the nominal strain increments, respectively. Therefore, for elastic-plastic conditions,

$$d\sigma = K_t \ dS\sqrt{E_T/E} \ . \tag{35}$$

Squaring both sides of Eq. (35) and rearranging gives

$$d\sigma(d\sigma/E_T) = dS(dS/E)(K_t^2) \ . \tag{36}$$

Since

$$E_T = \frac{d\sigma}{d\varepsilon} \tag{37}$$

and

$$E = \frac{dS}{d\lambda} \ , \tag{38}$$

where ε and λ are the peak and the nominal strains, respectively, substituting Eqs. (37) and (38) into Eq. (36) and rearranging gives

$$(d\sigma/dS)(d\varepsilon/d\lambda) = K_t^2 \ , \tag{39}$$

which is the incremental form of Neuber's equation [Eq. (1)] proposed and used in refs. 13 through 16. It is important to note that the derivation of Eq. (39) involves no assumption about the shape of the stress-strain curve. However, Eq. (39) is particularly easy to apply when the stress-strain curve is represented as a piecewise linear curve.

2.1.8 Total stress and strain analysis for a power-law stress-strain curve

As mentioned previously, Ilyushin's principle[5,6] states that elastic-plastic solutions for proportional boundary loading are scalable for power-law stress-strain curves. This implies that for a pure power-law stress-strain curve, the incremental ratios in Eq. (39) can be replaced by the corresponding ratios of total stress and strain, thus producing the deformation theory form of Neuber's equation [Eq. (1)]. Because unabbreviated explanations of Ilyushin's principle in current textbooks and literature are scarce, its basis will be reviewed here before assuming its applicability to Eq. (39). A reverse proof of Ilyushin's principle was developed recently by Chang and Witt,[26] who showed that if scaling is assumed to hold, then the stress-strain relation must be a power law.

Consider an elastic-plastic body under load with internal stress and strain distributions that satisfy the pure power-law stress-strain relation

$$\bar{\varepsilon} = A\bar{\sigma}^N \tag{40}$$

and the deformation theory flow rule

$$\varepsilon_{ij} = \bar{\varepsilon}(\partial\bar{\sigma}/\partial\sigma_{ij}) , \tag{41}$$

where $\bar{\sigma}$ and $\bar{\varepsilon}$ are the effective stress and effective strain, respectively. Now consider the internal stresses at each point to increase in proportion until they all reach values of q times their original values, and assume that the strain increments occurring at each point during this process are those corresponding to the incremental theory flow rule

$$d\varepsilon_{ij} = d\bar{\varepsilon}(\partial\bar{\sigma}/\partial\sigma_{ij}) . \tag{42}$$

Because the equations of equilibrium are linear partial differential equations, a constant multiplied by a solution is a solution, and the scaled stresses will equilibrate a set of loads q times the original loads. Also, since the stress ratios remain constant, the effective stresses at all points will increase in proportion to the stress components so that

$$\frac{d\bar{\sigma}}{\bar{\sigma}} = \frac{d\sigma_{ij}}{\sigma_{ij}} . \tag{43}$$

By differentiating Eq. (40),

$$\frac{d\bar{\varepsilon}}{\bar{\varepsilon}} = N\,\frac{d\bar{\sigma}}{\bar{\sigma}} \tag{44}$$

so that the effective strains will increase by the same fraction everywhere. Because of the normality rule of plasticity, the partial

derivatives in Eqs. (41) and (42) are equal, so that dividing Eq. (42) by Eq. (41) gives

$$\frac{d\varepsilon_{ij}}{\varepsilon_{ij}} = \frac{d\bar{\varepsilon}}{\bar{\varepsilon}} \ . \tag{45}$$

Consequently, all the individual strain components at each point will also increase together by the same fraction. Because the equations of compatibility are linear, the scaled solution will also satisfy compatibility, and from Eq. (40) the final boundary displacements will be q^N times the original boundary displacements. Thus, for the problem analyzed, both the stress and the strain ratios will remain constant, and the ratio of any pair of stress or strain increments will remain equal to the ratio of the corresponding total values. Therefore, for proportional boundary loading and a power-law stress-strain curve,

$$\frac{d\sigma}{dS} = \frac{\sigma}{S} \ , \tag{46}$$

and

$$\frac{d\varepsilon}{d\lambda} = \frac{\varepsilon}{\lambda} \ ; \tag{47}$$

substituting Eqs. (46) and (47) into Eq. (39) gives

$$(\sigma/S)(\varepsilon/\lambda) = K_t^2 \ . \tag{48}$$

Since by the usual definitions of peak stress and strain,

$$\sigma/S = K_\sigma \tag{49}$$

and

$$\varepsilon/\lambda = K_\varepsilon \ , \tag{50}$$

the result of substituting Eqs. (49) and (50) into Eq. (48) is

$$K_\sigma K_\varepsilon = K_t^2 \ , \tag{51}$$

which is the original deformation theory form of Neuber's equation.[9,10]

2.1.9 Discussion

The foregoing analysis clarifies and improves the relationship between Neuber's equation for estimating the stress and strain concentration factors of notches in the elastic-plastic range and the other equations of fracture mechanics. It also helps to explain the several cases of good agreement between calculation and experimental data that have been obtained with methods of fatigue and fracture analysis based on the incremental form of Neuber's equation. One such method is the tangent modulus method of elastic-plastic fracture analysis,[15] which can be derived from Eqs. (8) and (35). Relabelling the notch region and the gross-section tangent moduli, respectively, as E_n and E_g, Eq. (35) can be written in the form

$$d\sigma = K_t \, dS\sqrt{E_n/E_g} \ . \tag{52}$$

Then, by using the definitions

$$d\sigma = E_n \, d\varepsilon \tag{53}$$

and

$$dS = E_g \, d\lambda \ , \tag{54}$$

the combination of Eqs. (52) through (54) gives

$$d\varepsilon = K_t\sqrt{E_g/E_n} \, d\lambda \ . \tag{55}$$

Using $\theta = 0$ and $r = \rho/2$ in Eq. (8) yields

$$\sigma_e = \frac{2K_I}{\sqrt{\pi\rho}} . \tag{56}$$

Then, substituting Eq. (33) and the equation

$$K_I = CS\sqrt{\pi a} \tag{57}$$

into Eq. (56) gives

$$K_t = 2C\sqrt{a/\rho} . \tag{58}$$

Finally, combining Eqs. (55) and (58) gives

$$d\varepsilon\sqrt{\rho} = 2C\sqrt{a}\sqrt{E_g/E_n}\, d\lambda , \tag{59}$$

which is the basic incremental equation of the tangent modulus method.[14,15] Note that the right side of Eq. (59) is proportional to $C\sqrt{a}$ where C is still the LEFM shape factor and a is still the crack size. The values of the tangent moduli E_n and E_g are determined by the peak and the through-the-thickness average nominal strains, respectively, using the stress-strain curve and a semiempirical adjustment for the effects of bending caused by the crack itself.[15] Similar adjustments occur elsewhere in fracture mechanics, the two most common examples being LEFM plastic zone-size corrections and the use of a flow-stress-based blunting line in resistance-curve data analysis. In the case of elastic–perfectly plastic material at the notch tip, Eq. (59) loses meaning because of division by E_n. However, for this case, reference to Eq. (52) shows that $d\sigma$ becomes zero; because $d\sigma$ and $d\varepsilon$ are uncoupled, the notch-tip strain must be determined by other means — for example, by the equation for elastic–perfectly plastic material developed by Rice.[2]

The integral of Eq. (59) can be directly related to the value of the fracture toughness as conventionally measured. This relationship is assumed to hold for any value of the nominal strain at fracture, as

is the relationship between J and K for small and large specimens. For convenience, assuming a test to fracture under nominally elastic conditions, Eq. (57) gives

$$\lambda_f = \frac{(\sigma_c/S_Y)\lambda_Y}{C\sqrt{\pi a}} . \tag{60}$$

In addition, assuming the notch-tip region to be rigid–linear strain hardening and the remainder of the specimen to be elastic, integrating Eq. (59) up to the fracture point and rearranging gives

$$\lambda_f = \frac{\varepsilon_f\sqrt{\rho}}{2C\sqrt{a}\sqrt{E/E_n}} . \tag{61}$$

Then equating the right sides of Eqs. (60) and (61) and rearranging gives the toughness conversion

$$\frac{K_c}{S_Y} = \frac{\varepsilon_f\sqrt{\rho}}{\frac{2}{\sqrt{\pi}}\sqrt{E/E_n}\lambda_Y} . \tag{62}$$

The value of $\varepsilon_f\sqrt{\rho}$ in Eq. (62) is the integral of the right side of Eq. (59). This integral is easily evaluated by direct integration and addition after first representing the nominal stress-strain curve as a piecewise linear curve, for which the ratio E_g/E_n remains constant over specified ranges of nominal strain.

Equations (59) and (62) have been used to analyze fracture test data from a series of large part-through surface-cracked tensile specimens, with the results shown in Fig. 2.4. Reference 15 contains the details of this analysis. As shown in Fig. 2.4, the analysis described here is applicable up to but not beyond the average net section stress that causes necking and plastic instability to occur in the region of the flaw. This is true because the derivation of Eq. (59) is based on small strain theory and includes only an approximate representation of the effects of stress redistribution due to yielding, by means of the variation of the tangent modulus E_g with the nominal strain. The tangent modulus method has

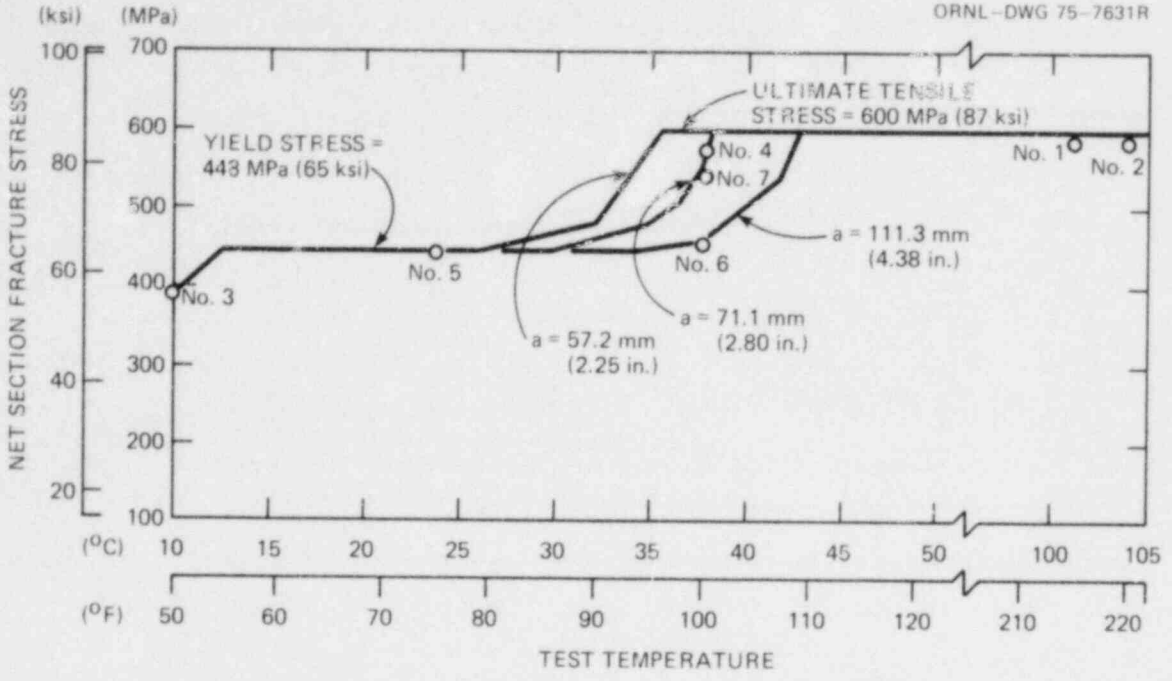

Fig. 2.4. Comparison of experimentally determined net section fracture-stress values with estimates made by the tangent modulus method for longitudinally oriented 152.4-mm-thick (6-in.) part-through surface-cracked intermediate tensile specimens of A533 grade B class 1 steel (ref. 15).

also been used to analyze fracture test data from two HSST Program intermediate test vessels with inside nozzle-corner cracks.[16] This method of analysis is particularly well suited to the estimation of fracture strengths in the elastic-plastic range at temperatures at which rapid fracture can still take place. Stable crack growth can also be considered.

The incremental form of Neuber's equation [Eq. (39)] has been used for the cyclic fatigue analysis of notches[11,12] and also to develop a relationship between fracture toughness, triaxial ductility, and other material properties.[13] The derivations presented herein help provide a theoretical basis for these methods of analysis previously considered semiempirical.

2.1.10 Conclusions

1. By using Creager's equations for the elastic stresses near the tip of a blunted notch, it is possible to show that $K_I^2 = E'J$, irrespective of the existence of a finite notch root radius.
2. Considering the path independence of J, the stresses near the tip of a notch in an elastic specimen with notch-tip region modulus E_T and remote elastic modulus E are demonstrably the same as for a homogeneous elastic specimen, except that the stresses are multiplied by the factor $\sqrt{E_T/E}$.
3. The previous result for elastic conditions can be transformed by differentiation and substitution into an incremental form of Neuber's equation for the elastic-plastic analysis of notch tips. The result, which is independent of the stress-strain curve, is the equation

$$(d\sigma/dS)(d\varepsilon/d\lambda) = K_t^2 ,$$

where σ, S, ε, and λ are the peak and the nominal stresses and strains, respectively, and K_t is the theoretical elastic stress concentration factor.

4. By using Ilyushin's principle, which states that the stress and strain solutions for proportionally loaded bodies obeying a pure power-law stress-strain curve can be scaled, the incremental form of Neuber's equation can be transformed into the familiar deformation theory form

$$K_\sigma K_\varepsilon = K_t^2 ,$$

where K_σ and K_ε are the actual stress and strain concentration factors, respectively.

5. Several methods of fatigue and fracture analysis based on the incremental form of Neuber's equation have already been developed. The analyses presented here provide an analytical basis for these methods and also an explanation of their usefulness in analyzing experimental data.

6. The method of analysis described herein is applicable up to but not beyond the loads causing necking and plastic instability of the flaw because the effects of stress redistribution due to yielding are only approximated by decreasing the tangent modulus corresponding to the nominal strain at the flaw location.

2.1.11 Nomenclature

A	Coefficient in power-law stress-strain relation having dimensions of $(\text{stress})^{-N}$
a	Notch or crack depth, m
b	Half the opening of an elliptical notch midway betwen the focal points, m
C	LEFM shape factor, dimensionless
E	Modulus of elasticity, MPa
E'	Effective modulus of elasticity for plane stress or plane strain, as specified, MPa
E_g	Gross-section tangent modulus, MPa
E_n	Notch-tip tangent modulus, MPa
E_T	Notch-tip region elastic modulus for a bielastic specimen, MPa
J	The J-integral, $MJ \cdot m^{-2}$
J_T	Value of the J-integral computed by integrating on a contour close to the notch tip, $MJ \cdot m^{-2}$
J_∞	Value of the J-integral computed by integrating on a contour remote from the notch tip, $MJ \cdot m^{-2}$
K_C	Fracture toughness, $MPa \cdot \sqrt{m}$
K_I	Linear-elastic crack-tip stress-intensity factor, $MPa \cdot \sqrt{m}$
K_T	Linear-elastic crack-tip stress-intensity factor corresponding to the stress magnitudes near a crack tip, $MPa \cdot \sqrt{m}$
K_∞	Linear-elastic stress-intensity factor calculated on the basis of the remote nominal stress, crack size, and geometry for a specimen assumed to be homogeneous, $MPa \cdot \sqrt{m}$
K_t	Theoretical elastic stress concentration factor, dimensionless
K_ε	Actual strain concentration factor, dimensionless
K_σ	Actual stress concentration factor, dimensionless

N	Strain-hardening exponent, dimensionless
r	Radial distance from notch-tip focal point, m
S	Nominal stress, MPa
S_Y	Yield stress, MPa
W	Strain energy density, MPa
x	Coordinate distance measured parallel to the notch centerline, m
Δx	Distance behind the notch tip measured along the notch centerline, m
y	Coordinate distance measured perpendicular to the notch centerline, m
Γ_t	Notch-tip contour (not an algebraic quantity)
ε	Strain near the notch tip, particularly peak strain where so stated, dimensionless
ε_f	Notch-tip fracture strain, dimensionless
$\bar{\varepsilon}$	Effective strain, dimensionless
θ	Position angle measured at the notch-tip focal point, radians
λ	Nominal strain, dimensionless
λ_f	Nominal fracture strain, dimensionless
λ_Y	Yield strain, dimensionless
ν	Poisson's ratio, dimensionless
ρ	Notch-tip radius of curvature, m
σ	Stress near the notch tip, particularly peak stress where so stated, MPa
$\bar{\sigma}$	Effective stress, MPa
σ_e	Stress in the notch region calculated for the assumption of homogeneous elastic behavior, MPa
σ_t	Principal stress acting tangential to the notch-tip contour, MPa
σ_x, σ_y	Normal stresses acting in the x and y direction, respectively, in the notch-tip region, MPa

2.2 Standard Method of Crack-Arrest Toughness Testing*†

E. J. Ripling‡ P. B. Crosley‡

2.2.1 Introduction

The task of developing a standard method for crack-arrest toughness (K_{Ia}) testing presently involves four subtasks:

1. organize, analyze, and present the results of the Cooperative Test Program on Crack-Arrest Toughness Measurements;
2. improve the method for initiating cleavage cracking;
3. establish size requirements for K_{Ia} testing;
4. arrange the American Society for Testing and Materials (ASTM) Task Group E24.01.06 Round-Robin Test Program.

2.2.2 Cooperative Test Program on Crack-Arrest Toughness Measurements

The raw data and calculated values of K_{Ia} and K_{ID} obtained on the Cooperative Program on Crack-Arrest Toughness Measurements have been distributed to the participants by Battelle Columbus Laboratories (BCL).[27] The participants calculated K by using expressions supplied by Materials Research Laboratory (MRL) and BCL for their respective specimen types. Both expressions were based on analytical compliance calibrations that were not verified experimentally. In the course of the program, both expressions were found to contain some errors: (1) the MRL analysis did not include the effect of the loading holes, so there was a compliance error for small crack lengths; (2) for the BCL specimen, displacements were measured on the split loading pins, which were found not to be identical with actual load-point displacements. Hence, both specimens were compliance-calibrated (as described in Sect. 2.2.6). The experimentally

---

*Conversions from SI to English units for all SI quantities are listed on a foldout page at the end of this report.

†Work sponsored by HSST Program under UCCND Subcontract 7755 between Union Carbide Corporation Nuclear Division and Materials Research Laboratory, Inc.

‡Materials Research Laboratory, Inc., Glenwood, Ill.

derived expression for calculating K with the MRL specimen was

$$\frac{K\sqrt{W}}{E\Delta}\left(\frac{B_N}{B}\right)^{1/2} = \frac{2.2434\ (1.7164 - 0.9x + x^2)\ \sqrt{1-x}}{(9.85 - 0.17x + 11.0x^2)}\ , \qquad (63)$$

where

K = stress-intensity factor,

W = specimen width,

E = Young's modulus,

Δ = displacement at 0.25W from the pin-hole centerline (away from the crack tip),

B_N = specimen thickness on notch plane,

B = specimen gross thickness,

x = a/w = normalized crack length.

For the BCL specimen,

$$\frac{K\sqrt{W}}{Ey}\left(\frac{B_N}{B}\right)^{1/2} = 0.9133 - 2.936x + 4.23x^2 - 2.25x^3\ , \qquad (64)$$

where y is load-line displacement measured on the split loading pins.

2.2.3 Improved method for initiating cleavage cracking

The presently recommended method of K_{Ia} testing involves the use of a machine-notched, very brittle weld for initiating the cleavage crack. To help ensure that the initiation K is not too large, the test specimen is compressed before applying the opening wedge force. Precompression is inconvenient, and elimination of it would be helpful. The very brittle weld has a more serious disadvantage in that it limits the highest temperature at which data can be collected. During mildly elevated temperature testing of A533 grade B class 1 steel, the crack tends to extend through the weld and to arrest before any appreciable extension into the base plate, presumably because the ratio of weld to test-plate toughness is too small.

To avoid precompression while using less brittle welds, some attempts have been made to initiate cracks in tougher welds by using sharper

machined notches. Not enough data have been collected on this phase of the work to determine whether this test method will be effective, however.

2.2.4 Size requirements for K_{Ia} testing

Size requirements for K_{Ia} testing are still to be established for both specimen thickness and inplane dimensions. In this program, these two-dimensional requirements are being treated separately, and the initial studies will be concerned only with thickness.

A convenient measure for defining size is the dimensionless parameter

$$\beta = \frac{1}{B}\left(\frac{K}{\sigma_{ys}}\right)^2 , \tag{65}$$

where

B = specimen thickness,

K = critical value of stress-intensity factor,

σ_{ys} = yield strength.

For K_{Ic} testing, according to ASTM standard test method E399, $\beta \leq 0.4$. All the testing done on A533 grade B class 1 steel used 50.8-mm-thick specimens, and the K_{Ia} values appear to have been collected under a condition of plane strain, because they were consistent with values obtained on 150-mm-thick thermal shock tests. At room temperature, K_{Ia} = 107 MPa$\cdot\sqrt{m}$ and σ_{ys} = 473 MPa, so that β = 1.0 for the steel. Obviously, size requirements are less severe for K_{Ia} than for K_{Ic} testing.

Further definition of size requirements must be determined experimentally, and this is expected to require a large number of tests. To minimize sawing costs, A36 rather than A533 grade B class 1 steel is being used for these tests because A36 can be purchased in the range of thicknesses needed for these specimens.

Crack-arrest toughness tests have been run on 25.4- and 50.8-mm-thick specimens at room temperature. The results of these tests, along with the plate tensile properties, are shown in Tables 2.1 and 2.2. The toughness is identified as K_a rather than K_{Ia} because which, if any, of these results are plane strain is not known.

Table 2.1. Tensile properties of A36 steel at room temperature

Specimen No.	Plate thickness (mm)	Yield strength (MPa)	Tensile strength (MPa)	Elongation (%)	Reduction of area (%)
T-16	25.4	247	469	31.4	58.8
T-17	25.4	254	478	32.1	57.2
T-18	25.4	232	464	31.4	57.5
Average	25.4	242	470	31.6	57.2
T-7	50.8	255	492	32.9	65.3
T-8	50.8	240	472	33.6	64.7
T-9	50.8	252	490	30.0	66.6
Average	50.8	249	485	32.2	65.5

Table 2.2. Crack-arrest toughness of A36 steel at room temperature[a,b]

Specimen No.	Plate thickness (mm)	Specimen thickness (mm)	K_o (MPa·$\sqrt{m}$)	K_a (MPa·$\sqrt{m}$)	$\left[\frac{1}{B}\left(\frac{K}{\sigma_{ys}}\right)^{\beta}\right]^{2}$
A36-4	50.8	50.8	129	100	
A36-9	50.8	50.8	139	106	
A36-10	50.8	50.8	132	100	
Average	50.8	50.8		102	3.3
A36-1	25.4	25.4	167	154	
A36-2	25.4	25.4	167	149	
A36-7	25.4	25.4	158	141	
Average	25.4	25.4		148	14.5
A36-6	50.8	25.4	182	148	
A36-13	50.8	25.4	172	137	
A36-14	50.8	25.4	168	126	
Average	50.8	25.4		137	11.9

[a] β_N/B is constant at 0.75.

[b] Inplane dimensions are constant at 203 × 203 mm.

The strength properties and reduction in area of the thicker plate are somewhat higher than those of the thinner one (see Table 2.1). Nevertheless, the tensile properties of the two plates are similar. Conversely, the crack-arrest toughness of the two plates differed when tested in full thickness: the 50.8-mm plate had a toughness of 102 MPa·$\sqrt{m}$, while the 25.4-mm plate had a toughness of 148 MPa·$\sqrt{m}$. To determine whether this difference in toughness is a result of differences in plate properties or of the differences in specimen thickness, the top and bottom 12.7 mm of the thicker plate were machined off, and the plate was then tested as a 25.4-mm specimen. As shown in Table 2.2, testing the center section of the thicker plate gave a toughness value close to that of the thinner plate, suggesting, of course, that 25.4 mm is not sufficient thickness for obtaining plane-strain cracking with this plate. Incidentally, this occurred even though all fractures appeared to be cleavage to the eye and none of the specimens showed any indication of shear lips.

The values of β were 3.3 for the thicker specimen and 14.5 and 11.9 for the two thinner ones. Static yield strength values were used for these calculations, while arrest toughness is thought to correspond to K rates about six orders of magnitude faster than static.[28] The increase in yield strength associated with the running crack might be taken into account by adding about 40 MPa to the yield strength per order of magnitude of rate increase. This decreases the β values in Table 2.2 from 3.3, 14.5, and 11.9 to 0.86, 3.7, and 3.1, respectively. A similar "correction" of the yield strength of A533 grade B class 1 steel gives $\beta = 0.44$ for 50.8-mm-thick specimens tested at room temperature. Apparently, neither $\beta > 10$ (static yield strength) nor $\beta \approx 3.0$ (dynamic yield strength) can be associated with plane-strain cracking. Whether the values obtained with the thicker specimen, $\beta = 3.1$ (static yield strength) or $\beta = 0.83$ (dynamic yield strength), are plane strain cannot be ascertained from the available data.

To define the value of β that ensures plane-strain cracking, tests similar to those just described will be run at successively lower temperatures until the 50.8- and 25.4-mm-thick specimens give the same value of crack-arrest toughness.

2.2.5 ASTM K_{Ia} round robin

The three steels to be used on the Round-Robin Test Program have been located, and sawing of specimen blanks is expected to start in the next quarter. Actual testing, however, must await the decision on the type of brittle weld to be used and on the need for precompression. The information on size requirements need not be obtained prior to starting the round robin, however. Other than the delay in starting the round robin, no unexpected problems have arisen.

2.2.6 Compliance calibration of MRL and BCL compact crack-arrest specimens

Introduction. Both MRL and BCL supplied specimens of their own design to the Cooperative Test Program participants. The MRL specimen had the dimensions shown in Fig. 2.5, with the exception that the slot had the same width, N, from the loading hole to the edge of the specimen as it had from the hole to the crack-initiation notch. The BCL specimen had the dimensions shown in Fig. 2.6.

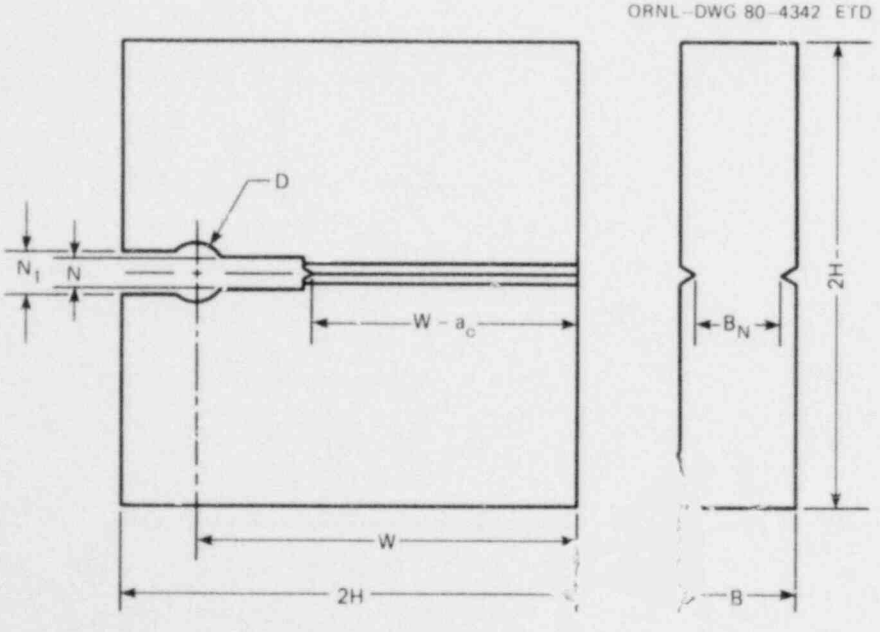

Fig. 2.5. MRL CCA specimen. W = 169.3; H = 1 1.6; B = 50.8; B_N = 0.75 B; W − a_o = 110.1; D = 25.4; N = 12.7; N_1 = 19.1. Dimensions in mm.

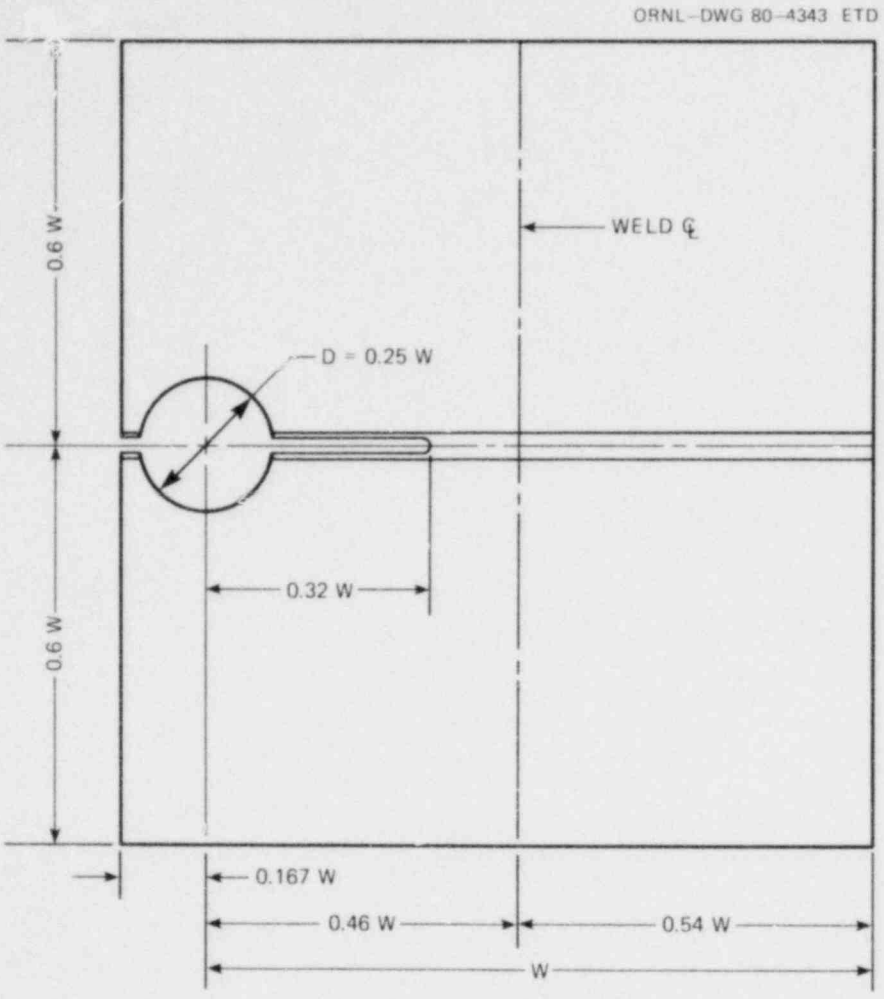

Fig. 2.6. BCL CCA specimen. W = 208 mm; B = 50.8 mm; B_N = 0.75 B.

The expressions supplied for calculating K for these specimens were based on analytical compliance calibrations developed by MRL and BCL, each for the laboratory's own test method.[27] Neither of the expressions was verified experimentally, and a need for doing so became apparent in the course of the Cooperative Test Program. The MRL test method used displacement measurements made at 0.25W from the centerline of the loading hole and assumed that there was no effect of loading hole pattern. Newman[29] had shown by means of a boundary collocation method that, for short crack lengths, displacements, Δ, at 0.25W were significantly affected by the loading hole pattern. Figure 2.7 shows the compliances,

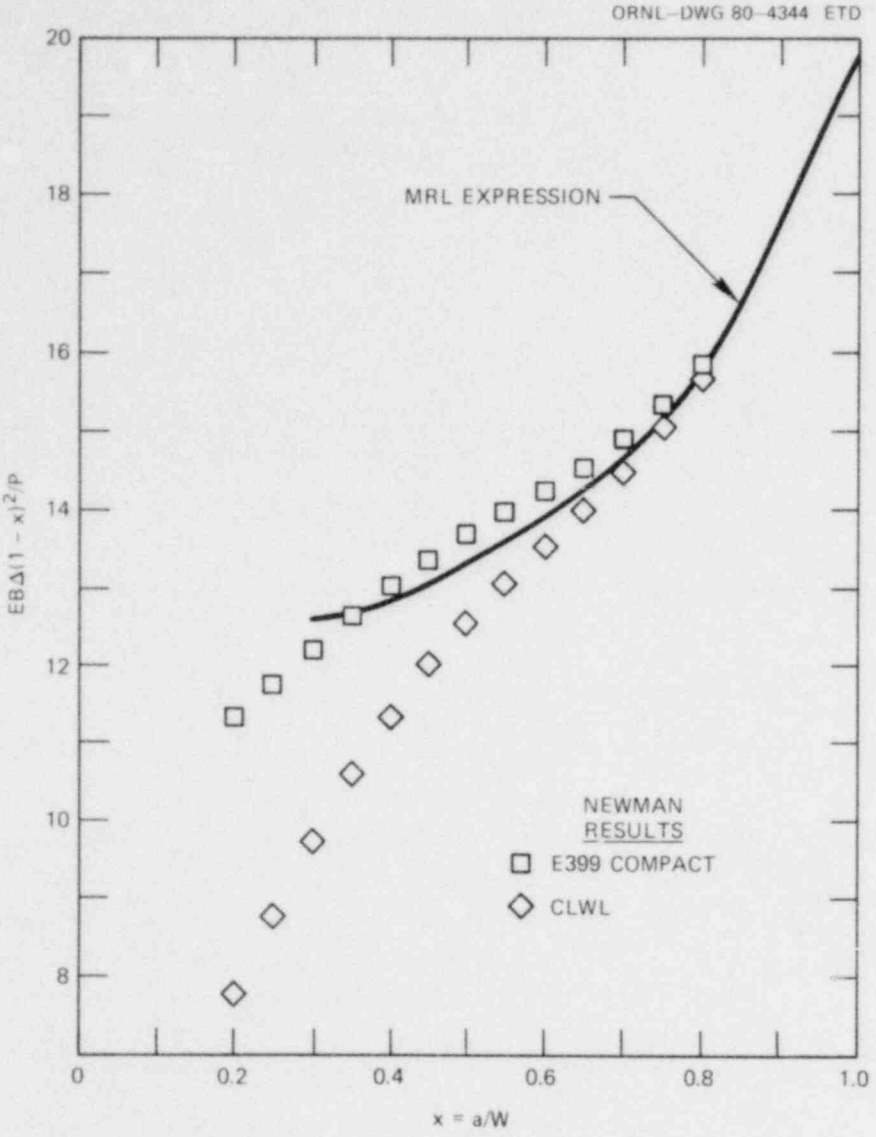

Fig. 2.7. Newman's results for load P and opening displacement Δ at 0.25W from load line for ASTM Standard E399 CLWL specimen. MRL expression supplied to Cooperative Test Program participants for K_{Ia} compact specimen shown for comparison.

according to Newman, for specimens using pin-hole loading and crack-line wedge-loading (CLWL), compared with the MRL expression supplied to the Cooperative Test Program participants.

The BCL test method measured displacement, y, on the split pins. The influence of hole pattern for displacements measured at the load line is small. Nevertheless, some measurements made by BCL directly on the

specimen load line, rather than on the split pin, suggested that the measurements made on the latter were not identical with load-point displacements.

Because of these uncertainties in the K expressions supplied to the Cooperative Test Program participants, both the MRL and BCL specimens were experimentally compliance-calibrated by relating the opening load to the displacement at the location where participants were asked to measure it.

MRL specimen compliance calibration. The experimental compliance calibrations were made with specimens like the one shown in Fig. 2.5. This configuration is identical to the K_{Ia} specimens tested in the Cooperative Crack-Arrest Program. The only difference was that a portion of the machined slot was wider (N_1 vs N in Fig. 2.5) to permit installation of the loading device. The calibration specimens, of course, did not have a machine-notched, brittle-weld crack starter; but the notch depth and configuration duplicated the final machined condition of the actual specimens. One calibration specimen was made from 7075 aluminum alloy for which Young's modulus was taken to be 69×10^3 MPa, and a second was made from SA533 grade B class 1 steel for which Young's modulus was taken to be 200×10^3 MPa.

To apply a load to the calibration specimens so that the load could be measured, two yokes were used. The yokes had cylindrical bearing surfaces that contacted the specimen loading hole just as the wedge-bushing loading device does in a K_{Ia} test. The assembly was installed in a test machine where load was measured with an inline load cell. A photograph of the test setup is shown in Fig. 2.8.

The opening displacement at 0.25W from the load line was measured exactly as it is measured in a K_{Ia} test. An aluminum target block and an aluminum transducer holder block were bolted to the front edge of the specimen to locate the centerline of the transducer at the desired measurement location. Prior to testing and at times during the testing, the transducer was calibrated in a micrometer stand over the same range of openings that would be sampled in the test. Plots of load vs opening displacement were made on an X-Y recorder.

Compliance calibration involved obtaining load, P, vs opening displacement, Δ, traces on the specimen in the original condition and with

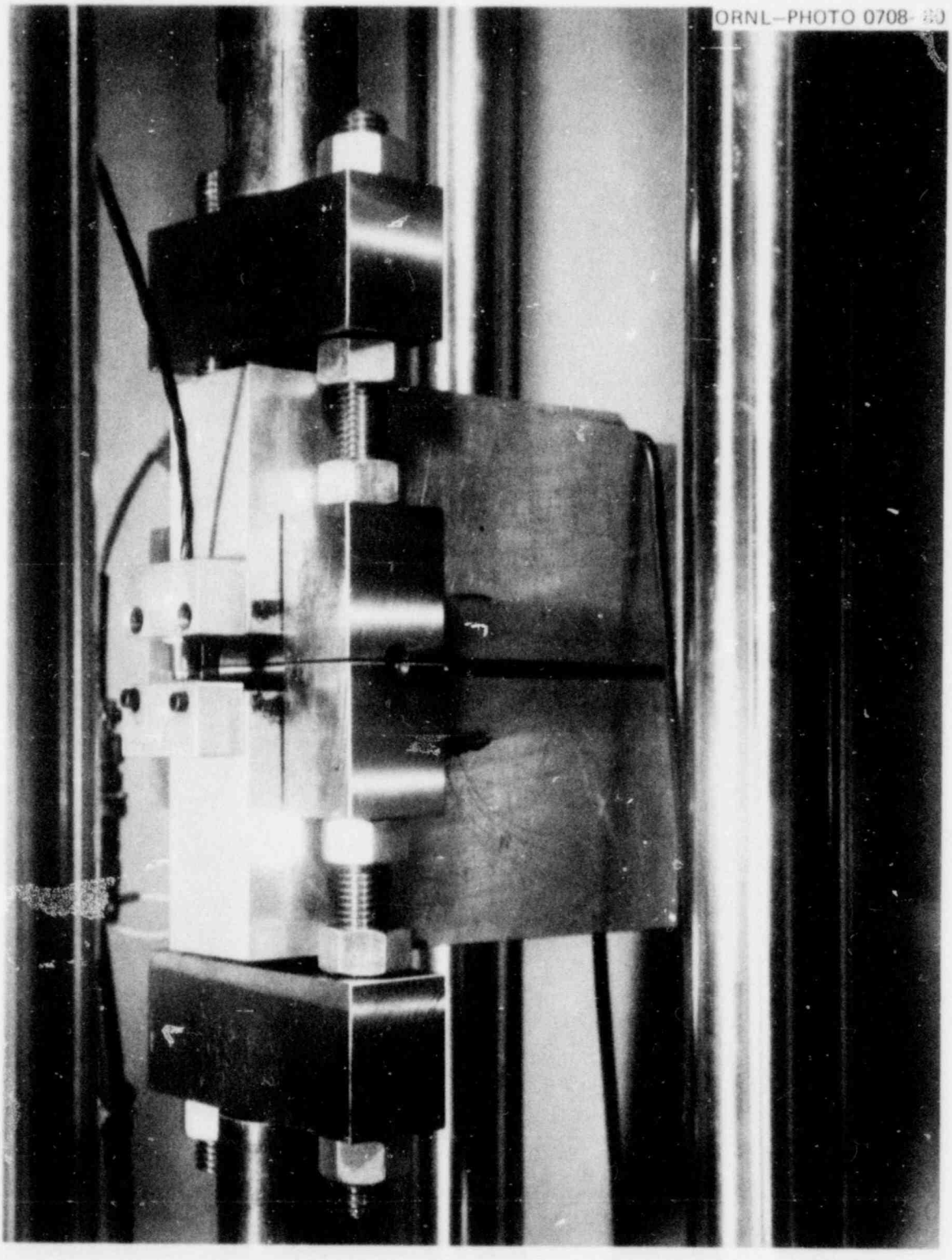

Fig. 2.8. Test setup for calibrating MRL CCA specimen.

saw cuts of different depths corresponding to different crack lengths. The sawing was done on a band saw which produced a 0.8-mm kerf. The compliance of a specimen with this amount of material removed is not expected to differ significantly from that of a specimen with a real crack, where no material is lost. The sawing was done in intervals of ~6 mm; the actual "crack" length at each stage was obtained by measuring W − a with a traveling microscope. Measurements on the two sides of the specimen generally agreed within 0.4 mm; the average of the two measurements was used to obtain the crack length, a.

The experimental results, given in Table 2.3, are plotted in Fig. 2.9 in terms of the quantity $EB\Delta(1 - x)^2/P$. Also shown is a least-squares parabolic fit to the data, which corresponds to

$$EB\Delta/P = (9.85 - 0.17x + 11.0x^2)/(1 - x)^2 \ . \qquad (66)$$

Comparison of this with the Newman results is as follows.

a/W	EBΔ/P (Newman, CLWL)	EBΔ/P [Eq. (66)]
0.30	19.90	22.0*
0.35	25.12	26.36
0.40	31.58	32.06
0.45	39.73	39.67
0.50	50.33	50.06
0.55	64.59	64.61
0.60	84.63	85.68
0.65	114.3	117.4
0.70	161.0	168.0
0.75	240.8	254.6
0.80	392.4	418.9

The curve fitted to the experimental data is compared with Newman's analytical results in Fig. 2.10. The difference is not large. The experimental results were obtained on the actual compact K_{Ia} specimen configuration, which has side grooves and a fairly wide starter notch; these features were not incorporated in the Newman analysis.

Newman has also presented a relation between K and P for a crack-line–loaded compact specimen using a boundary collocation analysis.[30]

*Extrapolated.

Table 2.3. Experimental calibration of MRL compact crack-arrest specimen[a]

W − a (mm)	Δ/P (m/GN)	a/W	EBΔ/P	EBΔ(1 − x)²/P
		Aluminum alloy		
		(E = 69 GPa; W = 169 mm; B = 50.8 mm)		
110.1	7.48	0.349	26.2	11.09
104.2	8.59	0.385	30.1	11.39
97.5	10.28	0.424	36.0	11.92
90.7	12.33	0.464	43.2	12.40
84.5	14.67	0.501	51.4	12.80
78.5	17.50	0.537	61.3	13.16
72.3	21.61	0.573	75.7	13.80
65.8	26.44	0.611	92.6	14.00
59.8	33.75	0.647	118.2	14.74
52.5	45.62	0.690	159.8	15.38
47.0	57.27	0.722	201.0	15.46
40.6	79.08	0.760	277.0	15.92
34.5	115.90	0.796	406.0	16.82
28.1	183.30	0.834	642.0	17.67
		Steel (A533 grade B class 1)		
		(E = 200 GPa; W = 169 mm; B = 50.8 mm)		
112.1	2.48	0.338	25.2	11.03
105.7	2.72	0.376	27.7	10.77
101.3	3.18	0.402	32.3	11.55
94.6	3.77	0.442	38.3	11.94
88.3	4.48	0.478	45.5	12.37
83.5	5.15	0.507	52.3	12.72
78.0	6.10	0.540	61.9	13.13
72.6	7.30	0.571	72.4	13.30
66.3	8.79	0.608	89.3	13.70
60.1	11.05	0.645	112.2	14.12
54.3	13.89	0.680	141.1	14.48
47.3	19.01	0.721	193.1	15.05
41.8	25.01	0.753	254.0	15.48
35.9	35.29	0.788	358.0	16.15
30.5	51.05	0.820	519.0	16.83
23.8	89.82	0.859	912.0	18.02
16.8	191.90	0.901	1949.0	19.21

[a]See Fig. 2.5 for definitions of dimensions.

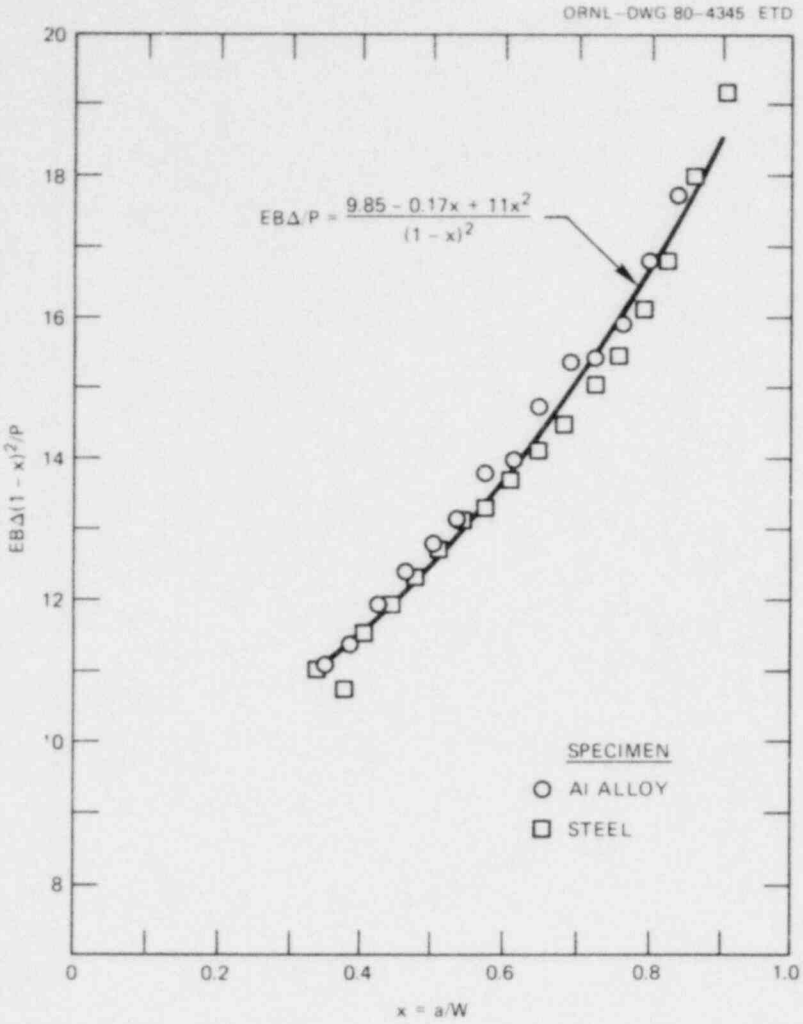

Fig. 2.9. Experimental compliance calibration of MRL CCA specimen.

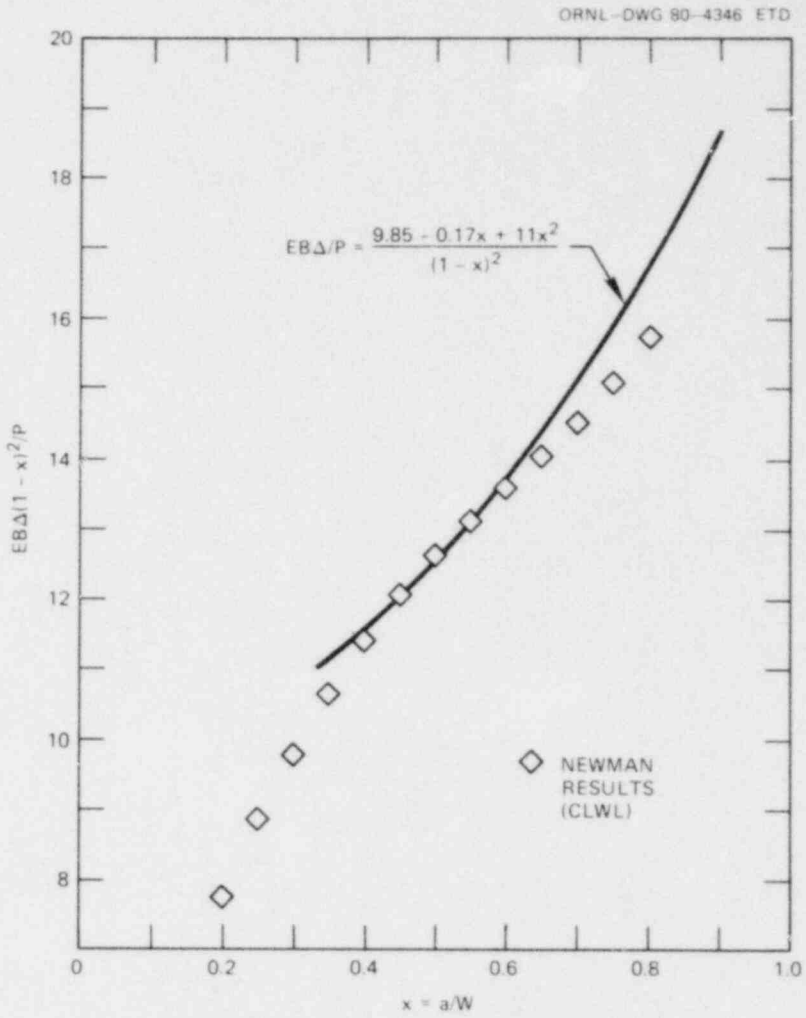

Fig. 2.10. Curve fitted to experimental calibration for MRL CCA specimen compared with Newman's results.

His data points for a smooth-sided specimen were fitted to the following polynomial by Rosenfield:[31]

$$KB\sqrt{W}/P = \frac{2.2434}{(1 - x)^{3/2}} (1.7164 - 0.9x + x^2) . \qquad (67)$$

Multiplying the right side of Eq. (67) by $(B/B_N)^{1/2}$ to account for the effects of side grooves and then combining Eqs. (66) and (67) gives the dependence of the dimensionless stress-intensity factor on dimensionless crack length shown in Eq. (63). A tabulation of this function is given in Table 2.4, and the function is plotted in Fig. 2.11.

This expression is the best available representation of the behavior of the MRL compact crack-arrest specimen and will be used for all future calculations of K_Q and K_{Ia} for this specimen.

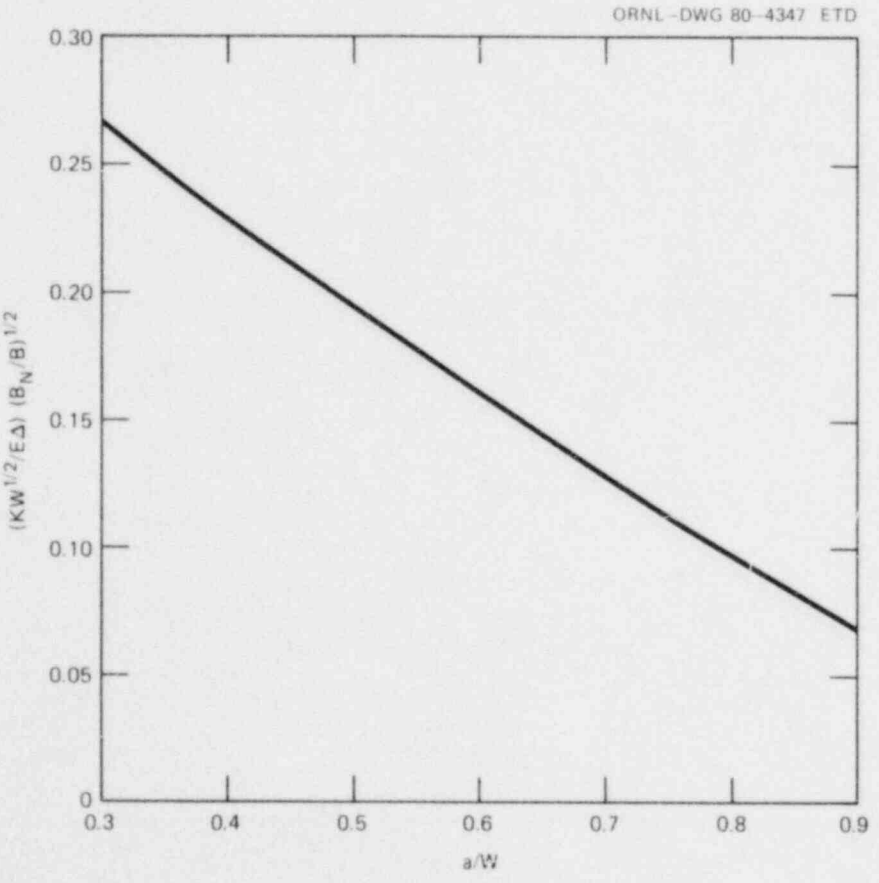

Fig. 2.11. Dimensionless stress-intensity factor as a function of dimensionless crack length for MRL CCA specimen.

Table 2.4. Dimensionless stress-intensity factor $(K\sqrt{W}/E\Delta)(B_N/B)^{1/2}$ as a function of dimensionless crack length, a/W

a/W	$(K\sqrt{W}/E\Delta)(B_N/B)^{1/2}$	a/W	$(K\sqrt{W}/E\Delta)(B_N/B)^{1/2}$
0.30	0.267	0.61	0.156
0.31	0.263	0.62	0.153
0.32	0.259	0.63	0.150
0.33	0.255	0.64	0.146
0.34	0.251	0.65	0.143
0.35	0.247	0.66	0.140
0.36	0.244	0.67	0.137
0.37	0.240	0.68	0.134
0.38	0.236	0.69	0.131
0.39	0.232	0.70	0.128
0.40	0.228	0.71	0.125
0.41	0.225	0.72	0.122
0.42	0.221	0.73	0.119
0.43	0.217	0.74	0.116
0.44	0.214	0.75	0.113
0.45	0.210	0.76	0.110
0.46	0.206	0.77	0.107
0.47	0.203	0.78	0.104
0.48	0.199	0.79	0.101
0.49	0.196	0.80	0.098
0.50	0.192	0.81	0.095
0.51	0.189	0.82	0.092
0.52	0.185	0.83	0.089
0.53	0.182	0.84	0.086
0.54	0.179	0.85	0.082
0.55	0.175	0.86	0.079
0.56	0.172	0.87	0.076
0.57	0.169	0.88	0.072
0.58	0.165	0.89	0.069
0.59	0.162	0.90	0.065
0.60	0.159		

BCL specimen compliance calibration. The BCL specimen used for experimental compliance calibration, like the MRL specimen, had dimensions identical with the specimens used in the Cooperative Test Program (Fig. 2.6). The specimen differed from the ones tested in that it was monolithic rather than being made of two pieces welded together. Only one specimen was calibrated, and it was made of SA533 grade B class 1 steel for which it was assumed that $E = 200 \times 10^3$ MPa.

Calibrating the BCL specimen was more difficult than calibrating the MRL specimens. To duplicate the displacement, y, measured by the Cooperative Test Program participants, the measurement had to be made on the two split-pin halves that are driven apart by the wedge. This prevents simultaneous measurements of y and opening load, P; thus, the calibration had to be carried out in two steps. The dependence of the displacement, Δ, at 0.25W on P was measured first, using a test setup essentially identical to that used for the MRL specimen calibration (Fig. 2.12). The second step then related the two displacements y and Δ by using two gages, one at 0.25W and a second across the two halves of the split pin, as shown in Fig. 2.13. The dependence of split-pin motion on load was obtained by combining these two sets of readings.

As with the MRL specimens, the first pair of measurements was made for the initial crack length, which, in this case, was a = 0.32W, after which the specimen was sawed to simulate crack extension, again leaving a 0.8-mm kerf. The saw cut intervals were about 12 mm long, and crack lengths were measured in the same manner as described previously for the MRL specimens. The first measurements were identical with those made on the MRL specimens, so the compliance values obtained on the larger BCL specimen could be compared with those obtained on the MRL specimen and with those obtained by the Newman analysis. As shown in Fig. 2.14, the differences between measurements of the two specimens and Newman's calculations are small. The experimental results are given in Table 2.5.

Unlike the first set of curves, the second set, Δ vs y, always had some curvature, and there was as much as 5% uncertainty in defining their slope. For all crack positions, at least four compliance lines were drawn (with both specimen types), so that some of the uncertainty in the Δ vs y curves might have been averaged out. The experimentally measured compliance and Newman's calculated values are compared in Fig. 2.15. A polynomial describing this experimental curve was combined with Eq. (67) with its right side multiplied by $(B/B_N)^{1/2}$ to arrive at the expression for K vs a for the BCL compact crack-arrest specimen given in Eq. (64). This expression is compared with the one supplied to the Cooperative Test Program participants in Fig. 2.16. The largest difference between the two expressions is about 10%.

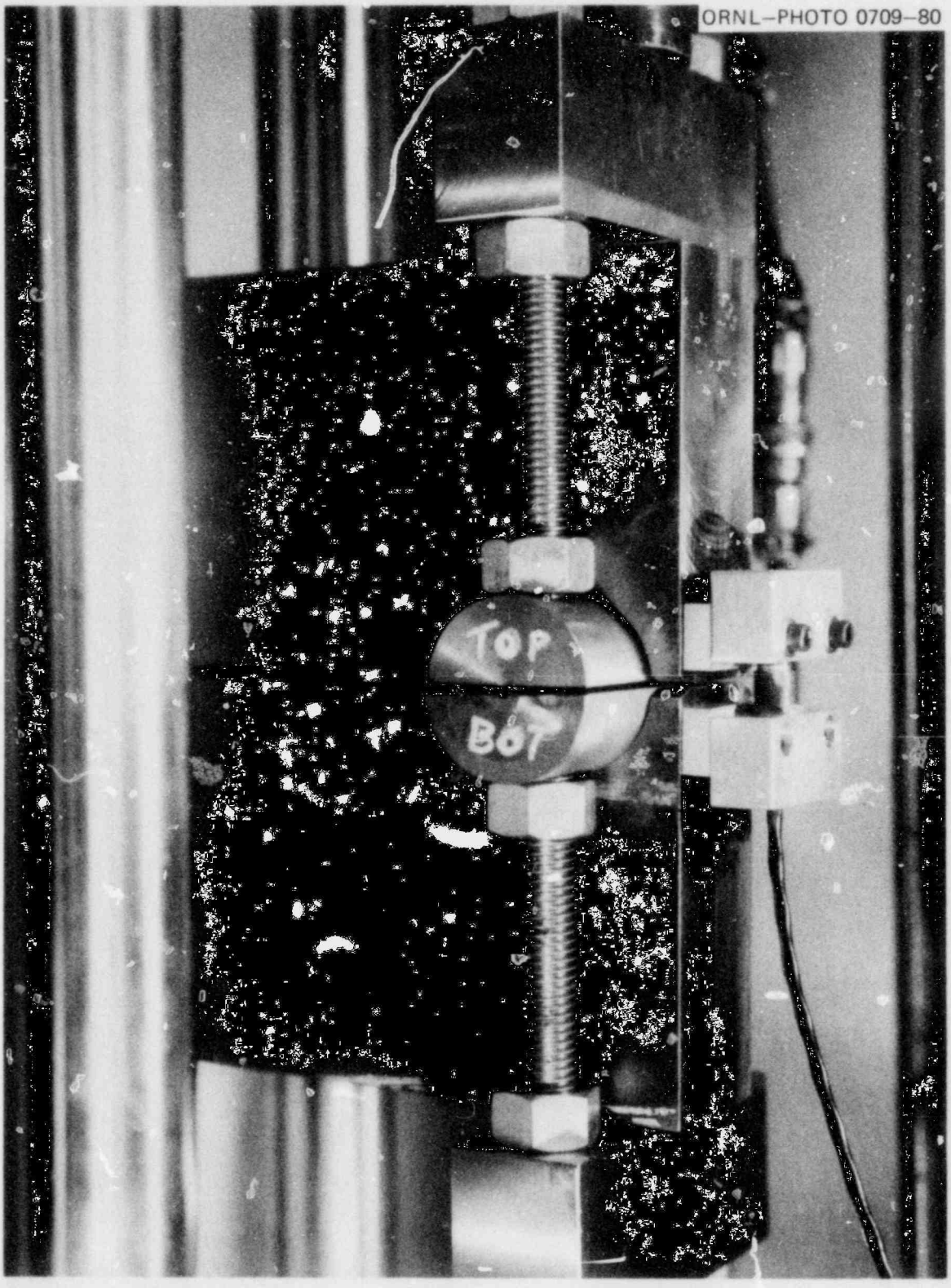

Fig. 2.12. Test setup for measuring dependence of displacement at 0.25W (Δ) on opening load for BCL CCA specimen.

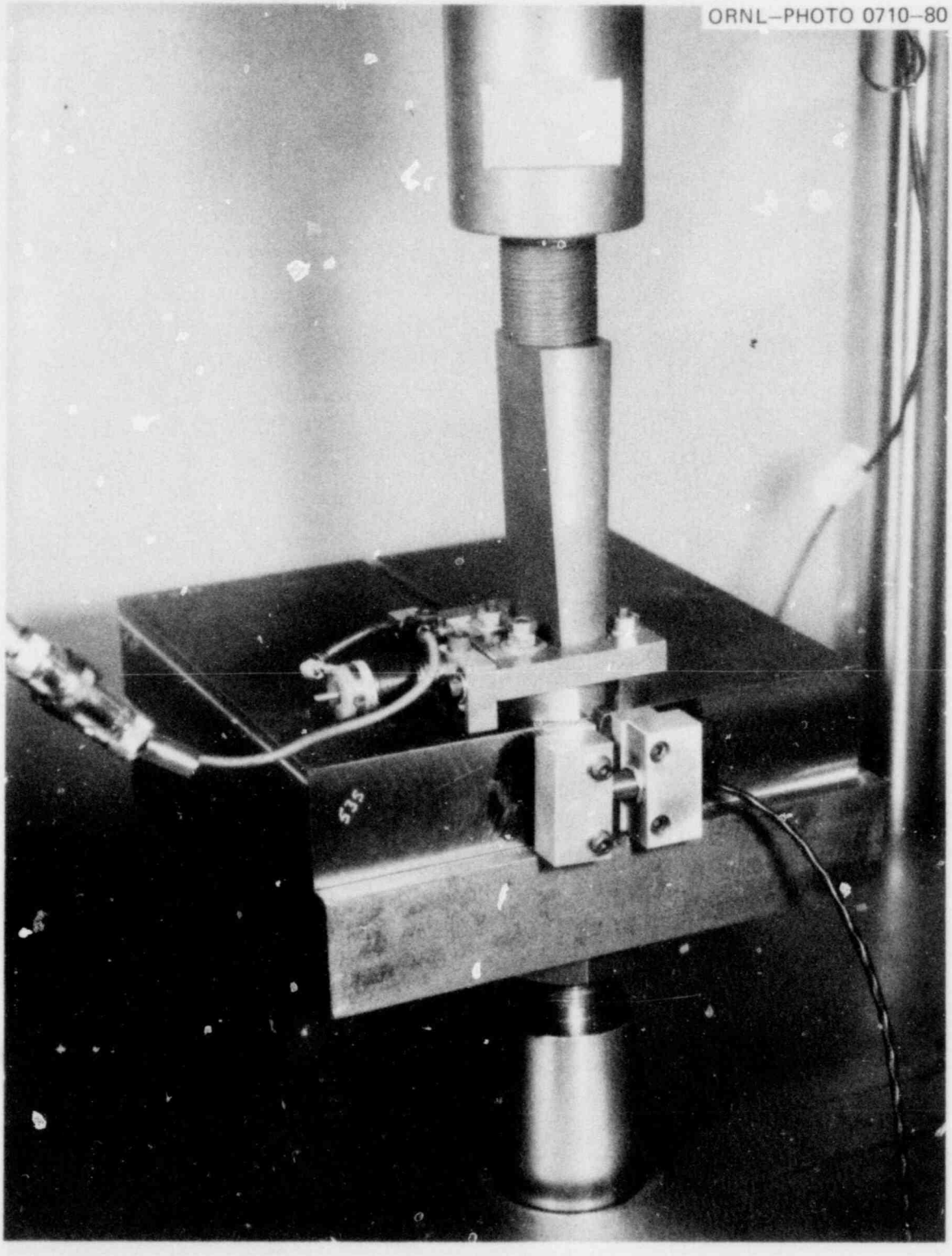

Fig. 2.13. Test setup for measuring the relationship of two displacements, Δ and y.

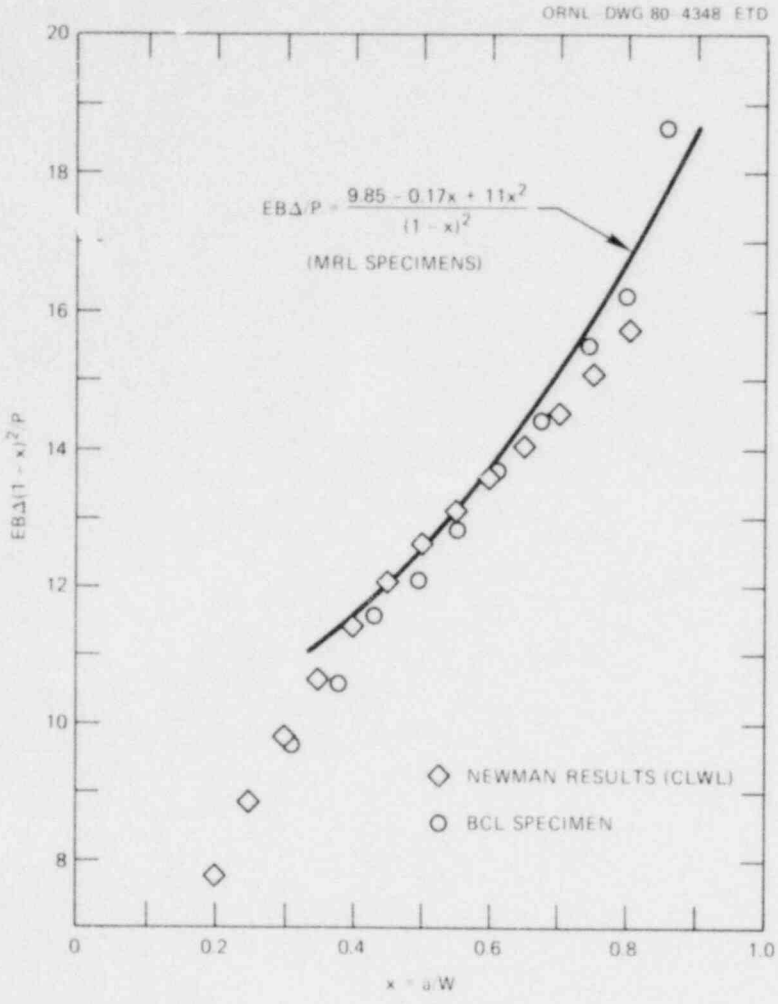

Fig. 2.14. Comparison of experimental compliance calibration of MRL and BCL specimens and Newman results.

Table 2.5. Experimental compliance calibration of BCL crack-arrest specimen[a,b]

a/W	Δ/P (m/GN)	y/Δ	y/P (m/GN)	EBΔ/P	$EB\Delta(1-x)^2/P$	EBy/P	$EBy(1-x)^2/P$
0.318	2.04	0.87	1.78	20.8	9.675	18.04	8.39
0.379	2.70	0.90	2.43	27.4	10.57	24.65	9.51
0.430	3.50	0.90	3.15	35.5	11.53	31.96	10.38
0.495	4.66	0.88	4.10	47.3	12.06	41.64	10.62
0.553	6.31	0.86	5.43	64.1	12.81	55.10	11.01
0.614	9.08	0.86	7.81	92.2	13.74	79.29	11.81
0.676	13.48	0.83	11.20	137.1	14.39	113.74	11.91
0.739	22.38	0.83	18.58	227.4	15.49	188.73	12.86
0.796	38.31	0.85	32.57	389.2	16.20	330.83	13.77
0.855	87.48	0.85	74.34	888.6	18.68	755.16	15.88

[a] Δ = displacement at 0.25W; y = displacement at load line on split pins; W = 208 mm; B = 50.8 mm; E = 200 GPa.

[b] See Fig. 2.6 for dimensions.

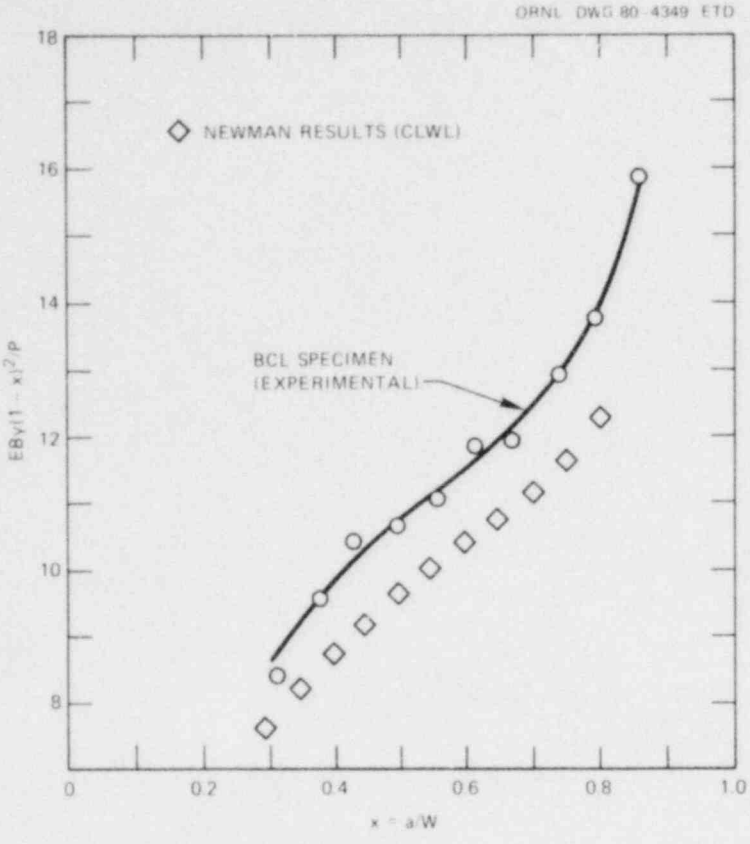

Fig. 2.15. Experimental compliance and Newman-calculated values for BCL CCA specimen compared.

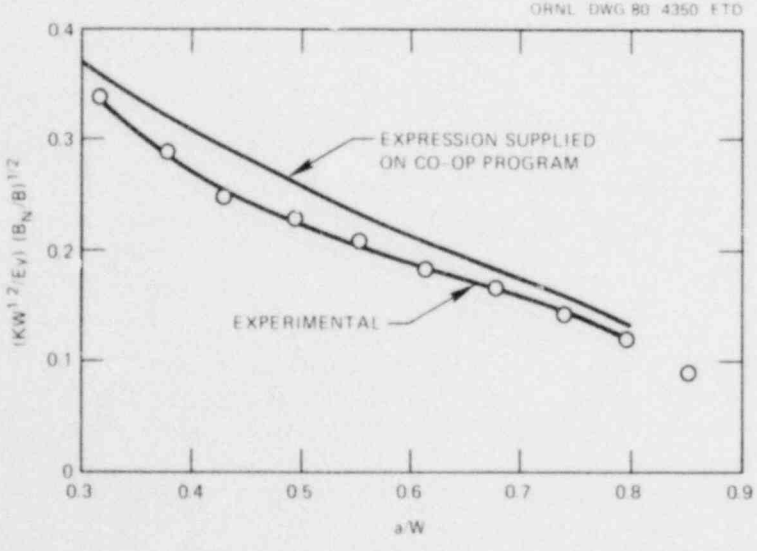

Fig. 2.16. Dimensionless stress-intensity factor vs dimensionless crack length for BCL CCA specimen.

2.3 Determination of K-Factors for Nozzle-Corner Flaws Under Combined Pressure-Thermal Loading

J. W. Bryson B. R. Bass*
W. G. Johnson* J. B. Blake*

Work was initiated this quarter on determining K_I distributions for quarter-circular–shaped nozzle-corner flaws under combined internal pressure-thermal loading. The MULT-NOZ,[32] ADINA,[33] ADINAT,[34] and BIGIF[35] computer codes are being used to perform this work. Several different sizes of nozzle-corner flaws in a boiling-water reactor (BWR) configuration (see Fig. 2.17) will be investigated under conditions simulating normal operating conditions of a BWR, that is, a combined internal pressure

*Computer Sciences Division, Union Carbide Corporation Nuclear Division.

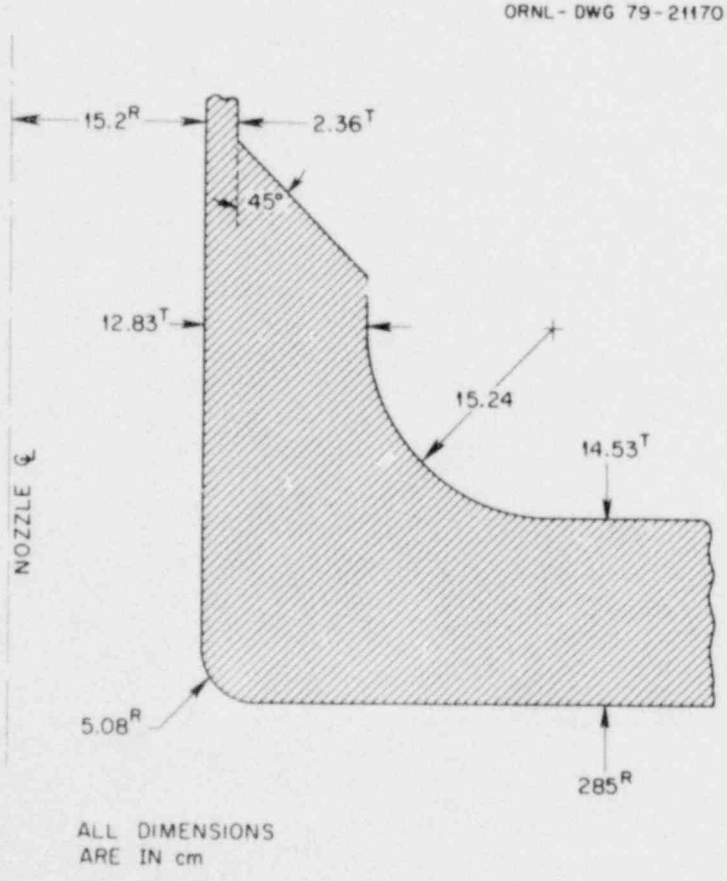

Fig. 2.17. Geometry and dimensions of a BWR feedwater nozzle.

loading (6.9 MPa) and a thermal environment (as shown in Fig. 2.18). This thermal environment represents steady-state data obtained at 97% power on November 12, 1975, at the Millstone Nuclear Power Station, Unit 1.[36]

The through-the-wall steady-state temperature distribution shown in Fig. 2.18 was obtained using ADINAT in conjunction with a finite-element mesh (see Figs. 2.19 and 2.20) generated by MULT-NOZ for an uncracked BWR feedwater nozzle configuration (Fig. 2.17). The steady-state nodal point temperatures were then input to ADINA, and a complete thermoelastic solution was obtained for the combined pressure-thermal loading. Normal stress (σ_y) contours for the longitudinal plane for both an internal pressure loading (6.9 MPa) acting alone and for the combined internal pressure-thermal loading are shown in Figs. 2.21 and 2.22, respectively. The imposed thermal environment elevates the maximum normal stress in the plane by ~25% (458 MPa at the inside nozzle corner for combined loading vs

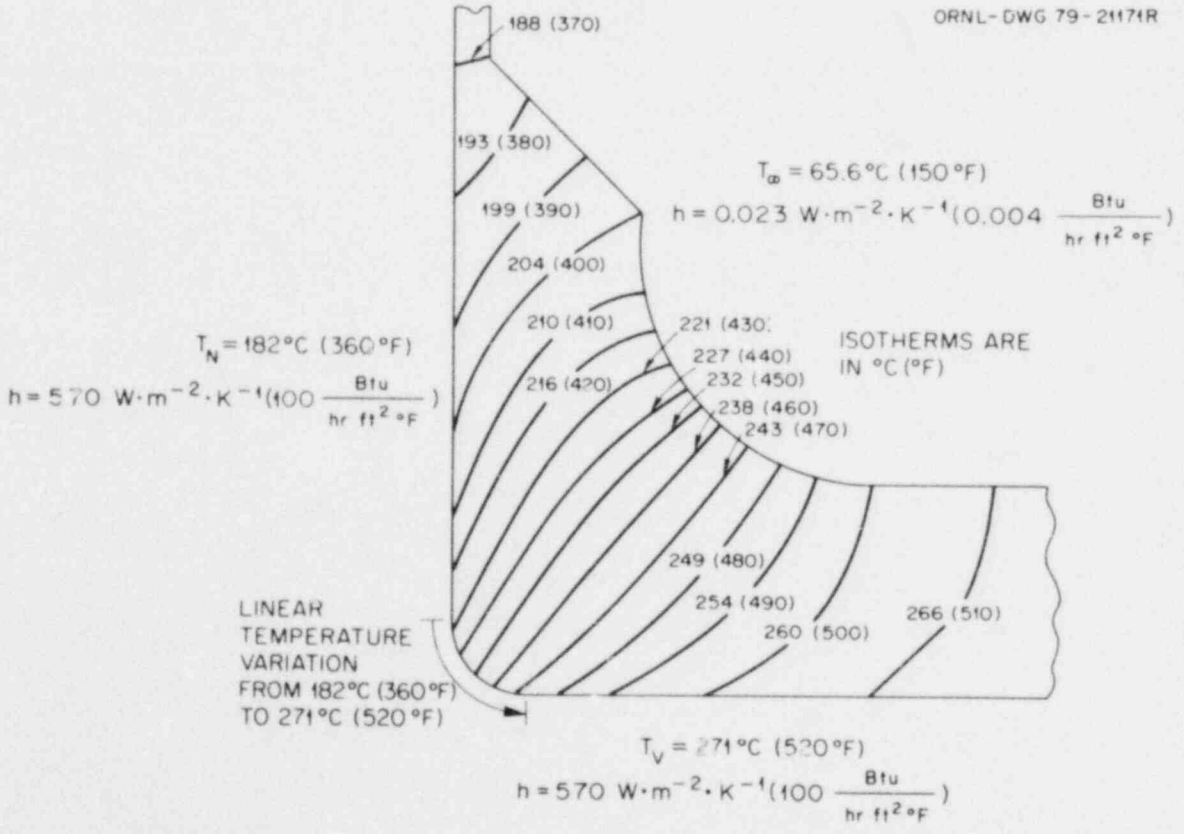

Fig. 2.18. Steady-state temperature distribution for BWR feedwater nozzle configuration, longitudinal plane.

ORNL–DWG 79–21172

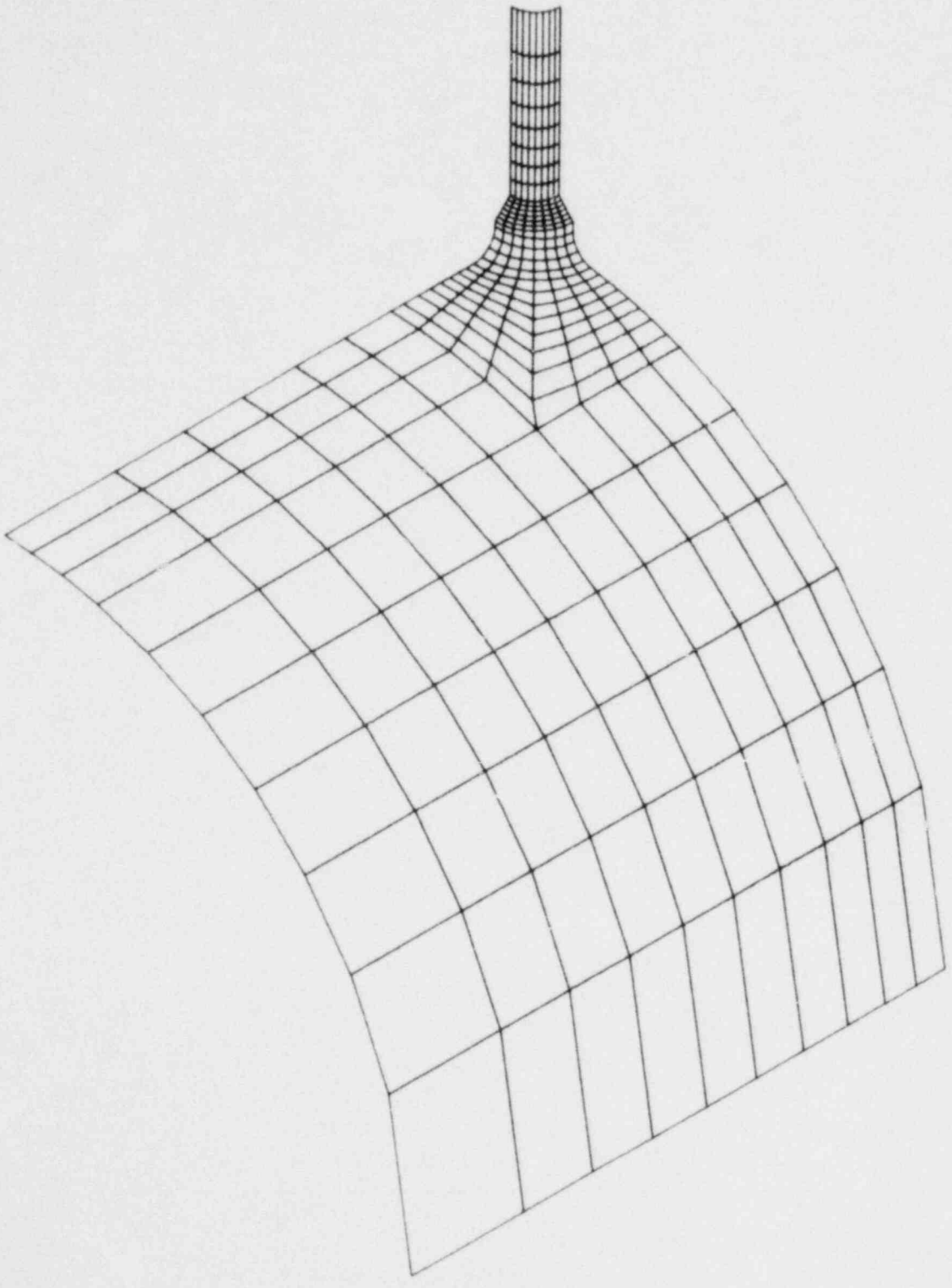

Fig. 2.19. Isometric view of generated mesh for BWR feedwater nozzle.

ORNL-DWG 79-21173

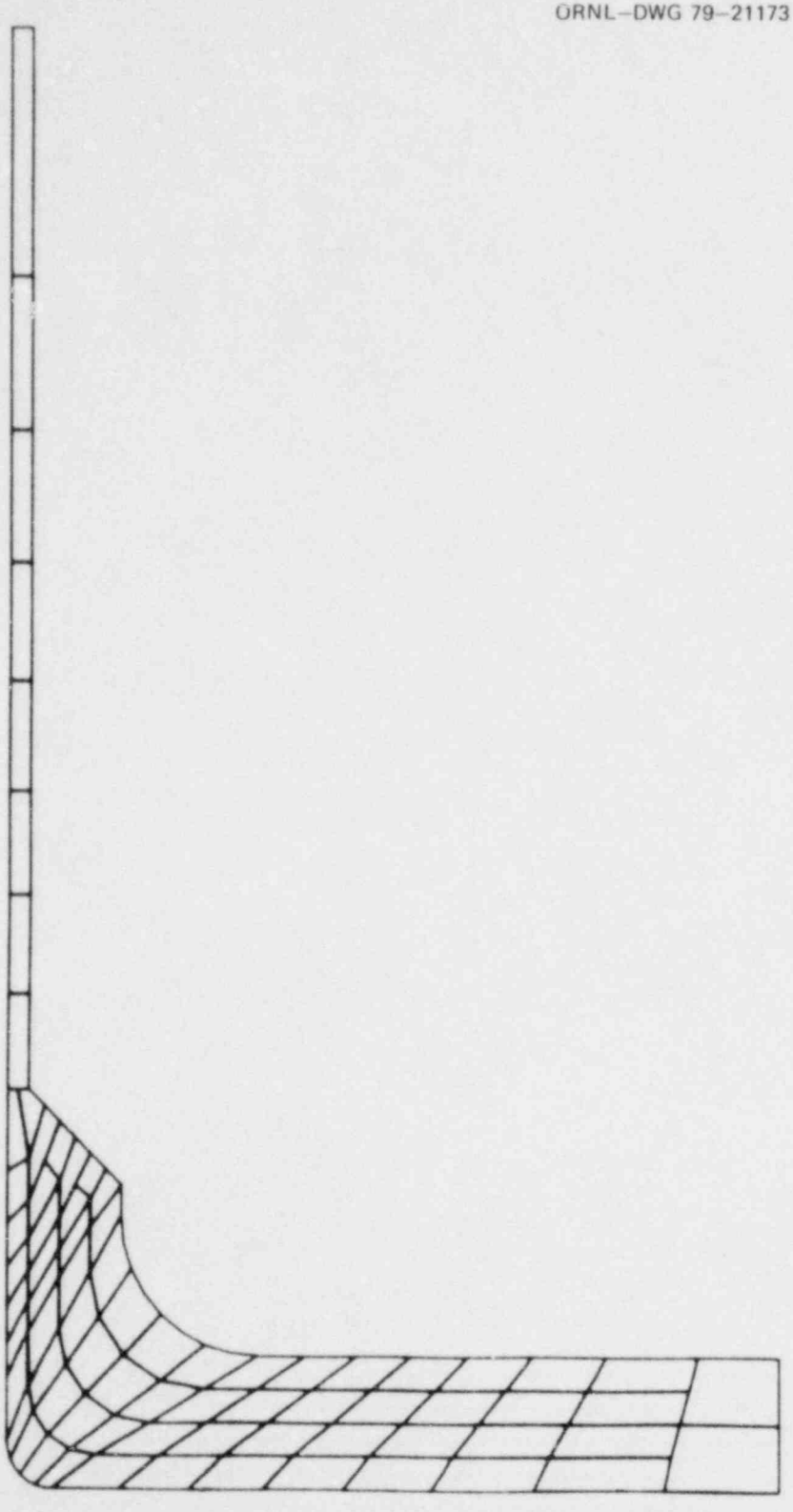

Fig. 2.20. Cross-sectional view of generated mesh for BWR feedwater nozzle, longitudinal plane.

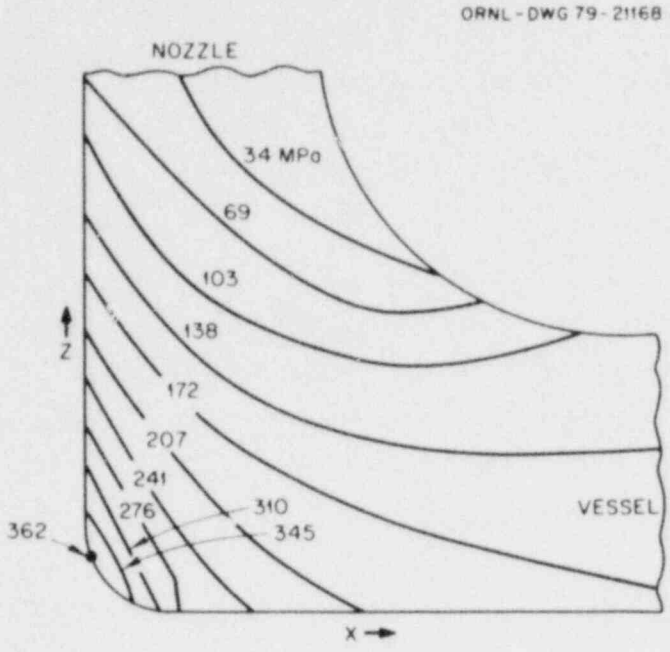

Fig. 2.21. Steady-state normal stress (σ_y) contours for internal pressure loading (6.897 MPa) acting alone, longitudinal plane.

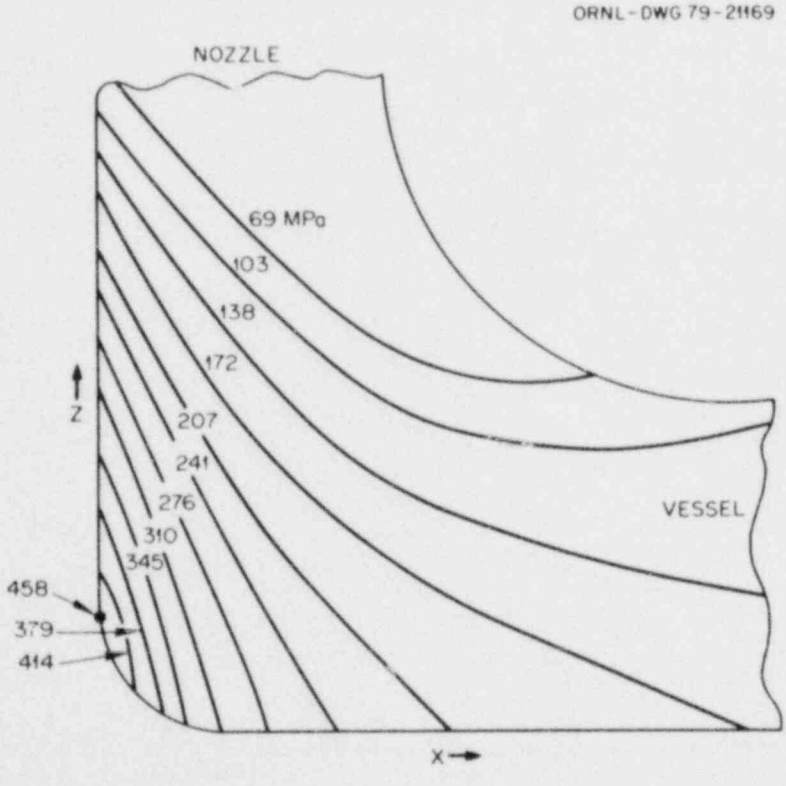

Fig. 2.22. Steady-state normal stress (σ_y) contours for combined pressure-thermal loading, longitudinal plane (P = 6.897 MPa; see Fig. 2.18 for thermal environment).

362 MPa for internal pressure acting alone). The uncracked stress distributions from ADINA will next be input to BIGIF, and K_I will be determined for several different flaw sizes. Comparisons of BIGIF results for combined pressure-thermal loading with results for pressure acting alone will demonstrate the relative effects of the thermal environment on the distribution of K_I.

A future problem of interest might be to determine a fully transient solution for a thermal shock situation. This would involve repeating these analyses for selected time intervals into the transient. One would then have both a spatial and a time variation of K_I for nozzle-corner flaws for prescribed pressure-thermal loadings.

In addition to the above work on quarter-circular-shaped flaws using BIGIF, similar investigations will be conducted for arbitrarily shaped flaws using the NOZ-FLAW computer program. This work is somewhat more involved, however, because a different mesh must be generated for each flaw shape considered and the corresponding ADINAT solutions for nodal point temperatures must be obtained.

2.4 Photoelastic Studies of Crack Propagation and Arrest*

W. L. Fourney†

2.4.1 Introduction

In the past, several groups of researchers have disagreed as to the best way to determine the ability of a material to arrest a propagating crack. In the forefront of this discussion have been Hahn et al. from BCL and Ripling and Crosley from MRL. The BCL researchers have contended that crack propagation is a dynamic event and that the possibility of energy transfer to the crack tip from kinetic sources should be considered in any analysis. Consequently, they base their determination of arrest toughness on a dynamic finite-difference computer code.

---

*Work sponsored by HSST Program under UCCND Subcontract 7778 between Union Carbide Corporation Nuclear Division and the University of Maryland.

†Department of Mechanical Engineering, University of Maryland, College Park, MD 20742.

Ripling and Crosley, however, state that the crack prior to arrest slows considerably in velocity and that conditions a few milliseconds after arrest should be a good approximation of conditions at arrest. They base the arrest toughness on measurements made just after arrest.

Both BCL and MRL were working with steel samples and had no sure way of determining which method was more accurate. Researchers at BCL were using the ladder gage technique to determine crack velocity, and there was some question whether the velocity on the surface was a good indication of the velocity at midthickness.

The group at the University of Maryland has been using dynamic photoelasticity with transparent birefringent polymers and could determine the stress-intensity factor at the tip of a running crack at any particular instant. The role of this group in the cooperative effort with BCL and MRL was to conduct fracture-mechanics tests with polymeric specimens to check the accuracy of both BCL and MRL methods of determining arrest toughness. Over the past five years, the technique of photoelastically determining stress-intensity factors has been refined and six reports describing the findings have been published.[37-42]

Some notable accomplishments include the following:

- developing $\dot{a}$ vs K relationships for Homalite 100, Araldite B, 4340 Steel, and several other tough epoxies;
- studying the behavior of a crack when propagating through a boundary between two materials with different degrees of toughness;
- examining crack-initiation stress-intensity decay;
- developing a photoelastic coating technique for use on brittle steel samples;
- developing dynamic analyses for photoelastically determining stress intensities;
- determining the higher-order terms necessary for accurate determination of K from isochromatics, isopachics, and caustics;
- determining damping in ring and compact tension specimens during crack propagation and after arrest;
- developing a two-dimensional finite-element computer code for predicting crack propagation behavior;

- examining BCL and MRL procedures for determining arrest toughness;
- participating in the ASTM Cooperative Test Program on Crack-Arrest Toughness.

Experiences over the past five years have led us to believe that damping is the major underinvestigated parameter in determining crack-arrest toughness. Concern exists about the effects that the late-breaking ligaments might have on the propagation distance; more should be known about the transition from brittle to ductile fracture. The effort during the coming year has been designed to answer these questions of concern.

Originally, funding was provided to conduct three separate tasks: task A, to perform dynamic two-dimensional finite-element computations to support findings in the following two tasks; task B, to examine more closely the effects of damping on the determination of K and propagation behavior; and task C, to examine the phenomenon of ductile-to-cleavage transition during fracture. A fourth, task D, has been added (to be funded with a savings realized in overhead charges): to examine further the effect of higher-order terms on the accuracy of K determination. In particular, concern here focuses on the effect of specimen size and shape on these higher-order terms. The principal elements of these four tasks are summarized in the following discussion.

Task A. A two-dimensional dynamic finite-element program, developed with the assistance of previous NRC funding, will be used to accomplish three subtasks.

1. Static and dynamic estimates of K for run-arrest events in configurations applicable in a nuclear reactor vessel will be compared. With the aid of task B, estimates will be provided of the need and magnitude of any dynamic supplement which should be applied when a static calculation of K is employed for purposes of predicting crack arrest.
2. Tasks B and C will be assisted by providing calculations of the crack-tip stress field for models of crack extension which employ late-breaking regions behind the crack tip.
3. Supplementary information will be provided on dynamic influences applicable to compact style crack-arrest toughness specimens. This

subtask will support development of an ASTM standard method for crack-arrest toughness evaluation.

Task B. The goal of task B is to conduct experimental model studies of damping and of late-breaking ligaments to accomplish the following subtasks.

1. Available equipment will be used for dynamic photoelastic stress analysis to study stress fields during run-arrest in models that contain late-breaking regions as suggested by task C.
2. Investigations of damping, including features observed in subtask (1), will be completed and summarized.
3. Applicability of these results to crack-arrest toughness testing and to estimates of applied K at crack arrest in a nuclear reactor vessel will be discussed.

Task C. The purpose of task C is to investigate two-phase, cleavage-fibrous fracturing in the following ways.

1. A search of technical literature will be conducted for previous work helpful to the task of modeling cleavage-fibrous fracturing.
2. Scanning electron microscopy (SEM) (stereo) and electron microprobe studies of fracture surfaces in the cleavage-fibrous transition range will be conducted, with special attention to late-breaking regions.
3. Plausible mechanical models of the stress-strain conditions that control cleavage-fibrous fracturing will be developed.
4. A plan will be recommended for developing adequate understanding of the cleavage-fibrous transition relative to use of J-R curves.

Task D. Past efforts to determine the effects of higher-order terms on K determinations from photoelastic data will be continued.

1. A determination will be made of the effect that the size of the specimen has on higher-order term contributions for a compact tension geometry.
2. The influence of the geometry on the higher-order terms for single-edge-notched (SEN), rectangular double-cantilever-beam (RDCB), and compact tension (CT) specimens will be determined.

2.4.2 Status of program

Two-dimensional computations. Work is under way to modify the finite-element code to accept input geometry and loading suitable to a nuclear reactor vessel configuration. Some comparisons with the thermal shock experiments conducted at Oak Ridge National Laboratory (ORNL) are anticipated to be available by the next report date.

The code is being used to investigate the possibility of crack surface impingement behind the running crack. This contact could result in large damping losses. These runs are under way, but no results are available at present. Various aspects of the code are still being checked out with respect to its ability to predict accurately a dynamic run-arrest event. Being investigated are such questions as effects of K vs å curve on output, accuracy of K levels predicted by the code compared with corresponding static calculations, and predicted load variations as the crack runs compared with experimentally obtained load vs time.

Photoelastic damping studies. Photoelastic experiments are being conducted to examine the effects of late-breaking ligaments on K levels at the crack tip. Preliminary experiments have been conducted, and the data are presently being analyzed. Additional experiments are anticipated because the material used to model the late-breaking ligaments was too tough and thus the effect on the singularity at the crack tip was too large.

Tests conducted to investigate damping in compact specimens as a function of size yielded interesting results. Data analyzed to date apparently indicate that not only does specimen size have an effect on damping but initial crack length also affects damping. As a result of these findings, additional testing is under way to investigate the effects of (1) specimen thickness, (2) initial crack length, and (3) specimen size on damping.

Some calculations have been completed which view the K level at the crack tip as being made up of two contributions: the normal singularity associated with the running crack and a contribution due to a strip-zone load which is located behind the crack tip. These results will be used to model either a curved crack front or a late-breaking ligament strip

zone traveling with the crack front. Preliminary results are particularly interesting with regard to the fringe patterns obtained for the 4340 CT specimens tested with birefringent coatings.

Cleavage-fibrous transition. A preliminary literature survey has been completed, and papers of particular interest are being reexamined in more detail. The problem of cleavage-fibrous fracturing is interesting to other investigators also, including the nuclear industry, the U.S. Army and Navy, and bridge designers.

A cooperative effort has been established with John Gudas, Naval Ship Research and Development Center, Annapolis, Maryland. He has obtained a special block of A533 grade B class 02 plate and plans to conduct ten special tests for this group that are designed to bring out features of interest in the cleavage-fibrous transition region. In addition to these tests, results will be available from tests conducted with other materials for the U.S. Navy. These should also be in a suitable range to bring out features of interest for the brittle-to-ductile transition region.

Higher-order terms. Tests are being designed to determine the effect of size on higher-order terms for CT specimens; these, however, will not start for another month.

2.4.3 Discussion

A discussion of the philosophy behind this testing program will give further clarification to this progress report. Five mechanisms exist for energy loss which warrant examination.

1. Energy loss is associated with the rapid drop in K from high pre-initiation K_Q values to a much lower K_D.

2. An energy loss occurs whenever energy is changed in form. For example, in Homalite 100, the static modulus of elasticity is much lower than the dynamic one. Thus, when the energy (even potential energy) goes from a static state to a dynamic one, a loss is involved as a result of the change in E.

3. If late-breaking ligaments are present, as in a steel specimen, energy can be lost in ligament formation. If the crack tends to close

behind the running tip, energy may be lost because of rubbing or impingement of these ligaments.

4. Energy is also lost because of the attenuation of stress waves.

5. Energy is lost in vibrations that are damped out after arrest occurs.

The first three sources of damping are the most important, and efforts are being concentrated along those lines. Tasks A and B of this program will help in understanding damping losses more clearly. A computer code is being used to analyze effects of late-breaking ligaments and strip-zone loadings on the stress intensity at the crack tip. In addition, photoelastic experiments are being run to determine the amount of damping in polymeric models. Investigations are being conducted on such questions as the effect of specimen size, shape, and thickness; K_Q level; and initial crack length on damping.

The third task is aimed at increasing understanding of the brittle-to-ductile transition in fracturing. By conducting electron microprobe studies of fracture surfaces, a plausible model of the stress-strain conditions which control cleavage-fibrous fracturing will be developed. The ultimate aim of this task is to recommend a plan for developing adequate understanding of the transition region relative to use of J-R curves.

The final task on higher-order terms that was added to the program will permit an increase in the accuracy of the K determination from the photoelastic data.

References

1. J. R. Rice, "Mathematical Analysis in the Mechanics of Fracture," chap. 3 in *Fracture, An Advanced Treatise*, vol. II, ed. by H. Liebowitz, Academic Press, New York, 1968.

2. J. R. Rice, "A Path Independent Integral and the Approximate Analysis of Strain Concentration by Notches and Cracks," *J. Appl. Mech., Trans. ASME* 90, 379–86 (June 1968).

3. A. Mendelson, *Plasticity: Theory and Application*, Macmillan, New York, 1968.

4. F. A. McClintock, "Plasticity Aspects of Fracture," chap. 2 in *Fracture, An Advanced Treatise*, vol. III, ed. by H. Liebowitz, Academic Press, New York, 1971.

5. A. A. Ilyushin, "The Theory of Small Elastic-Plastic Deformations," *Prikl. Mat. Mekh. [J. Appl. Math. Mech. (USSR)]* 10, 347 (1946); available in English translation at the David Taylor Model Basin, U.S. Department of the Navy, Washington, D.C.

6. A. Nadai, *Theory of Flow and Fracture of Solids*, 2d ed., vol. I, McGraw-Hill, New York, 1950.

7. N. L. Goldman and J. W. Hutchinson, "Fully Plastic Crack Problems: The Center-Cracked Strip Under Plane Strain," *Int. J. Solids Struct.* 11, 575–91 (1975).

8. D. F. Shih and V. Kumar, *Estimation Technique for the Prediction of Elastic-Plastic Fracture of Structural Components of Nuclear Systems*, First Semiannual Report to EPRI, General Electric Company, Schenectady, N.Y. (June 1, 1979).

9. H. Neuber, "Theory of Stress Concentration for Shear Strained Prismatical Bodies with Arbitrary Nonlinear Stress-Strain Law," *J. Appl. Mech., Trans. ASME* 28, 544–50 (December 1961).

10. V. Weiss, "Notch Analysis of Fracture," chap. 3 in *Fracture, An Advanced Treatise*, vol. III, ed. by H. Liebowitz, Academic Press, New York, 1971.

11. T. H. Topper, R. M. Wetzel, and J. Morrow, "Neuber's Rule Applied to Fatigue of Notched Specimens," *J. Mater.* 4(1), 200–209 (March 1969).

12. J. G. Merkle, "An Analytical Basis for Notch Sharpening by Fatigue," ASME Paper 71-PVP-46, presented at First National Congress on Pressure Vessels and Piping, San Francisco, Calif., May 10–12, 1971.

13. J. G. Merkle, *An Elastic-Plastic Thick-Walled Hollow Cylinder Analogy for Analyzing the Strains in the Plastic Zone Just Ahead of a Notch Tip*, ORNL/TM-4071 (January 1973).

14. R. W. Derby et al., *Test of 6-In.-Thick Pressure Vessels. Series 1: Intermediate Test Vessels V-1 and V-2*, ORNL-4895 (February 1974).

15. R. H. Bryan et al., *Test of 6-In.-Thick Pressure Vessels. Series 2: Intermediate Test Vessels V-3, V-4, and V-6*, ORNL 5059 (November 1975).

16. J. G. Merkle, "An Approximate Method of Elastic-Plastic Fracture Analysis for Nozzle Corner Cracks," *Elastic-Plastic Fracture*, ASTM STP 668, pp. 674–702 (1979).

17. J. R. Rice, "Mechanics of Crack Tip Deformation and Extension by Fatigue," *Fatigue Crack Propagation*, ASTM STP 415, pp. 247–311 (1967).

18. F. A. McClintock and G. R. Irwin, "Plasticity Aspects of Fracture Mechanics," *Fracture Toughness Testing and Its Applications*, ASTM STP 381, pp. 84–113 (1965).

19. A. B. Holt, "A Critical Evaluation of the Tangent Modulus Method of Elastic-Plastic Fracture Analysis," Paper G 3/6, *Transactions of the Fourth International Conference on Structural Mechanics in Reactor Technology*, San Francisco, Calif., August 15–19, 1977.

20. C. E. Turner, "Methods for Post-Yield Fracture Safety Assessments," chap. 2 in *Post Yield Fracture Mechanics*, ed. by D. G. H. Latzko, Applied Science Publishers, Ltd., Barking, Essex, England, 1979.

21. J. W. Hutchinson, "Singular Behaviour at the End of a Tensile Crack in a Hardening Material," *J. Mech. Phys. Solids* 16, 18–31 (1968).

22. S. S. Wang, "An Analysis of Tapered Double Cantilever-Beam Fracture Toughness Test for Adhesive Joints," *Fracture Mechanics*, ASTM STP 677, pp. 651–67 (1979).

23. G. R. Irwin, "Analysis of Stresses and Strains Near the End of a Crack Traversing a Plate," *J. Appl. Mech., Trans. ASME* 24, 361–64 (1957).

24. M. Creager, "The Elastic Stress Field Near the Tip of a Blunt Crack," Master's Thesis, Lehigh University (Sept. 20, 1966).

25. M. Creager and P. C. Paris, "Elastic Field Equations for Blunt Cracks with Reference to Stress Corrosion Cracking," *Int. J. Fract. Mech.* 3, 247–52 (1967).

26. S. H. Chang and F. J. Witt, "Application of the J-Integral to Obtain Some Similarity Relations," *Fracture Analysis*, ASTM STP 560, pp. 226–39 (1974).

27. G. T. Hahn, *Progress Report No. 5: A Program Status Report* (on the ASTM E24.01.06 Cooperative Test Program on Crack-Arrest Toughness Measurements), Battelle Columbus Laboratories (Feb. 23, 1979).

28. P. B. Crosley and E. J. Ripling, "Plane Strain Crack Arrest Characterization of Steels," *J. Pressure Vessel Technol., Trans. ASME* 97, 291 (November 1975).

29. J. C. Newman, Jr., *Crack-Opening Displacements in the Center-Crack, Compact, and Crack-Line-Wedge-Loaded Specimens*, NASA/TN D-8268 (July 1976).

30. J. C. Newman, Jr., "Stress Analysis of the Compact Specimen Including the Effects of Pin-Loading," *Fracture Analysis*, ASTM STP 560, p. 105 (1974).

31. A. R. Rosenfield, private communication.

32. F. K. W. Tso et al., *Stress Analysis of Cylindrical Pressure Vessels with Closely Spaced Nozzles by the Finite-Element Methods, Vol. 1. Stress Analysis of Vessels with Two Closely Spaced Nozzles Under Internal Pressure*, ORNL/NUREG-18/V1 (November 1977).

33. K. J. Bathe, *ADINA – A Finite Element Program for Automatic Dynamic Incremental Nonlinear Analysis*, Report 82448-1, Mechanical Engineering Department, Massachusetts Institute of Technology (May 1977).

34. K. J. Bathe, *ADINAT – A Finite Element Program for Automatic Dynamic Incremental Nonlinear Analysis of Temperatures*, Report 82448-5, Mechanical Engineering Department, Massachusetts Institute of Technology (May 1977).

35. P. M. Besuner, D. C. Peters, and R. C. Cipolla, *BIGIF: Fracture Mechanics Code for Structures*, NP-838, Failure Analysis Associates (July 1978).

36. International Atomic Energy Agency, *Fracture Mechanics Applications: Implications of Detected Flaws*, IAEA-189 (1976).

37. G. R. Irwin et al., *A Photoelastic Study of the Dynamic Fracture Behaviour of Homalite 100*, report to NRC under Contract No. AT(49-24)-0172, University of Maryland (September 1975).

38. G. R. Irwin et al., *A Photoelastic Characterization of Dynamic Fracture*, NUREG-0072 (NRC-5), University of Maryland (December 1976).

39. G. R. Irwin et al., *Photoelastic Studies of Crack Propagation and Crack Arrest*, NUREG-0342, University of Maryland (October 1977).

40. G. R. Irwin et al., *Photoelastic Studies of Crack Propagation and Arrest in Polymers and 4340 Steel*, NUREG/CR-0542, University of Maryland (December 1978).

41. H. P. Rossmanith and G. R. Irwin, *Analysis of Dynamic Isochromatic Crack-Tip Stress Patterns*, University of Maryland Department of Mechanical Engineering Report (July 1979).

42. G. R. Irwin et al., *Photoelastic Studies of Damping, Crack Propagation and Crack Arrest in Polymers and 4340 Steel*, report to NRC under Contract No. NRC-04-06-172, University of Maryland (November 1979).

3. INVESTIGATIONS OF IRRADIATED MATERIALS — FOURTH HSST IRRADIATION SERIES*

R. G. Berggren J. W. Woods
T. N. Jones D. A. Canonico

The first capsule of this irradiation series[1] is being irradiated at the Bulk Shielding Reactor (BSR) at ORNL. The specimen complement and design were previously described.[2]

Preirradiation testing of the capsule was completed. However, when the reactor was started up and the reactor power level was brought up to the normal operating level of 2 MW, specimen temperatures rose rapidly. The reactor power was immediately reduced to 1 MW, and specimen temperatures leveled out at about 270°C. This temperature level was reached with the high-conductivity gas (helium) in the capsule and without electrical heating. A series of tests was then conducted at lower reactor power levels and also with electrical heat only. These tests indicated errors in gamma heating values and heat transfer values used in the capsule design. The errors in gamma heating values were primarily due to using a gamma attenuation curve that did not account for back scattering from the water behind the capsule or for edge effects. Because redesign of the capsule did not appear necessary, the decision was made to install a steel thermal shield between the reactor and the capsule. Calculations indicated that a 60-mm steel thermal shield would reduce gamma heating and permit control of the specimen temperatures at 288°C. However, irradiation time for a given fast-neutron fluence will be about doubled. A temporary 60-mm-thick thermal shield was installed between the BSR and the capsule, and test runs were made at various reactor power levels, gas mixtures, and levels of electrical trim heat. These tests suggested that a thinner shield would provide the necessary shielding. A 42.5-mm-thick steel thermal shield and supports were designed, fabricated, and installed between the BSR and the capsule.

The capsule is operating with the BSR at full power (2 MW). Temperature control is excellent, with a maximum temperature difference of less

---

*Conversions from SI to English units for all SI quantities are listed on a foldout page at the end of this report.

than ±5 K for the 40 thermocouples in the capsule. The mean temperature is being controlled at 288 ± 2°C.

Parts for a neutron dosimetry experiment are being prepared for irradiation to determine fast-neutron fluxes and spectra in the capsule with the thermal shield in place. The length of time for irradiation of the capsule will be based on the results of this dosimetry experiment.

A similar thermal shield is being prepared for the second capsule of the irradiation series. This capsule and shield will be positioned on a different face of the BSR, and a neutron dosimetry experiment will be conducted for that position. Specimen preparation and initial steps of assembly for the second capsule are in progress.

References

1. R. G. Berggren et al., "Toughness Investigations of Irradiated Materials," *Heavy-Section Steel Technology Program Quart. Prog. Rep. January–March 1979*, ORNL/NUREG/TM-324, p. 56.

2. R. G. Berggren et al., "Toughness Investigations of Irradiated Materials," *Heavy-Section Steel Technology Program Quart. Prog. Rep. July–September 1979*, ORNL/NUREG/TM-370, chap. 4.

4. THERMAL SHOCK INVESTIGATIONS*

R. D. Cheverton S. E. Bolt
S. K. Iskander

4.1 Introduction

During this report period for the Thermal Shock Experiment (TSE) Program, the posttest analysis of TSE-5 was continued, material used for the TSE-5 test specimen was further characterized, and calculations pertaining to the next proposed thermal shock experiment were conducted.

4.2 Posttest Analysis of TSE-5

4.2.1 Synopsis of TSE-5 and preliminary posttest analysis

Thermal shock experiment TSE-5 was conducted on August 1, 1979, and consisted of quenching the inner surface of a thick-walled steel cylinder with liquid nitrogen. The cylinder contained an inner-surface long axial flaw, and the initial temperature of the cylinder was 96°C. Conditions for the experiment are summarized in Table 4.1.

Anticipated results of TSE-5, based on expected heat transfer conditions and specified and assumed material properties, are discussed in ref. 1, and a preliminary posttest analysis is included in ref. 2. This latter analysis indicated that the material toughness was considerably less than expected for temperatures above 0°C. As a result, conditions for demonstrating warm prestressing (WPS) and arrest in a rising K_I field were not achieved. However, multiple initiation-arrest events, initiation and arrest of both shallow and deep flaws, and a long crack jump were achieved; and the preliminary posttest analysis of these events indicates that LEFM is valid for severe thermal shock conditions.

This tentative conclusion regarding the validity of LEFM is based on the assumption that material toughness values deduced from TSE-5 can be obtained with laboratory-size specimens. Material characterization studies under way at this time indicate that indeed the toughness is much

*Conversions from SI to English units for all SI quantities are listed on a foldout page at the end of this report.

Table 4.1. Test conditions for TSE-5

Test specimen	TSC-1
Test specimen dimensions, m	
OD	0.991
ID	0.686
Length	1.22
Test specimen material	A508 class 2 chemistry
Test specimen heat treatment	Tempered at 613°C for 4 h
K_{Ic} vs temperature curve specified	HSST plate 02
K_{Ic} and K_{Ia} curves used in TSE-5 final design analyses	ASME Section XI, Appendix A, RT_{NDT} = −34°C
Flaw	Long axial sharp crack, a = 16 mm
Temperatures, °C	
Wall (initial)	96
Sink	−196
Coolant	LN_2
Flow conditions	Natural convection loop
Coating on quenched surface	Rubber cement (3M-NF34)
Coating thickness, mm	0.8

less than originally expected on the basis of the pretest characterization studies. Furthermore, the results indicate, as suggested by Landes,[3] that crack behavior in large structures, such as the TSE-5 test cylinder, is governed by lower-bound toughness as derived from laboratory-size fracture specimens. Results of the ongoing material characterization studies are discussed in refs. 4 through 7 and in Sect. 4.4 of this report.

4.2.2 COD measurements

Crack-opening displacement (COD) gages in the form of Ailtech weldable strain gages were used during TSE-5 to (1) detect initiation-arrest events, (2) obtain absolute values of COD, and (3) measure COD rate.

Seven gages located along the length of the flaw were used for event indicators and COD measurements, while two gages near midlength were used for the COD rate measurements. Specific locations for the gages and a preliminary interpretation of the data are included in ref. 2.

As part of the preliminary posttest analysis of the COD data, an attempt was made to obtain absolute COD values by multiplying the output strain by an effective gage length equal to the published nominal gage length. These results were compared with the results of the posttest finite-element analysis of TSE-5, and agreement between measured and calculated COD was not very good. Even so, the measured COD vs time data from the fast-phenomena digital recorder were used in conjunction with the calculated relation between COD and crack depth to estimate the initial crack velocity for the second initiation-arrest event in TSE-5. The initial velocity was the maximum recorded during the run event, and a value of 180 m/s was calculated and reported in ref. 2.

Recently, the Ailtech gages were calibrated under simulated TSE-5 conditions. As shown in Fig. 4.1, a gage was applied to a 29-mm-diam stainless steel circular bar that was mounted in an MTS testing machine and cut in two at midlength of the gage. As with TSE-5 and previous thermal shock experiments,[8] the central portion of the gage was left unattached to the two bars for a length of 10 mm.

Prior to a gage calibration test, the strain gage recording equipment was calibrated by shunting in an appropriate resistance, and the displacement-measuring instrumentation was calibrated by comparing the output from three separate and different displacement gages. Subsequent calibration of the Ailtech gage consisted of first achieving the desired testing temperature and then loading the gage at a rate of 0.127 mm/min until the gage failed or reached a desired limit. One test was run at room temperature, and two were conducted at −196°C (liquid nitrogen). For the two low-temperature tests, the gages were subjected to an initial tensile strain of ~1.5% that resulted from thermal contraction of the strain gage and the two bars because the clamped ends of the bars were fixed in position during cooling.

Test results provided a plot of relative displacement of the ends of the bars vs output of the strain gage, and the slopes of the three curves

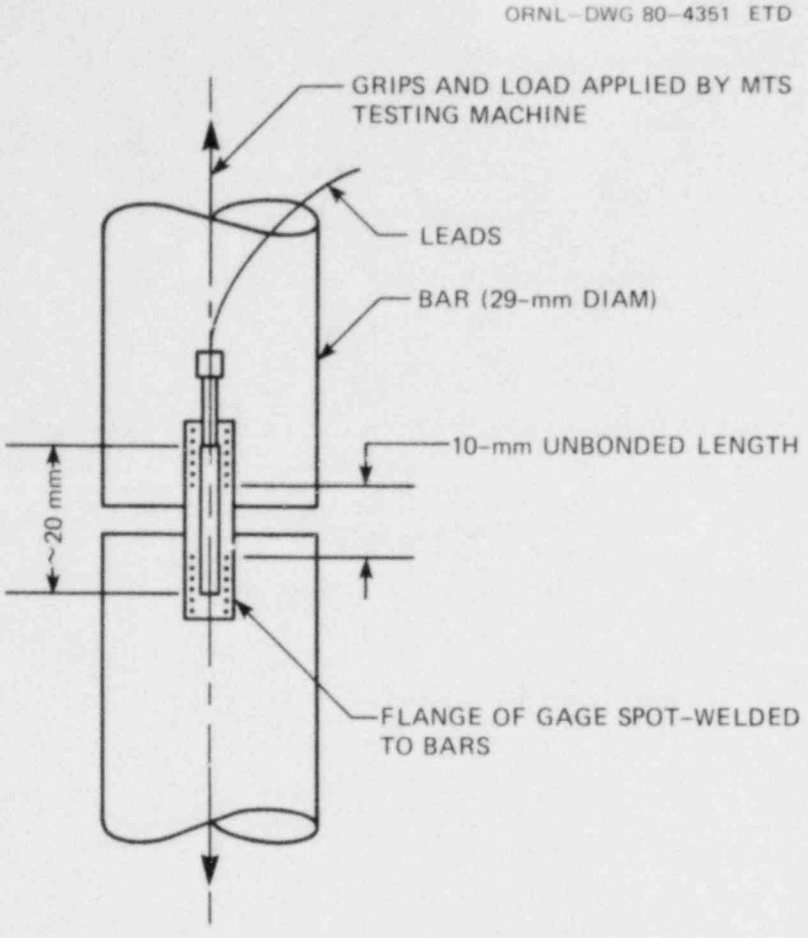

Fig. 4.1. Mounting of Ailtech SG-125 gage for strain vs displacement calibration.

were essentially constant. For the room-temperature test, the slope of the curve was 0.043 mm^{-1}, and the test was stopped at 5% strain. The slopes of the curves for the two gages tested at −196°C were 0.039 and 0.041 mm^{-1}. These gages were tested separately and were loaded to failure; the strains at failure were 7.5 and 6.6%, respectively. Interestingly, the strain was concentrated over approximately one-half the length of the gage (i.e., the unbonded length). Thus, the local strain at failure was ~14%. The maximum COD during TSE-5 corresponded to a COD gage strain output of ~6.5%. Some of the COD gages failed before reaching this level and some did not.

A comparison of calculated and measured COD values, using the above calibration data, is presented in Table 4.2 for the three initiation-

Table 4.2. Measured and calculated CODs (mm) for the three initiation-arrest events in TSE-5

a/w	Event number and time of occurrence					
	1 (t = 106 s)		2 (t = 178 s)		3 (t = 206 s)	
	Experimental	Calculated	Experimental	Calculated	Experimental	Calculated
0.10	0.172	0.150				
0.20	0.30	0.28	0.38	0.35		
0.63			1.02	1.22	1.07	1.27
0.80					1.45	1.65

arrest events in TSE-5; the revised maximum crack velocity for the second event is 230 m/s. Table 4.2 shows that for the shallow flaws the calculated value of COD is somewhat less than the measured value (13% for a/w = 0.10 and 6 and 9% for a/w = 0.20), while for the deeper flaws the calculated value is greater than the measured value (20 and 19% for a/w = 0.63 and 14% for a/w = 0.80). The differences are probably within the accuracy of the measurements and calculations. However, the trend is consistent with the three-dimensional effect that developed as the flaw propagated deeper into the wall. As discussed in ref. 2, propagation was not so great near the end of the test cylinder as it was near midlength, and the variation was greater as the crack grew deeper. The calculation, however, is for a two-dimensional model and thus tends to overestimate the ratio COD/(a/w) as the axial nonuniformity increases with crack depth. If indeed the trend is due to this effect, then the calculated K_I values for the deep flaws would also be too high. Thus, the K_{Ic} values deduced from TSE-5 for the deeper flaws and consequently higher temperatures should perhaps be less than those reported in ref. 2. This question may be resolved by conducting a three-dimensional analysis of TSE-5.

4.2.3 Secondary cracking

As discussed in ref. 2, cracking other than that associated with the long axial crack took place during TSE-5. This secondary cracking was on the inner surface and initiated at a small cross crack in the electron-beam (EB) weld that was used to generate the long axial flaw. As indicated in Fig. 4.2, the cross crack initially extended from one end in a circumferential direction and then started branching. Many branches turned in an axial direction and terminated at or near the ends of the cylinder. Several circumferential branches effectively extended ~360°, terminating at or near the long axial flaw. Apparently, none crossed the latter flaw; this indicates that the secondary cracking occurred after the primary cracking (axial flaw). Another indication of this timing is that there are no secondary axial cracks close to the axial flaw, yet the secondary circumferential flaw extended the entire circumference. Existence of a deep primary axial flaw would relieve the circumferential stresses in

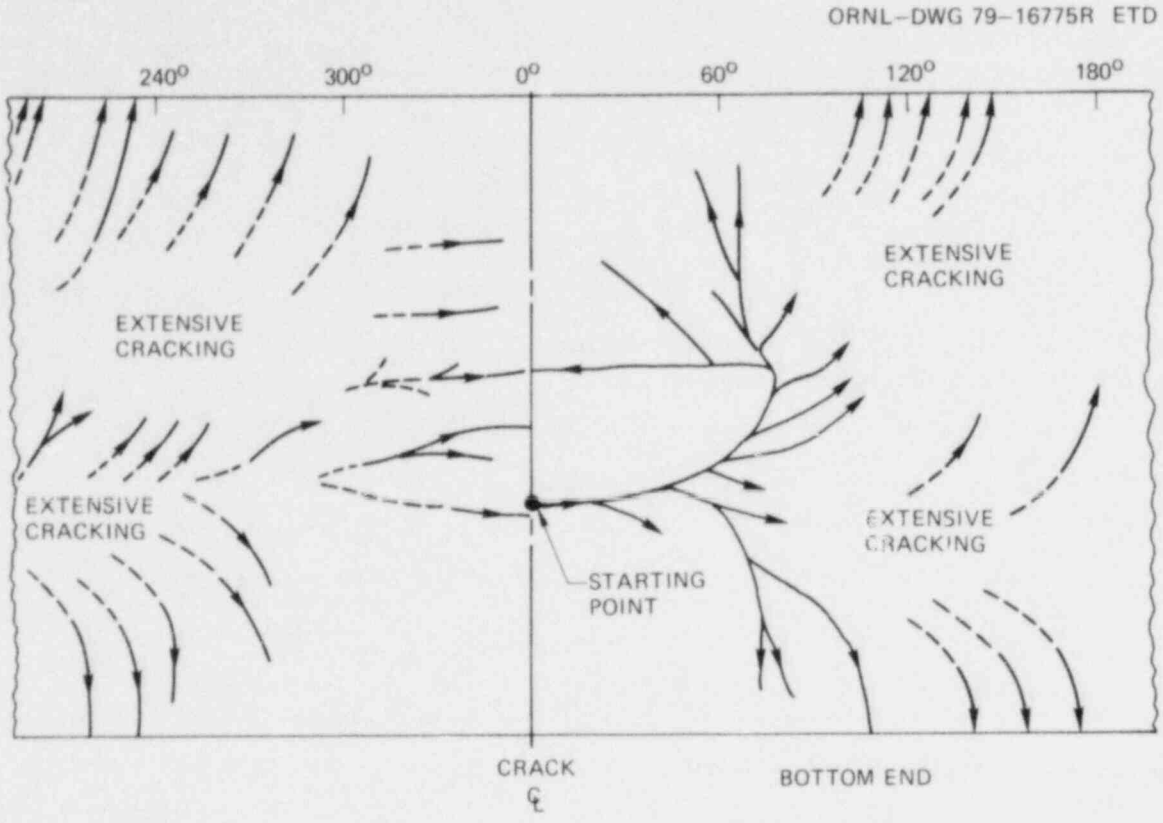

Fig. 4.2. Secondary cracking during TSE-5 (layout of inner surface of TSC-1).

the vicinity of this flaw, thus preventing the formation of secondary axial flaws in this area but not preventing the extension of the circumferential branches.

In an effort to help understand the effect that the secondary cracking might have on the behavior of the primary crack, depending on the relative times of occurrence, additional fracture mechanics calculations were made with seven and nine secondary axial flaws in addition to the primary flaw. The secondary cracks were spaced about 30° apart (as shown in Fig. 4.3) starting 180° from the primary flaw. The fractional crack depth for these cracks was 0.35, and, for the primary crack, two depths were considered: $a/w = 0.1$ and 0.8. All calculations were made for a time of 7 min in the TSE-5 transient, since the COD for the primary crack was a maximum at this time. The calculational model was two-dimensional finite-element LEFM.

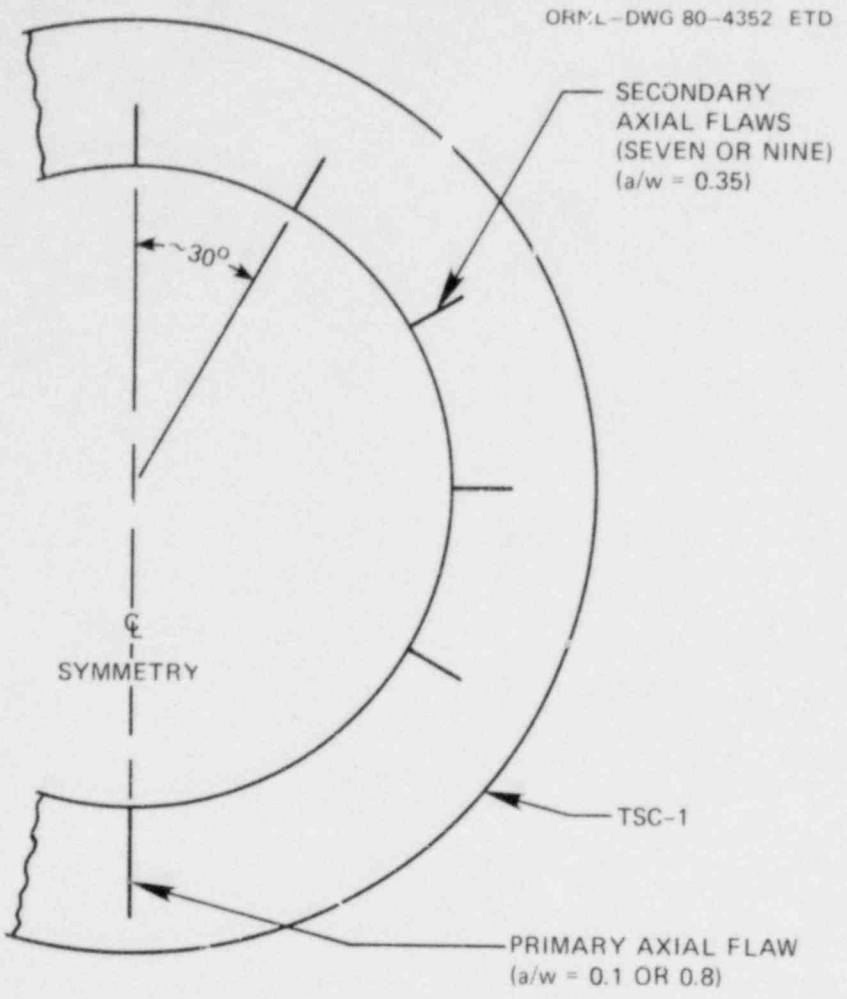

Fig. 4.3. Model used for two-dimensional analysis of secondary cracking effects during TSE-5.

Introduction of the secondary axial cracks tends to relieve the tensile stress in the inner portion of the wall and thus would tend to reduce the primary-crack COD. However, the existence of the secondary cracks also reduces the stiffness of the wall, and this reduction tends to increase the primary-crack COD.

Results of the analysis are shown in Table 4.3. For a primary-crack depth (a/w) of 0.1, the introduction of seven secondary cracks decreases the COD by only 3%. For a crack depth of 0.8, the introduction of seven secondary cracks increases the COD by 10%, and the introduction of nine secondary cracks reduces the COD by 5%. Thus, even if the secondary

Table 4.3. Calculated CODs for the TSE-5 primary crack with and without the existence of secondary cracking and with a/w (secondary) = 0.35 and t = 7 min

Total number of cracks	Primary-crack depth (a/w)	COD for primary crack (mm)
1	0.1	0.085
8	0.1	0.083
1	0.8	0.95
8	0.8	1.05
10	0.8	0.66

cracking occurred during the propagation period for the primary crack, the effect of the former on the latter would be very small.

4.3 Calculations Pertaining to TSE-5A

Test conditions desired for TSE-5A are essentially the same as those specified for TSE-5 and are partially illustrated in the critical-crack-depth set of curves shown in Fig. 4.4. These curves show that incipient warm prestressing (IWPS) occurs at a fractional crack depth (a/w) $\cong$ 0.45 and that the corresponding maximum K ratio $[(K_I/K_{Ic})_{max}] \cong 2.5$. For TSE-5 the actual toughness was less than specified, and the severity of the thermal shock was somewhat greater than expected. These combined conditions decreased the time to initiation and thus moved the initiation curve ($K_I = K_{Ic}$) to the left of what was expected. The difference in toughness does not affect the WPS curve, but the greater severity of the thermal shock causes K_I to peak earlier and thus moves the WPS curve to the left. For TSE-5 the former effect was much greater than the latter. Thus, IWPS occurred deeper in the wall (a/w $\cong$ 0.8) than desired, and the corresponding maximum K ratio was only 1.2. The critical-crack-depth curves illustrating this situation are shown in Fig. 4.5.

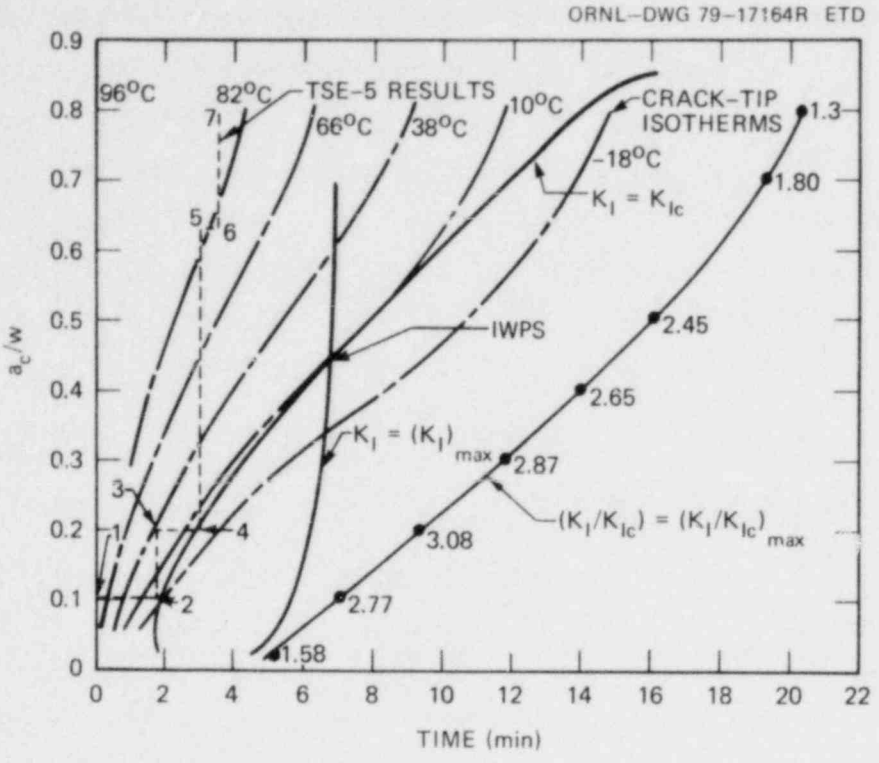

Fig. 4.4. Critical-crack-depth curves for TSE-5 (posttest) using design toughness curve.

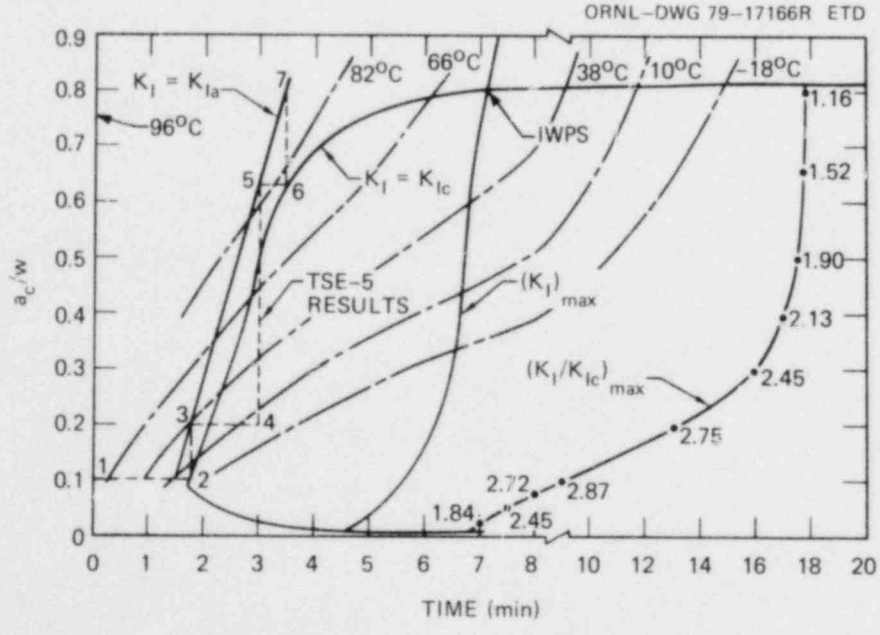

Fig. 4.5. TSE-5 critical-crack-depth curves using K_{Ic} curve based on first and third initiation events.

Parametric studies were conducted to determine how much variation in the K_{Ic} vs temperature curve, relative to that specified for TSE-5, could be tolerated and still provide appropriate conditions for demonstrating WPS and arrest in a rising K_I field. For these studies, the thermal shock achieved during TSE-5 was assumed. In another study, the severity of the thermal shock was increased so that, in combination with a higher-toughness material than that used for TSE-5, appropriate test conditions for TSE-5A might be achieved. These studies are discussed in the following sections.

4.3.1 Variations-in-toughness curves

The toughness curves used in these studies were believed at one time to be representative of A508 class 2 steel tempered in the range of 650 to 700°C; they are shown in Fig. 4.6 (curves b and c) along with the curve specified for TSE-5 (curve a) and that deduced from TSE-5 (curve d).

Curve a represents an average curve for HSST plate 02 (A533 grade B)[9] and is described by the American Society of Mechanical Engineers (ASME) Code Section XI, Appendix A, K_{Ic} curve with $RT_{NDT} = -34°C$. Curve b was based on a post-TSE-5 review of A508 class 2 data collected in connection with the HSST Program prior to TSE-5, and curve c is this same curve shifted to the right 56 K.

Results of the analysis using toughness curves b and c are shown in Figs. 4.7 and 4.8, respectively. As indicated by a comparison of Figs. 4.7 and 4.4, increasing the lower shelf without changing the transition temperature reduces the maximum K ratio corresponding to IWPS from ~2.5 to ~1.2 and that for an initial crack depth (a/w) = 0.1 from ~2.8 to ~1.2. These lower values of $(K_I/K_{Ic})_{max}$ are too small for an acceptable experiment design. However, the fractional crack depth associated with IWPS was not changed significantly by increasing the lower-shelf toughness.

Reducing the toughness relative to curve b in Fig. 4.6 by shifting curve b to the right by 56 K (curve c) increases the maximum K ratios relative to Fig. 4.7 but increases $(a/w)_{IWPS}$ to ~0.65, for which the maximum K ratio is only 1.1. The maximum K ratio for a shallow flaw (a/w ≅ 0.1) is satisfactory (~1.5) but not for $(a/w)_{IWPS}$. A possible

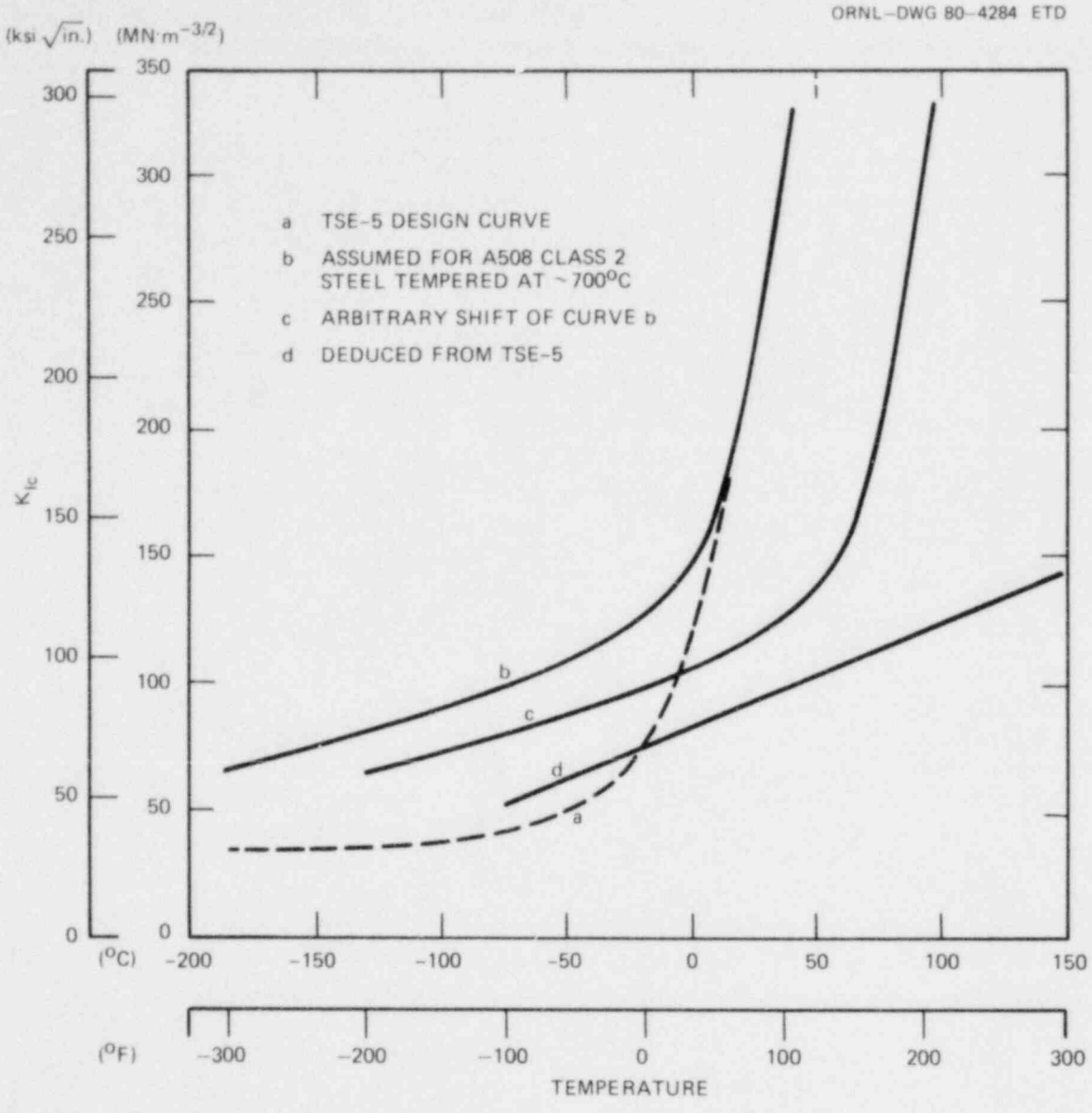

Fig. 4.6. K_{Ic} curves used in thermal shock studies.

solution to the dilemma is to reduce $(a/w)_{IWPS}$ by moving the $K_I = (K_I)_{max}$ curve to the left. In principle, this can be done by increasing the severity of the thermal shock; this approach is discussed in Sect. 4.3.2.

4.3.2 Variations in severity of thermal shock

Within the limits imposed by the rubber cement coating on the inner surface of the cylindrical test specimen, the severity of the thermal

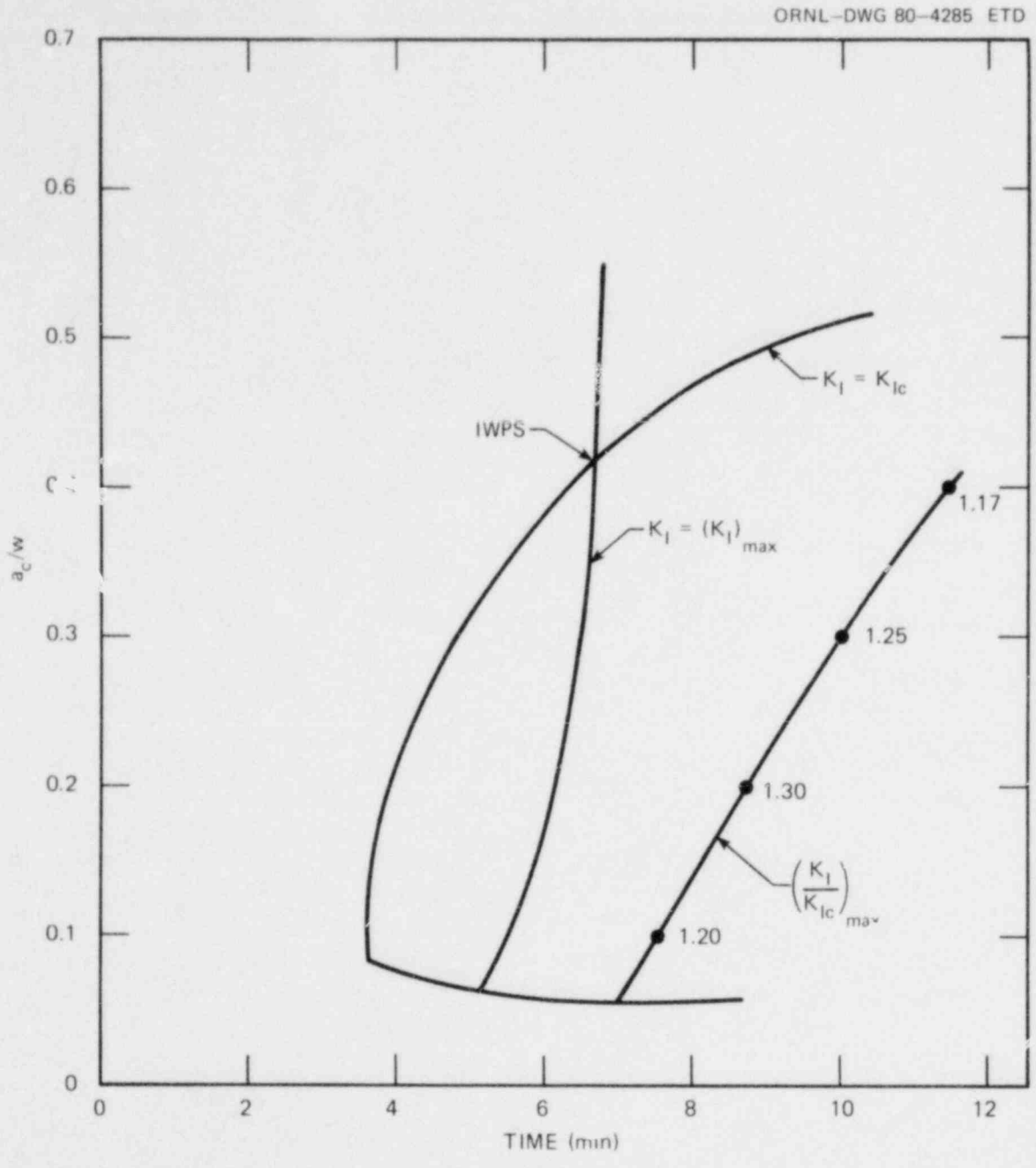

Fig. 4.7. Fractional critical crack depth (a_c/w) vs time using toughness curve b.

shock can be increased by an initial positive temperature grad through the wall. The inner-surface temperature would be limited to that dictated by the inner-surface coating, and the outer-surface temperature would be limited by thermal properties of the cylinder, heat removal capability at

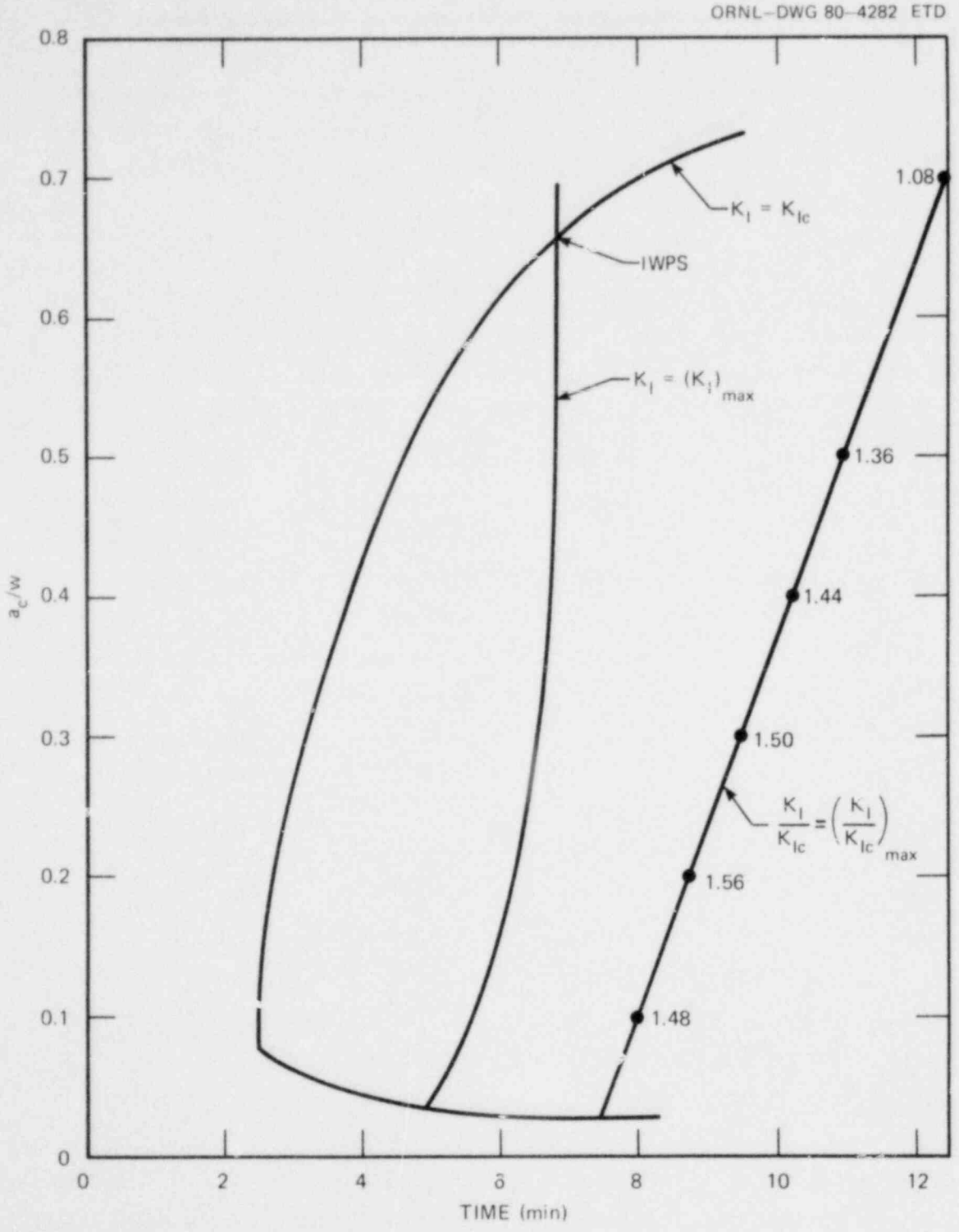

Fig. 4.8. Fractional critical crack depth (a_c/w) vs time using toughness curve c.

the inner surface during the heating cycle, and heat flux at the outer surface.

Calculations were made for a maximum inner-surface temperature of 93°C and a constant heat flux of 31 kW/m^2 (118 kW for the TSC-1 cylinder), with the inner surface insulated during the heating cycle. The heating cycle was terminated and the quench commenced when the inner-surface temperature reached 93°C. Typical temperature distributions during the quench in liquid nitrogen, using the inner-surface heat transfer coefficient specified for TSE-5, are shown in Fig. 4.9. Included in Fig. 4.9 are the temperature distributions at the beginning of the quench (t = 0) and at t = 5 min. For comparison purposes, distributions at t = 5 min for no added heat at the outer surface after t = 0 (same distribution at t = 0) and for a uniform temperature at t = 0 with no added heat after t = 0 are also included. At t = 0, the outer-surface temperature is 57 K higher than the inner-surface temperature. The outer-surface temperature reaches a maximum value of 160°C at t ≅ 3.5 min, and at t = 5 min it has dropped slightly to 159°C. Without the heat flux applied to the outer surface after t = 0, the outer-surface temperature at 5 min is 109°C; and with an initially uniform temperature of 93°C at t = 0, the outer-surface temperature at t = 5 min is 83°C. For the three cases, the initial temperature at the inner surface is 93°C, and at t = 5 min it is −76, −81, and −97°C. Thus, the differences between the temperature curves, particularly in the inner half of the wall, are not large. However, a final assessment must be based on the results of the fracture mechanics analyses.

Fracture mechanics analyses were performed for the case of continuous heat flux at the outer surface and for the case of uniform initial temperature; for both cases, toughness curve b in Fig. 4.6 and the TSE-5–design heat transfer coefficient were used. Results of the analyses are shown in Fig. 4.10, in which the critical-crack-depth curves for the two cases are compared. With uniform initial temperature at t = 0 and no heat added thereafter, $(a/w)_{IWPS}$ = 0.35, which is reasonable; but the maximum K ratios for the initial flaw (a/w ≅ 0.1) and for $(a/w)_{IWPS}$ are much too small. Applying heat to the outer surface improves the situation. For this case, $(a/w)_{IWPS}$ = 0.38, which is acceptable; the maximum K ratio for $(a/w)_{IWPS}$ is increased from 1.10 to 1.35, which is marginally acceptable.

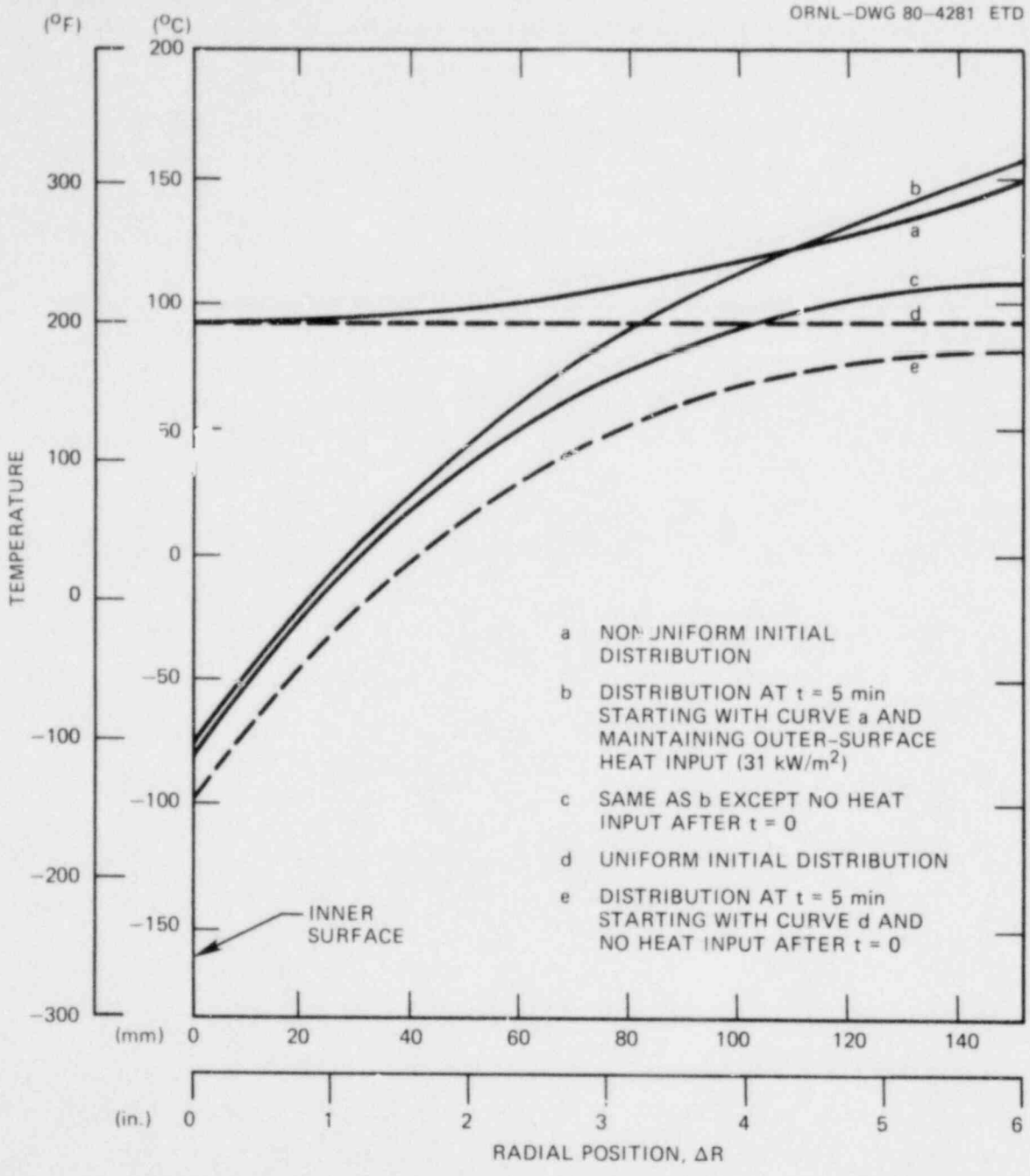

Fig. 4.9. Temperature distributions in test cylinder wall for different initial and transient conditions (TSE-5-design liquid nitrogen quench).

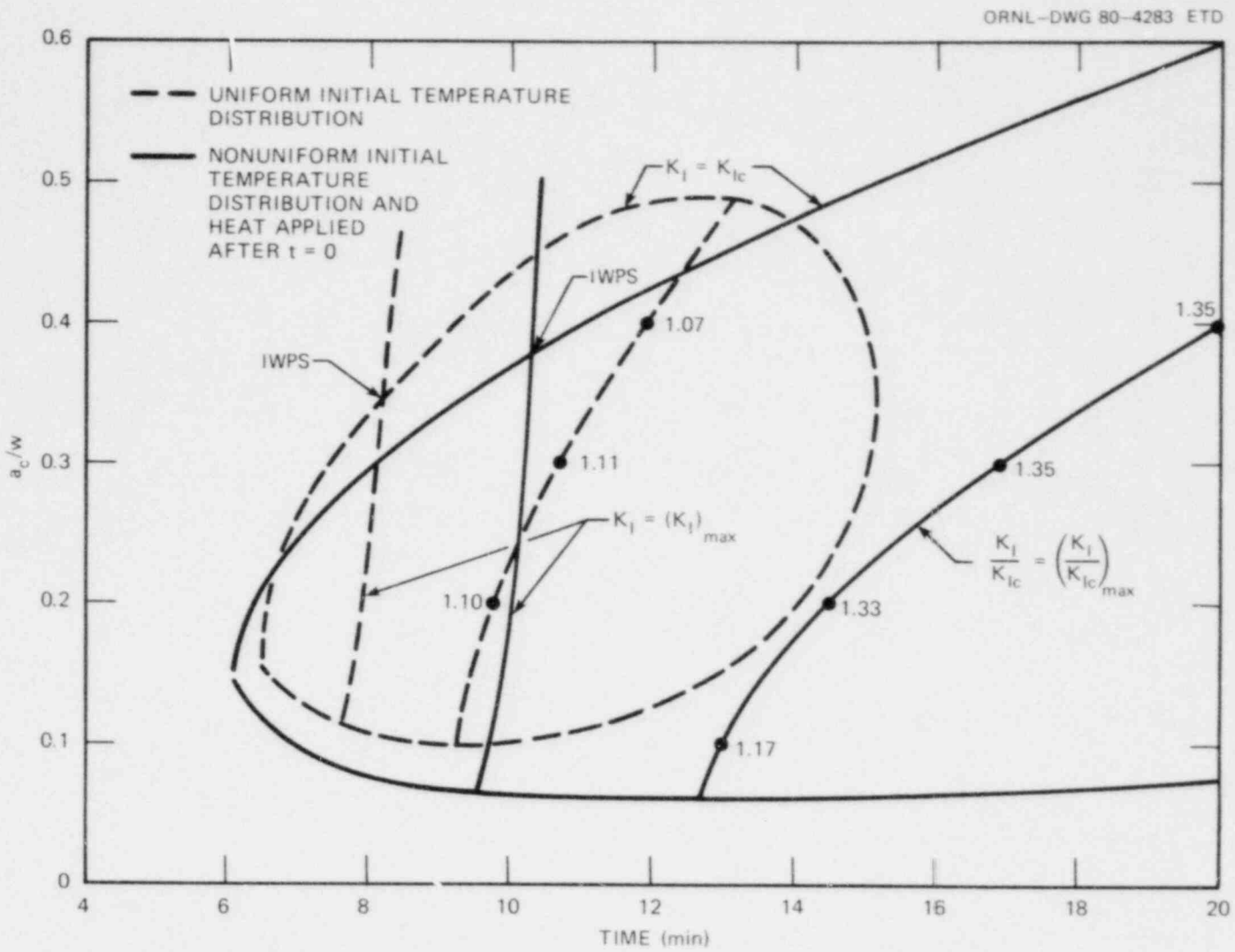

Fig. 4.10. Critical-crack-depth curves for uniform and nonuniform initial temperature distributions.

The maximum K ratio for a/w = 0.1 is increased also (1.00 to 1.17), but the increase is not sufficient to make this case acceptable.

As mentioned previously, the thermal shock during TSE-5 was more severe than assumed for the design of the experiment. Increased severity results in a substantial increase in the maximum K ratios; and if this increase were applied to the results in Fig. 4.10, an acceptable experiment, using the added-heat concept, might be achieved. For instance, the increase in maximum K ratio for a/w = 0.1 is ~20%, and for $(a/w)_{IWPS}$ it is ~10%. Applying these increases to the appropriate values in Fig. 4.10 results in maximum K ratios of 1.40 and 1.49 for a/w = 0.1 and $(a/w)_{IWPS}$, respectively. These are marginally acceptable values.

In another calculation the severity of the thermal shock was increased by increasing the heat transfer coefficient at the inner surface of the test cylinder above that achieved during TSE-5 and by increasing the initial temperature of the cylinder from 93 to 120°C. The initial temperature distribution was uniform, and there was no heat added after quenching commenced.

The heat transfer coefficient used was that obtained experimentally[10] prior to TSE-5 with a near-optimum coating of rubber cement. The specific curve of coefficient vs metal surface temperature is shown in Fig. 4.11 as curve a. Curve b in this figure is the one that was used for the design of TSE-5. The actual curve obtained during TSE-5 falls between curves a and b.

Results obtained from the calculations with the greater heat transfer coefficient are shown in Fig. 4.12. As indicated, $(a/w)_{IWPS} = 0.38$, $[(K_I/K_{Ic})_{max}]_{IWPS} = 1.34$, and $[(K_I/K_{Ic})_{max}]_{a/w = 0.1} = 1.48$. The latter value is satisfactory for initiation of the initial flaw, but the maximum K ratio corresponding to IWPS is somewhat less than desired, since the actual crack depth for which WPS would be demonstrated (the final arrested crack depth) might be ~0.45, which has a maximum K ratio of ~1.25. This is less than desired (from a design point of view) for a conclusive demonstration of WPS.

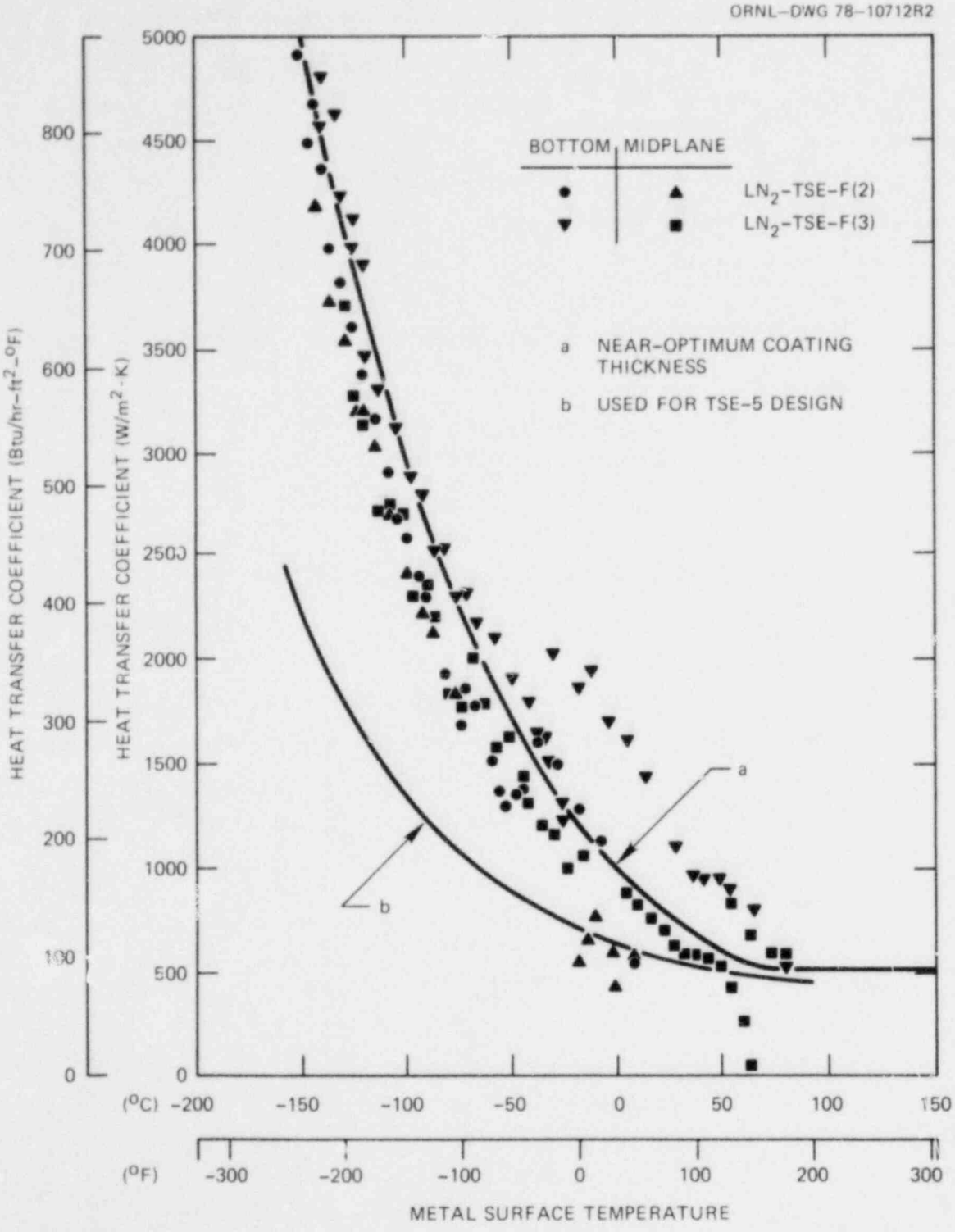

Fig. 4.11. Heat transfer coefficients obtained from LN_2 quench of TSV-F (530-mm-OD by 150-mm-wall thermal-hydraulic test cylinder). Surface coated with NF-34 adhesive. Experiments LN_2-TSE-F (2 and 3).

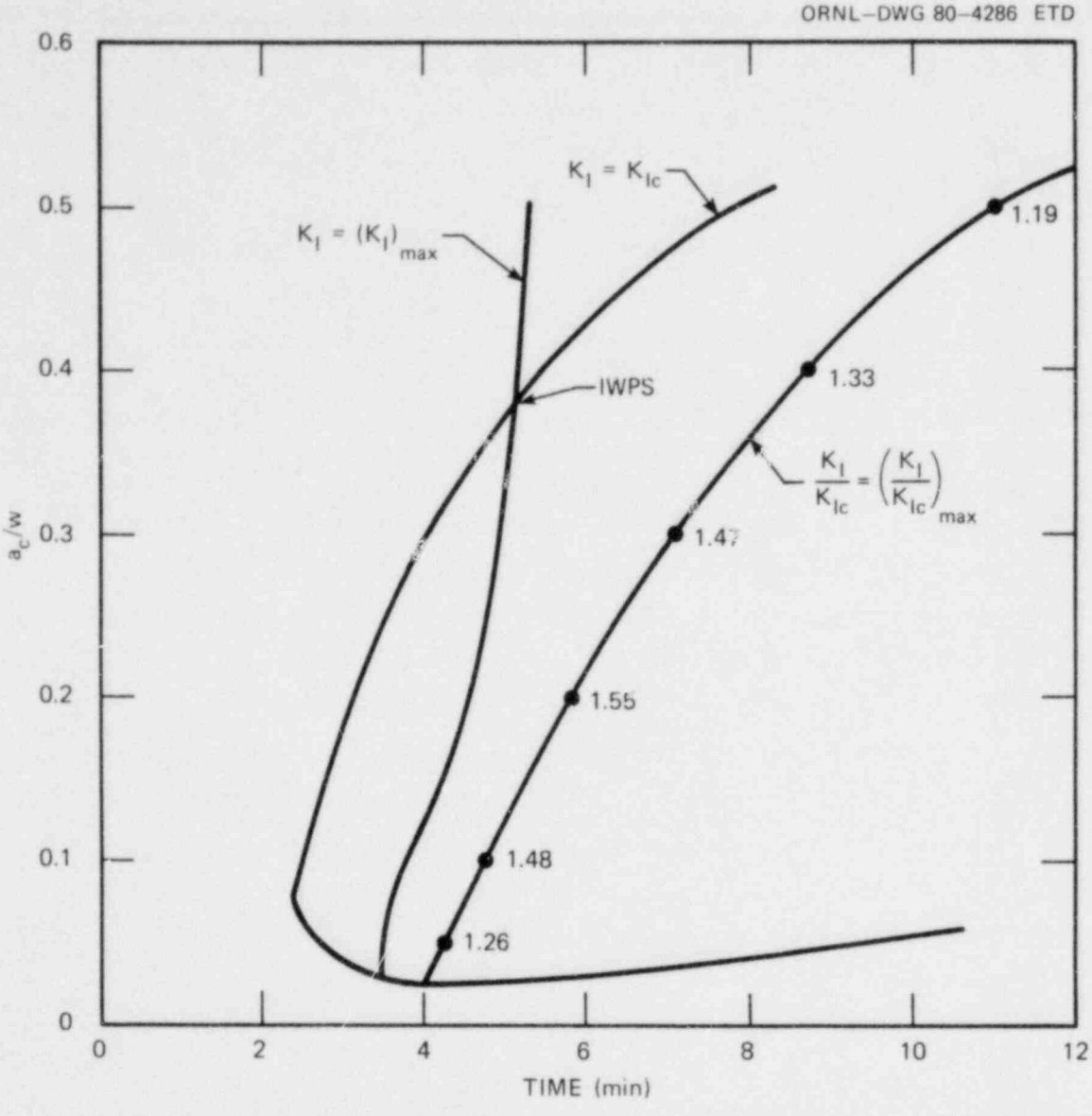

Fig. 4.12. Fractional critical crack depth (a_c/w) vs time using heat transfer coefficient vs temperature curve corresponding to near-optimum inner-surface coating thickness (liquid nitrogen quench, T_i = 129°C).

4.4 Thermal Shock Material Characterization

W. J. Stelzman D. A. Canonico

Characterization of the fracture toughness and tensile properties of the thermal shock cylinder TSC-1 and a prolongation (TSP-1) of this cylinder is continuing. Both the cylinder and the prolongation have

received identical heat treatments, including tempers of 613°C for 4 h. The fracture toughness properties are also being investigated at higher tempering temperatures using material from a second prolongation (TSP-2) that has received normalizing, austenitizing, and quenching treatments identical to those of TSC-1 and TSP-1. Three tempering temperatures (649, 677, and 707°C) are being evaluated using the TSP-2 material.

The cylinders and prolongations used in the thermal shock experiment and characterization were machined from forgings that had a 216-mm wall thickness when quenched. The as-quenched forgings had an inside diameter of 622 mm and an outside diameter of 1054 mm.

The tensile properties of the tempered samples from TSC-1 and TSP-1 were determined in the C orientation and at the quarter-thickness depth (from the inside surface of the thermal shock cylinder). Test temperatures ranged from −46 to 288°C. The effect of depth on the tensile properties in TSC-1 and TSP-1 was also investigated at three temperatures (−18, 38, and 93°C). Results from TSC-1 and TSP-1 are listed in Tables 4.4 and 4.5, respectively. The ultimate tensile strength at room temperature and at the one-fourth T depth location in TSC-1 is about 835 MPa.

It is important to recognize that the forgings used in this experiment (TSC-1) satisfy the chemical composition requirements for SA508 class 2 but do not meet the tensile requirements of that specification. The ultimate tensile strength range permitted in SA508 class 2 is 550 to 725 MPa. Therefore, although the TSC-1 cylinder satisfies the chemical composition in the SA508 class 2 specification, it is not SA508 class 2 because its ultimate tensile strength (835 MPa) is higher than the maximum permitted.

The tensile strength values are plotted in Fig. 4.13. The tensile properties of the test cylinder and prolongation are quite similar. As shown in Fig. 4.13, the difference between TSC-1 and TSP-1 is only about 15 to 25 MPa. Depth had little effect on the strength and ductility of TSC-1 and TSP-1. Very little difference exists between the tensile properties at the 0.04 (or 0.96) depth location and those at any other depth locations. The low variation of tensile properties through the cylinder wall was not unexpected, since 32 mm was machined from the as-quenched surfaces of all the forgings prior to tempering. Thus, the 0.04 depth

Table 4.4. Tensile properties[a] at several depth locations[b] through the 152-mm-thick wall of thermal shock vessel TSC-1[c]

Depth location[d]	Temperature (°C)	Stress (MPa)		Ductility (%)		
		Yield[e]	Ultimate	Total elongation[f]		Reduction of area
				L/D = 7	L/D = 4	
0.04	−18	716	851	13.4	18.3	56.0
0.04	38	696	826	14.6	20.1	59.8
0.04	93	672	801	11.7	16.0	56.2
0.21	−46	731	869	13.6	19.4	55.8
0.21	−18	707	843	14.3	19.6	54.8
0.21	10	695	825	12.8	17.0	53.1
0.21	38	680	807	12.7	17.4	56.3
0.21	93	656	780	12.4	16.8	55.6
0.21	177	630	766	12.2	17.0	57.2
0.21	288	638	779	12.2	16.9	56.8
0.50	−18	702	839	13.4	19.8	53.4
0.50	38	677	802	12.8	17.6	57.0
0.50	93	655	776	11.5	15.9	55.4
0.75	−18	706	836	13.7	18.5	54.4
0.75	38	666	794	12.8	17.4	57.8
0.75	93	652	775	12.0	16.5	55.2
0.96	−18	715	849	14.1	19.2	56.0
0.96	38	685	808	12.2	16.8	55.8
0.96	93	662	783	11.6	15.8	54.8

[a] Average of two specimens, both C-oriented.

[b] The wall of the cylinder was 216 mm thick when quenched. Approximately 32 mm was removed from the inner and outer surfaces, leaving a 152-mm wall thickness.

mpered at 613°C for 4 h, air-cooled.

[d] Fraction of the 152-mm thermal shock vessel wall thickness; inner surface = 0 t.

[e] 0.2% offset; strain rate = 0.016/min.

[f] Gage length/gage diam ratio (L/D) = 4 is a calculated value.

Table 4.5. Tensile properties[a] at several depth locations[b] through the 152-mm-thick wall of thermal shock vessel TSC-1 prolongation TSP-1[c]

Depth location[d]	Temperature (°C)	Stress (MPa)		Ductility (%)		
		Yield[e]	Ultimate	Total elongation[f] L/D = 7	Total elongation[f] L/D = 4	Reduction of area
0.04	−18	734	881	13.9	19.2	55.1
0.04	38	711	842	12.7	17.6	55.9
0.04	93	678	816	12.5	17.2	55.0
0.21	−46	751	892	13.7	18.5	49.6
0.21	−18	727	869	13.7	18.8	55.4
0.21	10	710	850	13.0	17.4	54.8
0.21	38	696	828	13.0	18.1	54.9
0.21	93	666	799	11.7	16.2	55.2
0.21	177	647	789	12.5	17.3	54.4
0.21	288	660	803	12.5	17.6	54.2
0.50	−18	730	869	15.3	21.0	56.3
0.50	38	695	828	12.8	17.9	57.1
0.50	93	664	799	13.9	19.3	58.4
0.75	−18	719	864	14.6	20.2	59.2
0.75	38	687	820	13.4	18.7	57.7
0.75	93	662	793	13.2	18.6	59.9
0.96	−18	734	875	14.2	19.5	57.1
0.96	38	704	835	13.2	18.3	57.6
0.96	93	683	816	11.8	16.2	53.5

[a] Average of two specimens, both C-oriented.

[b] The wall of the cylinder was 216 mm thick when quenched. Approximately 32 mm was removed from the inner and outer surfaces, leaving a 152-mm wall thickness.

[c] Tempered at 613°C for 4 h, air-cooled.

[d] Fraction of the 152-mm prolongation wall thickness; inner surface = 0 t.

[e] 0.2% offset; strain rate = 0.016/min.

[f] Gage length/gage diam ratio (L/D) = 4 is a calculated value.

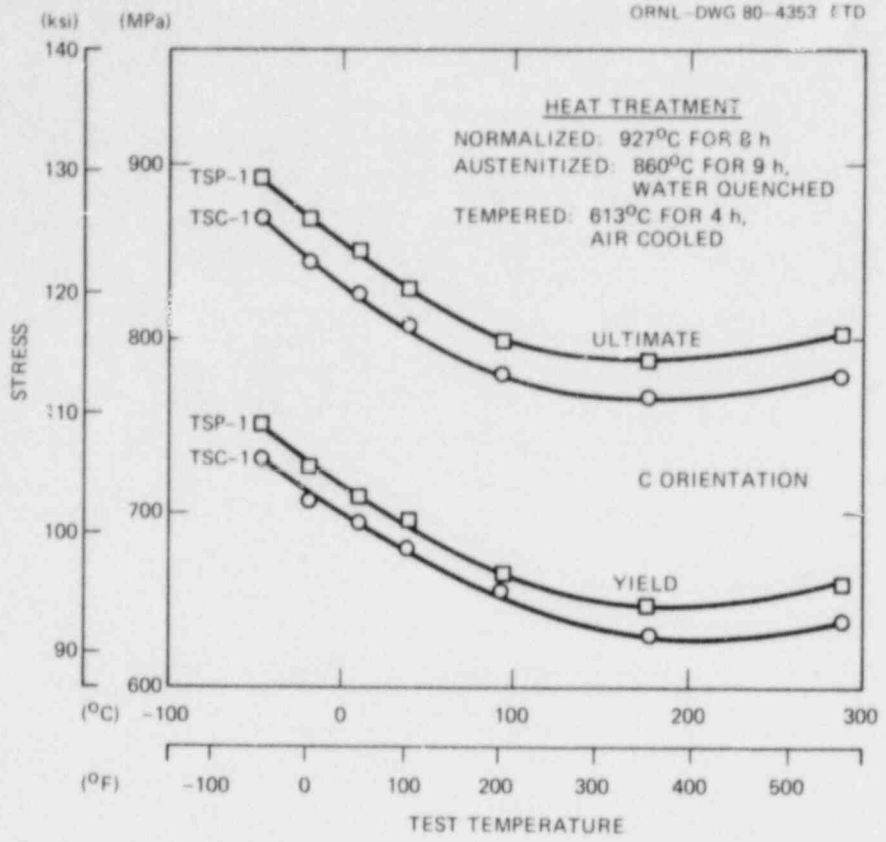

Fig. 4.13. Tensile properties at the quarter-thickness depth in the 152-mm-thick wall of thermal shock cylinder TSC-1 and prolongation TSP-1.

location in the 152-mm-thick wall of the thermal shock cylinder is the 0.18 depth location when referenced to the forging blank that was quenched from the austenitizing temperature.

The fracture toughness testing is being conducted with CT-oriented 1T and 2T compact specimens (1T CS and 2T CS) of material from TSP-1 and TSP-2 tempered at 613, 649, 677, or 707°C for 4 h. The major portion of the posttest TSC-1 fracture toughness examination (613°C temper) is being made with the TSP-1 material because of the shortage of suitable TSC-1 material. The results are listed in Table 4.6. Emphasis is being placed on testing multiple specimens at a single test temperature to determine the lower bound of fracture toughness and the degree of scatter. Recent experience indicates that testing too few specimens at a single temperature can result in an erroneous fracture toughness value. This observation is supported by nine 1T CS from the 707°C tempered material tested

Table 4.6. Static fracture toughness (K_{Icd}) from 1T and 2T compact specimens[a] of quenched prolongations TSP-1 and TSP-2 after tempering at 613, 650, and 707°C

Temper temperature[b] (°C)	Test temperature (°C)	Static fracture toughness, K_{Icd} ($MN \cdot m^{-3/2}$)
613	82	210
	82	131[c]
	82	134[c]
	82	256[c]
	135	272[c]
650	−18	85
	−18	118
	10	236
	10	126
	38	239
	38	105
	66	261
	93	246
707	−73	131
	−4	317
	−4	337
	−4	226
	−4	140
	−4	219
	−4	180
	−4	243
	−4	274
	−4	248
	38	336
	66	373

[a] CT-oriented.

[b] Tempered for 4 h, air-cooled.

[c] 2T compact specimens; remainder 1T.

at −4°C. Most of the specimens indicate a high fracture toughness; however, continued testing resulted in a low value of 140 $MN \cdot m^{-3/2}$. As can be seen in Table 4.6, values as high as 337 $MN \cdot m^{-3/2}$ were obtained at −4°C. A similar test procedure will be used when testing the 613, 677, and 707°C tempered materials at two or three test temperatures. Partial results from 1T CS and 2T CS from the 613°C tempered material tested at 82°C and results from 1T CS from the 649°C tempered material are also listed in Table 4.6.

The tests conducted on material tempered at 613°C are part of the characterization study of the TSC-1 material. As reported earlier, TSC-1 underwent an initiation event at near 82°C late into the experiment. Six 1T CSs were tested (four at Battelle Memorial Institute[11] and two at ORNL). All failed at toughness levels near 220 $MN \cdot m^{-3/2}$, a value considerably higher than that observed in the experiment. Not until the seventh specimen was tested was a value observed near that in the experiment. This need to test a number of specimens, in some instances considerably more than the three recommended in ASTM E399, is under investigation.

Further fracture toughness testing is in progress on the 613, 677, and 707°C tempered material. Charpy V impact and drop-weight properties are also being examined for the 613°C tempered material (TSC-1 and TSP-1).

References

1. R. D. Cheverton, *Heavy-Section Steel Technology Program Quart. Prog. Rep. April–June 1979*, ORNL/NUREG/TM-347, pp. 59–63.

2. R. D. Cheverton, *Heavy-Section Steel Technology Program Quart. Prog. Rep. July–September 1979*, ORNL/NUREG/TM-370.

3. J. D. Landes and D. H. Shaffer, *Statistical Characterization of Fracture in the Transition Region*, Scientific Paper 79-ID3-JINTF-P4, Westinghouse Research and Development Center (June 8, 1979).

4. W. J. Stelzman and D. A. Canonico, "Thermal Shock Temper Study," *Heavy-Section Steel Technology Program Quart. Prog. Rep. October–December 1978*, ORNL/NUREG/TM-298, pp. 57–61.

5. W. J. Stelzman and D. A. Canonico, "Thermal Shock Temper Study," *Heavy-Section Steel Technology Program Quart. Prog. Rep. January–March 1979*, ORNL/NUREG/TM-324, pp. 104–110.

6. W. J. Stelzman and D. A. Canonico, "Thermal Shock Temper Study," *Heavy-Section Steel Technology Program Quart. Prog. Rep. April–June 1979*, ORNL/NUREG/TM-347, pp. 68–72.

7. W. J. Stelzman and D. A. Canonico, "Thermal Shock Temper Study," *Heavy-Section Steel Technology Program Quart. Prog. Rep. July–September 1979*, ORNL/NUREG/TM-370.

8. R. D. Cheverton and S. E. Bolt, *Pressure Vessel Fracture Studies Pertaining to a PWR LOCA-ECC Thermal Shock: Experiments TSE-3 and TSE-4 and Update of TSE-1 and TSE-2 Analysis*, ORNL/NUREG-22 (December 1977), pp. 79–81.

9. W. O. Shabbits et al., *Heavy Section Fracture Toughness Properties of A533 Grade B Class 1 Steel Plate and Submerged-Arc Weldment*, Heavy-Section Steel Technology Program Technical Report No. 6, WCAP-7414 (December 1969).

10. R. D. Cheverton, *Heavy-Section Steel Technology Program Quart. Prog. Rep. April–June 1978*, ORNL/NUREG/TM-239, pp. 50–58.

11. A. R. Rosenfield, Battelle Memorial Institute, private communication to R. D. Cheverton, ORNL, Dec. 19, 1979.

5. PRESSURE VESSEL INVESTIGATIONS*

Work during this report period was concerned with preparations for the next intermediate vessel test, V-8A, and examining the possibilities of repairing and testing vessel V-7 for Pacific Northwest Laboratories (PNL) as a part of their acoustic emission (AE) flaw-growth-characterization program. No work was undertaken to develop the pressurized thermal shock and thermal fatigue test facility, in accordance with the current financial plan. This work is expected to continue later in the fiscal year.

5.1 Intermediate Vessel Test V-8A

P. P. Holz

Vessel 8 is scheduled for reuse after repair and modification to include a seam weld especially designed to have low toughness and tensile properties similar to irradiated low-toughness weldments in several existing reactor pressure vessels. A V-8A test will be both a demonstration of the behavior of a crack in such material and a study of the mechanism of upper-shelf fracture in a large structure.

A request for bids was prepared and issued to (1) repair vessel 8 and insert a new, special, longitudinal low-toughness seam weldment; (2) provide additional low-toughness weldments in a vessel prolongation and test pieces; and (3) perform metallurgical specimen preparations, tests, and analyses to give full characterization of these weldments. Bids are to be evaluated in January 1980.

The job involves research to develop a welding process and materials that will produce a weldment with special metallurgical and mechanical properties. The proposed contract consists of three phases. Phase I includes trial welds and a feasibility demonstration complete with nondestructive examination and material property test results to prove that toughness requirements are met. Other work requirements call for shop

---

*Conversions from SI to English units for all SI quantities are listed on a foldout page at the end of this report.

drawings and procedures for the seam, repair, and material characterization welds. Phase II includes making these welds along with an additional weld for flawing practice at ORNL. Phase III comprises a complete weld metal characterization and preparation of a final documentary report.

5.2 Proposed AE Tests with Vessel V-7 (V-7AE)

R. H. Bryan

The 11 tests of intermediate test vessels were monitored with AE systems by 5 different organizations.[1-7] The tests were opportunities for studying the capabilities of the AE systems in detecting known flaws in thick-section vessel tests. One to three systems were used in a particular test. The systems were generally capable of mapping source locations and recording data for each AE event concerning its magnitude.

Researchers at PNL, who participated in the last two tests,[6-7] are developing for the NRC AE techniques to detect and analyze flaw growth.[8] They are considering using a repaired intermediate test vessel and an HSST Facility for a series of tests in which AE will be observed during cyclic loading. PNL requested that ORNL determine the extent to which their proposed requirements could be met.

The evaluation of test capabilities was based on the assumption that only minor modifications to the facility could be considered because of budgetary limitations. Furthermore, PNL's interest in tests that could be initiated in FY 1980 precluded use of planned pressurized thermal shock and thermal fatigue test facilities.[9]

Preparation of the test vessel for the AE program would involve repairing vessel V-7, preparing fatigue-sharpened flaws, implanting a slag inclusion, and applying test instrumentation. Other attachments could be made, such as stainless steel weld-overlay cladding and devices that would be sources of extraneous noise; but the utility of these additions in an initial test program has not been evaluated.

The ultimate range of test conditions and loading modes in which PNL is interested is the range experienced in a nuclear power plant. Cyclic pressure loading and localized cyclic thermal loading are both of interest. The latter cannot be accomplished in the vessel test facilities

until modifications are made for pressurized thermal shock and thermal fatigue tests. Cyclic pressure loadings are feasible only at low frequencies, and high test temperatures involve complications that may not be justifiable in a first test. These two limitations are discussed further.

There are two ways of cyclically pressure-loading a flaw in the test vessel: by varying internal pressure or by cyclically pressurizing the flaw notch while holding internal pressure constant. Cyclic notch pressurization is preferable for several reasons. The room-temperature phase of the V-7AE test program, if run to a full course of ~114,000 cycles, would require 239 uninterrupted 8-h working days with cyclic internal pressurization but only about 8 d with notch pressurization. Cyclic pressurization of the entire vessel would entail periodic repair and refurbishing of the pressurization system and the vessel closure, which would substantiallly prolong the test program. Cyclic notch pressurization would allow more flexibility in the choice of loading parameters; the R ratios and ΔKs could be chosen almost independently both initially and during the test. Furthermore, multiple flaws could be loaded individually. The disadvantages of notch pressurizations are that measuring COD at the notch opening may be impossible and that crack growth which increases the volume of the notch significantly would require more complex pump-and-dump systems.

The cyclic vessel pressurization frequency is limited by the capacity of the intensifier on the positive part of the cycle and by sonic flow on depressurization. The rates that can be achieved with our present equipment were estimated on the assumption that 94% of the internal volume of the vessel is occupied by ballast. Pressurization and venting times are derived from actual test data for venting through a single line.[7] Typical results are as follows.

Pressure range (MPa)	Fill time (s)	Dump time (s)
7.6 to 72	38	10
5.8 to 72	9	2

These contain no allowance for the opening and closing transients or for

actuation of mechanisms. In contrast to these rates for vessel pressurization, practical cycle times less than 1.8 s have been attained in notch pressurization.

Intermediate test vessel design limits the number of internal pressure-loading cycles that can be applied. The vesssel closure is designed for 100 cycles to 110 or 138 MPa, depending on the temperature. This number is sufficiently low that, in accordance with the provisions of the ASME Boiler and Pressure Vessel Code, a fatigue analysis was not required and thus was not made. The closure studs (or the head) may be the critical component. They can probably take much more than 100 cycles but cannot be expected to approach tens of thousands. Inspection and replacement during an extensive test program would be necessary, and the test facility would have to be designed to prevent costly damage to the instrumented vessel assembly if a closure failure occurred.

High temperatures can be imposed upon an intermediate test vessel. The test facility was designed to permit tests nominally up to 180°C, although no tests above 93°C have been performed. Vessel temperatures up to 290°C can probably be attained with electrical heaters. However, the pressurization system is not capable of handling water or other fluids above their saturation temperatures at atmospheric pressure. With minor modifications to the present test facility, heating a test vessel to 290°C and maintaining it at approximately constant pressure may be possible. Cyclic notch pressurization under this condition can also probably be performed.

References

1. R. W. Derby et al., *Test of 6-In.-Thick Pressure Vessels. Series 1: Intermediate Test Vessels V-1 and V-2*, ORNL-4895 (February 1974).

2. R. H. Bryan et al., *Test of 6-In.-Thick Pressure Vessels. Series 2: Intermediate Test Vessels V-3, V-4, and V-6*, ORNL-5059 (November 1975).

3. J. G. Merkle et al., *Test of 6-In.-Thick Pressure Vessels. Series 3: Intermediate Test Vessel V-7*, ORNL/NUREG-1 (August 1976).

4. J. G. Merkle et al., *Test of 6-In.-Thick Pressure Vessels. Series 4: Intermediate Test Vessels V-5 and V-9*, ORNL/NUREG-7 (August 1977).

5. R. H. Bryan et al., *Test of 6-In.-Thick Pressure Vessels. Series 3: Intermediate Test Vessel V-7A Under Sustained Loading*, ORNL/NUREG-9 (February 1978).

6. R. H. Bryan et al., *Test of 6-In.-Thick Pressure Vessels. Series 3: Intermediate Test Vessel V-7B*, ORNL/NUREG-38 (October 1978).

7. R. H. Bryan et al., *Test of 6-In.-Thick Pressure Vessels. Series 3: Intermediate Test Vessel V-8*, ORNL/NUREG-58 (December 1979).

8. P. H. Hutton, R. J. Kurtz, and E. B. Schwenk, "Acoustic Emission-Flaw Relationship for In-Service Monitoring of Nuclear Pressure Vessels," Seventh Water Reactor Safety Research Information Meeting, sponsored by the Nuclear Regulatory Commission, November 5–8, 1979, Gaithersburg, Md.

9. R. H. Bryan et al., "Pressurized Thermal Shock and Thermal Fatigue Tests," *Heavy-Section Steel Technology Program Quart. Prog. Rep. July–September 1979*, ORNL/NUREG/TM-370, p. 51.

CONVERSION FACTORS[a]

SI unit	English unit	Factor
mm	in.	0.0393701
cm	in.	0.393701
m	ft	3.28084
m/s	ft/s	3.28084
kN	lb_f	224.809
kPa	psi	0.145038
MPa	ksi	0.145038
$MN \cdot m^{-3/2}$ ($MPa \cdot \sqrt{m}$)	ksi $\sqrt{in.}$	0.910048
J	ft-lb	0.737562
K	°F or °R	1.8
kJ/m^2	$in.-lb/in.^2$	5.71015
$W \cdot m^{-2} \cdot K^{-1}$	$Btu/hr-ft^2-°F$	0.176110
$T(°F) = 1.8\ T(°C) + 32$		

[a]Multiply SI quantity by given factor to obtain English quantity.

NUREG/CR-1305
ORNL/NUREG/TM-380
Dist. Category RF

Internal Distribution

1. R. G. Berggren
2. S. E. Bolt
3-7. R. H. Bryan
8. J. W. Bryson
9. D. A. Canonico
10. R. D. Cheverton
11. J. M. Corum
12. W. B. Cottrell
13. W. L. Greenstreet
14. R. C. Gwaltney
15. P. P. Holz
16. S. K. Iskander
17. K. K. Klindt
18. J. G. Merkle
19 C. A. Mills
20. S. E. Moore
21. F. R. Mynatt
22. D. J. Naus
23. F. H. Neill
24. J. L. Rich
25. G. C. Robinson
26. G. M. Slaughter
27. J. E. Smith
28. W. J. Stelzman
29. H. E. Trammell
30-34. G. D. Whitman
35. Patent Office
36-37. Central Research Library
38. Document Reference Section
39-40. Laboratory Records Departmen
41. Laboratory Records (RC)

External Distribution

42. C. Z. Serpan, Reactor Safety Research, Nuclear Regulatory Commission, Washington, DC 20555
43. M. Vagins, Reactor Safety Research, Nuclear Regulatory Commission, Washington, DC 20555
44. Office of Assistant Manager, Energy Research and Development, DOE, ORO
45-46. Technical Information Center, DOE
47-456. Given distribution as shown in category RF (NTIS – 10)

☆U.S. GOVERNMENT PRINTING OFFICE: 1980-640-245/057